A Polarimetry Measurement for the Nab Experiment

by

Chelsea Hendrus

A dissertation submitted in partial fulfillment
of the requirements for the degree of
Doctor of Philosophy
(Physics)
in the University of Michigan
2023

Doctoral Committee:

Professor Tim Chupp, Chair
Professor Fred Adams
Professor Christine Aidala
Professor Angela Calabrese Barton
Professor Joshua Spitz

Chelsea Hendrus
hendrusc@umich.edu
ORCID iD: 0000-0002-4756-7317

DEDICATION

For the people who support me in the search for all my heart's desires

"If I ever go looking for my heart's desire again, I won't look any further than my own back yard. Because if it isn't there, I never really lost it to begin with... There's no place like home."

–The Wizard of Oz

ACKNOWLEDGMENTS

"I don't know half of you half as well as I should like, and I like less than half of you half as well as you deserve."

– J.R.R. Tolkien, The Fellowship of the Ring

Getting a PhD has been a long and challenging journey for me, and it is incredible to finally see at least some of these parts of it come together. No one completes a doctoral project alone, and I am blessed to have many people to thank for their help in getting me here. I'm sure they all know who they are, and I don't think most of them of them will need to read this thesis to figure it out. However, it feels wrong to leave this page empty, so without further ado:

My deepest and most sincere thanks go to my family, and my incredible partner, Ethan, (who has uprooted his entire life to follow me through a couple of the hardest parts of this journey). Their fiercely unwavering support is worth more than anything else in this world. Thank you all for your confidence in all this weird stuff that I have chosen to do. I would not be writing this thesis without their constant encouragement. They are my favorite source of joy and laughter.

Many thanks to my dearest friend Dr. Elizabeth Mae Scott. I am endlessly glad that we ended up working on Nab together, rather than either of us having to go it alone. Thank you for reminding me to take care of myself, teaching me how to live in Knoxville, suggesting some of the best ways to relax and make the best of this process, and being an amazing friend.

And finally, Thank you to my many advisors, Tim Chupp, Geoff Greene, Nadia Fomin, and all the other members of the Nab Experiment. You have all given me the space and patience to explore physics in my own way. For that, I am grateful, and from that, I have learned a lot.

Funding Acknowledgement: Funding for this work was provided by the NSF Program for Nuclear Physics and a DOE Science Graduate Student Research Award (SCGSR), and Rackham Graduate School.

TABLE OF CONTENTS

LIST OF FIGURES

FIGURE

LIST OF TABLES

TABLE

LIST OF APPENDICES

ABSTRACT

The Nab Experiment aims to use the Spallation Neutron Source at Oak Ridge National Lab to measure two parameters associated with the kinematics of the beta decay of free neutrons. The first is the electron-neutrino correlation coefficient, a, with a precision goal of $\frac{\Delta a}{a} = 10^{-3}$. This parameter is closely related to λ, the ratio between vector and axial vector coupling constants in the Standard Model, and can probe charge-parity violating asymmetries associated with the weak interaction. The experiment also aims to measure b, the Fierz interference term, to a precision of $\Delta b = 10^{-3}$. This term represents the way that tensor interactions, processes beyond the Standard Model, may affect neutron beta decay.

The methods used in this experiment require unpolarized neutrons, as the polarization can couple to the momenta of the daughter particles and present a systematic error. Because a spallation source is used, it is expected that there should be no beam polarization, however weak magnetic interactions with the neutron guide, choppers, and other components of the beamline may induce a small polarization. In order to meet the experiment's systematic error budget, the neutron beam for the Nab experiment must have a polarization less than $P_n = 2 \times 10^{-5}$. The work that follows describes the design and construction of an Adiabatic-Fast-Passage (AFP) Spin Flipper, procedures for polarizing gas in a glass cell using Spin-Exchange Optical Pumping (SEOP), and how these polarized cells can be used in conjunction with the Spin Flipper to measure and mitigate the neutron beam polarization.

CHAPTER 1

Introduction: Neutrons, the Standard Model, and Beta Decay

The idea of the neutron was first proposed by Ernest Rutherford, in 1920. At the time, it was an idea that was useful in describing several puzzling results associated with isotopes of different masses for the same elemental species and helped to explain how an atom might contain a small region of positive charge, as demonstrated by α and β particle scattering experiments. Initially, Rutherford and others thought the neutron might be a tightly bound electron-proton system[1, 2], but after the physical neutron was discovered by Chadwick, in 1932, it became clear that this type of composite particle was not possible in the current scheme of quantum mechanics. [2]

Chadwick's experiment was built off of observations from experiments performed by Irene and Frederic Joliot-Curie, who bombarded beryllium with α particles. It was noted that those samples released some sort of radiation, that could interact with light elements to produce recoil products. Chadwick studied the trajectories of these recoil products further, to determine that the radiation from the beryllium sample was most likely composed of particles with a negligible charge, and had approximately if not slightly more than the mass of a proton.[2]

Neutrons were quickly adopted as a tool commonly used in nuclear physics, materials science, and chemistry to study material properties and atomic phenomena, including nuclear decay, nuclear structure, and constructing new elements and isotopes. They are intimately linked to historical discoveries that helped piece together the Standard Model, weak interactions, and the discovery of the neutrino. They are also a source for powerful tests of symmetry breaking in the Standard

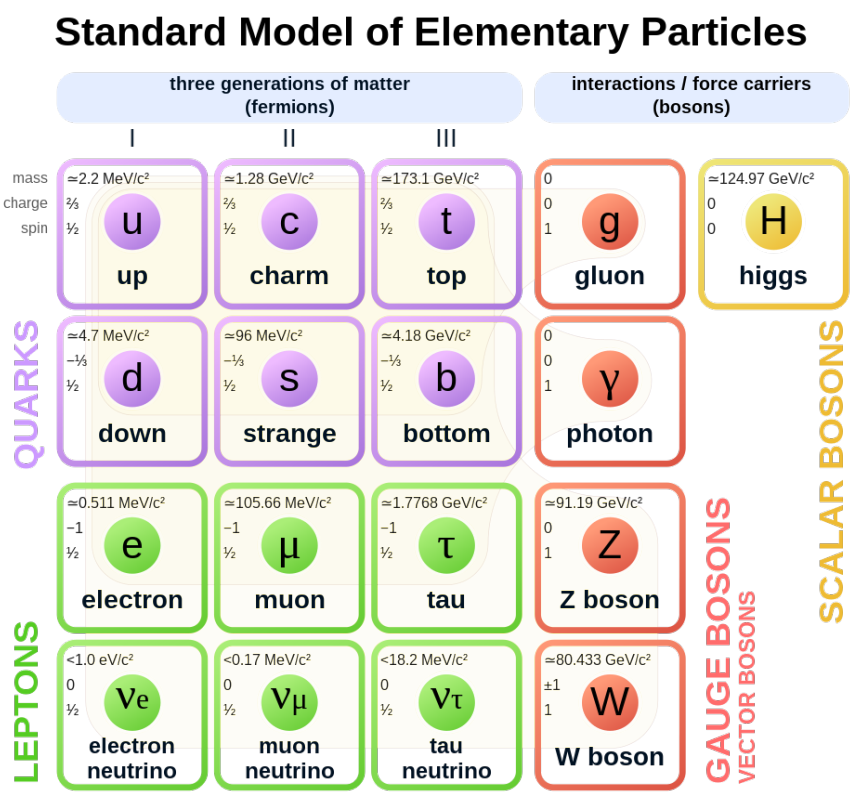

Figure 1.1: A chart depicting all the particles associated with the Standard Model of Particle Physics, and some of their properties (Image courtesy Wikimedia Commons)

Model and an interesting laboratory for examining the holes in the Standard Model where new physics might be found.

1.1 Weak Symmetry Breaking in the Standard Model

The Standard Model of Particle Physics has long been praised as a theory that unites many of the fundamental forces and the particles they mediate interactions between into one cohesive picture. The main constituents of the Standard Model are illustrated in Figure 6.1.

The fundamental forces are mediated by bosons, which have integer spins. Massless gluons carry a color charge and mediate the strong force. Photons moderate the electromagnetic force. The massive W and Z bosons generate the weak force and are given mass via spontaneous symme-

try breaking and the scalar Higgs boson. The remaining particles are half-integer spin fermions. Fermions come in two varieties: quarks, which can only exist in bound, color-neutral hadrons, and leptons: neutrinos, electrons, muons, and tau particles, which interact via the electroweak interactions and do not have a color charge[3].

Although it describes much of the universe that human beings are capable of observing, there are still many puzzling questions that the Standard Model leaves unanswered. One quite obvious hole is the fact that it does not address one of the most familiar fundamental forces- Gravity, but other puzzles are subtler- For example, the Standard Model does not adequately explain the abundance of matter in the universe. Because the Standard Model, by itself, is quite symmetric with respect to discrete symmetries, charge, parity and time reversal. Because of this, matter and antimatter should be created in equal proportions, only to annihilate each other. There must be some mechanism that could promote matter interactions- This is often referred to as Baryogenesis (Baryons are color-neutral quark triplets. A particle's baryon number is 1/3 the number of quarks, minus 1/3 the number of anti-quarks).

In the mid-1900s, Andrei Sakharov put forth the 3 conditions that any physics model would need to have, particularly in the early universe, in order to generate an excess of baryons. Those conditions, the "Sakharov Conditions," are[4]:

- Interactions that occur outside of a thermal equilibrium
- Interactions that violate Charge(C) and Charge-Parity (CP) symmetry
- Interactions that do not conserve baryon number

Beta decay, via the weak interaction, demonstrates some degree of parity violation. This was shown for the first time experimentally by C.S. Wu, who measured an excess of left-handed electrons when polarized Cobalt-60 atoms decayed into Nickel[5]. This suggested that quarks interacting under the weak interaction might be a source for some of the parity violations necessary to create baryogenesis. Wu's work experimentally validated the theories of C.N. Yang and T.D. Lee, who first hypothesized that left-right parity symmetries might be violated by the weak interaction,

via a mixing of parity eigenstates in the weak interaction Hamiltonian[6]. They won the Nobel Prize for this work in 1957.

The weak interaction was also known, at the time, to vary in strength, depending on whether or not the interaction is purely leptonic, semi-leptonic, or hadronic. Nicola Cabibbo postulated that the flavor eigenstates of the weak interaction mixed according to a rotation angle, in order to generalize the weak interaction and account for this variation. This mixing conserved CP symmetries, and only included the two generations of quarks known to exist- up/down, and charm/strange. Later, Kobayashi and Masakawa extended this concept to include rotation angles associated with the top and bottom quarks- a third generation[7]. These rotation angles can all be organized into a unitary rotation matrix, the CKM matrix[8, 7]:

$$\begin{matrix} |d'\rangle \\ |s'\rangle = \\ |b'\rangle \end{matrix} \begin{pmatrix} V_{ud} & V_{us} & V_{ub} \\ V_{cd} & V_{cs} & V_{cb} \\ V_{td} & V_{ts} & V_{tb} \end{pmatrix} \begin{matrix} |d\rangle \\ |s\rangle \\ |b\rangle \end{matrix} \tag{1.1}$$

The CKM matrix restored generality to the weak interaction and provided a mechanism that allowed quark flavors to mix. If all the values in the CKM matrix were real and lacked imaginary parts, then CP symmetry would be conserved by the weak interaction. The third generation of quarks, however, requires a phase, and this imaginary phase (if non-zero) would constitute a mechanism for generating some of the CP violations in the Standard model[9, 7]. Because of orthogonality and normalization conditions, there are many relations between these quantities to place limits on some when others are measured [10]. Among these is the condition that, if an up quark transforms, it must transform into another type of quark (down, strange, or charm):

$$|V_{ud}|^2 + |V_{us}|^2 + |V_{uc}|^2 = 1 \tag{1.2}$$

Deviations from this predicted sum when measured experimentally would clearly signal physics beyond the Standard Model at work. These deviations would indicate that up quarks could then

couple with other particles. V_{ud} is the largest among these and is currently measured in $0^+ \rightarrow 0^+$ nuclear decays to the highest precision, as this reaction occurs in many different types of nuclei, however, these measurements indicate a 4σ tension with the unitarity condition[11]. Free neutrons make a particularly well-suited candidate for studying at least one piece of this problem because they are cleaner systems, unperturbed by nuclear effects[9]. Measurements of several parameters associated with the beta decay of free neutrons can help to pose limits on the measurement uncertainties associated with V_{ud} and serve as a test of the unitarity of the CKM matrix. These parameters include the neutron lifetime and λ, the ratio between vector and axial-vector coupling constants in the Standard Model.

1.2 Neutrons and Beta Decay

A neutron is a neutral particle comprised of three valence quarks, one positively charged up quark, and two negatively charged down quarks held together under the strong force via gluons. These valence quarks only make up 0.97% of the neutron mass. The gluons inside the neutron also interact and split to create "Sea Quarks," quark-anti-quark pairs whose presence contributes to the neutron mass, but fluctuate in and out of existence through creation and annihilation[12]. Neutrons are just slightly heavier than protons and are most often found bound alongside them inside the nucleus of an atom. The strong force binds protons and neutrons together in an atomic nucleus via a complicated web of interactions, modeled by pion exchanges and other effective field theories. At the short distances inside the nucleus, these interactions overcome the Coulomb repulsion that would otherwise force protons apart and prevent stable elements from forming[13].

When inside this nucleus of an atom, neutrons interact with protons via strong interaction, to produce nuclei. There are many different models that describe how these nucleons organize themselves inside a nucleus, however, one very common method for an unstable nucleus to decay into a more stable one is beta decay, via the weak interaction. Inside a nucleus, several different types of beta decay can occur, involving both protons and neutrons, each yielding slightly different

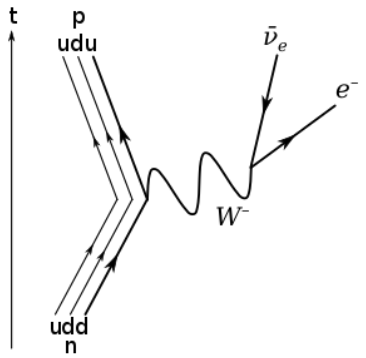

Figure 1.2: The leading order Feynman diagram that describes neutron beta decay, including the spectator quarks. (Image courtesy Wikimedia Commons)

daughter particles[14].

Freed from the nucleus, however, a neutron can only decay via β^- decay, whose products are a proton, electron, and anti-neutrino. The tree-level Feynman diagram for such decay is pictured in Figure 1.2. Schematically, one of the down quarks in the neutron gets converted to an up quark, turning the neutron into a proton. This flavor change happens via the emission of a W^- boson, which then decays into the other daughter products. The other two quarks in the neutron are along for the ride- they are known as "spectator quarks." The spectator quarks are expected to contribute in some way to the interaction. Because quarks are only asymptotically free, spectator quarks will always be present in beta decay[15].

If no assumptions are made about the structure of the weak interaction, such that spectator interactions may be included in the model, and all the possible mathematical operators, O_i with the proper symmetries under Lorentz invariance are allowed (scalar, vector, axial vector, tensor, and pseudo-scalar), the Hamiltonian takes the form[16]:

$$\mathcal{H} = \sum_{i=SVATP} \bar{\psi}_p O_i \psi_n \bar{\psi}_e O_i \left(C_i + C_i' \gamma^5\right) \psi_{\bar{\nu}} + H.C. \tag{1.3}$$

Here, C and C' serve to parameterize the mixing right- and left-handed parts of the interaction and the strength of the interaction. The interaction strength is related to the Fermi constant, G_F, and V_{ud}. [8]. When this Hamiltonian is used to calculate the differential decay rate, summing

over the spin states of the daughter particles, and neglecting the neutrino mass, the result is the following[16, 8]:

$$\frac{\partial w}{\partial E_e \partial \Omega_e \partial \Omega_\nu} = \frac{G_F^2 V_{ud}^2}{32\pi^5} p_e E_e (E^0 - E_e)^2 \left(1 + 3|\lambda|^2\right) \times \left(1 + a\frac{\vec{p_e} \cdot \vec{p_\nu}}{E_e E_\nu} + b\frac{m_e}{E_e} + \vec{\sigma_n}\left(A\frac{\vec{p_e}}{E_e} + B\frac{\vec{p_\nu}}{E_\nu} + D\frac{\vec{p_e} \times \vec{p_\nu}}{E_e E_\nu}\right)\right) \quad (1.4)$$

Each of the parameters, a, b, A, B, and D are related to the coupling constants from the Hamiltonian, as listed in the appendix of reference [16], the paper by Jackson, Treiman, and Wyld. The complexity of these relations can be reduced by noting that in nature, two types of beta-minus decay can be observed, based on how the lighter daughter particles carry off angular momentum (Fermi and Gamov-Teller transitions). This implies that interactions in the Standard Model take only two forms of the operators in the original Hamiltonian. The left-handedness of neutrinos and other particle interactions further defines the limits on the palette of operators beta decay can be built from to be vector-minus-axial-vector (V-A) form[17], and in fact, those two parts are separable-Gamov-Teller decays are considered purely axial, and Fermi transitions are vector[9, 18]. This reduction dictates that b is zero, as it relates only to scalar and tensor interactions at first order.

The other parameters in equation 2.2 can be described using the ratio between vector and axial vector coupling constants, $\lambda = \frac{g_A}{g_V}$, and a complex phase, ϕ[8].

$$a = \frac{1 - |\lambda|^2}{1 + 3|\lambda|^2}, A = \frac{-2\left(|\lambda|^2 + |\lambda|\cos\phi\right)}{1 + 3|\lambda|^2}, B = \frac{-2\left(|\lambda|^2 - |\lambda|\cos\phi\right)}{1 + 3|\lambda|^2}, D = \frac{2|\lambda|\sin\phi}{1 + 3|\lambda|^2}, \quad (1.5)$$

Measurements of the parameters λ, and V_{ud}, are signposts in the search for physics beyond the Standard model. They are measurements that can be made which may indicate where further study is needed to understand the puzzles that remain in the Standard Model. These parameters are also incredibly important in understanding and placing limits on the discrepancy in the neutron lifetime between the beam and bottle-type measurements. Those discrepancies will not be included in

the scope of this work, however we will note here that these parameters are related by the fermi function, f, the mass of the electron, and some radiative corrections, δ_{RC}[19]:

$$\frac{1}{\tau_n} = \frac{|V_{ud}|^2 G_f^2}{2\pi^3} m_e^5 f \left(1 + \delta_{RC}\right) \left(1 + 3\lambda^2\right) \tag{1.6}$$

Figure 1.3 shows measurements of g_A (a proxy for λ because $g_v = 1$ under the conserved-vector-current hypothesis at zero momentum transfer[8]), and $|V_{ud}|$ from several experiments contribute to the picture that is forming around the intersection of CKM unitarity and physics beyond the Standard Model[19].

The Nab experiment, described in the following chapter, uses unpolarized neutrons to measure a and b from equation 2.2, and therefore λ in order to better understand the limits where CP-violating interactions may operate inside the weak interaction. Measurements like these constitute the "Precision Frontier" in searches for physics outside the Standard Model. They use precise measurements of quantities that can be cross-checked with different experiments, or predicted by theory, to search for places where deviations or disagreements may occur. These types of interactions are difficult to probe with energy frontier-based experiments, like those carried out at the LHC[11].

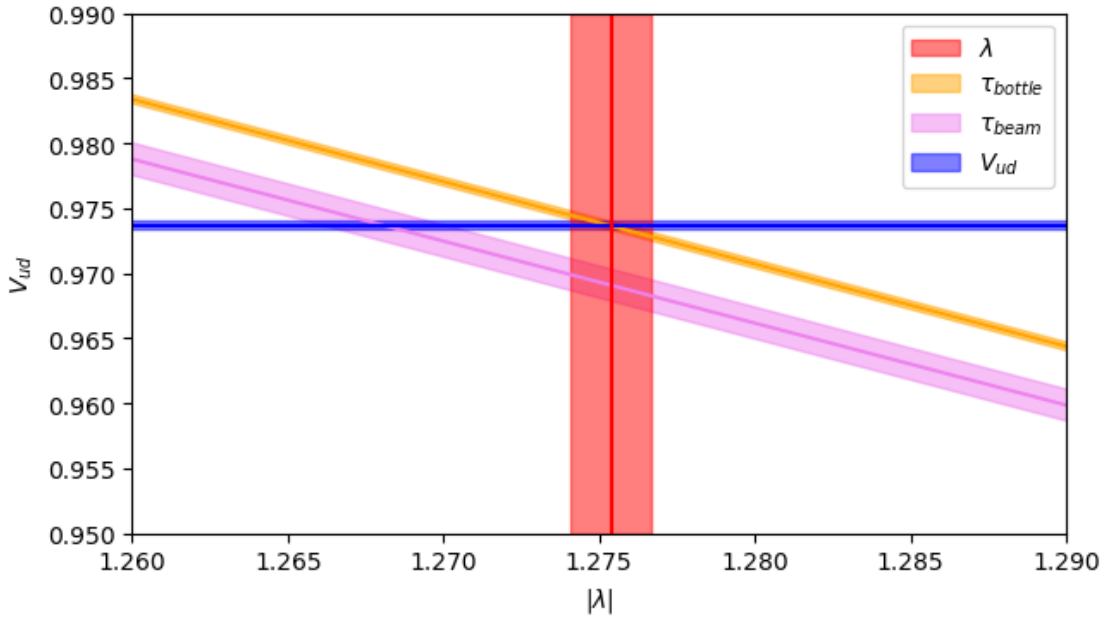

Figure 1.3: A plot of the phase space of λ and V_{ud} constraining CKM unitarity. Here the red section represents the most recent average for λ from [20], 1.2754 ± 0.0013, the blue represents the most recent value of V_{ud} from [21], 0.97373 ± 0.00031, and the violet and orange regions are derived from bottle and beam neutron lifetime measurements of 879.4 ± 0.6s [20] and 887.7 ± 2.2s [22], respectively.

CHAPTER 2

The Nab Experiment

The Nab Experiment aims to precisely measure two important parameters associated with the unpolarized beta decay of free neutrons. The first is the electron-neutrino correlation coefficient, which describes how the unpolarized decay rate couples to the angle at which the electron and neutrino leave the decay. The second is *b*, the Fierz Interference Term, which relates to distortions in the energy spectrum of the daughter electron. The experiment will take place on the Fundamental Physics Neutron Beam (FnPB), beam line 13 at the Spallation Neutron Source (SNS) at Oak Ridge National Lab, and relies on the use of a magnetic spectrometer that maps the amount of time the proton spends in this spectrometer to its energy. This chapter will discuss the motivation behind this experiment, the principle behind the measurement, and some of the major systems associated with the apparatus and the measurement itself.

2.1 Motivation

The previous chapter discussed the derivation of the expression for the differential decay rate of beta decay of the free neutron. This expression is repeated here for reference[23, 16, 8]:

$$\frac{\partial w}{\partial E_e \partial \Omega_e \partial \Omega_\nu} = \frac{G_F^2 V_{ud}^2}{32\pi^5} p_e E_e (E^0 - E_e)^2 \left(1 + 3|\lambda|^2\right) \times \left(1 + a\frac{\vec{p_e}\cdot\vec{p_\nu}}{E_e E_\nu} + b\frac{m_e}{E_e} + \vec{\sigma_n}\left(A\frac{\vec{p_e}}{E_e} + B\frac{\vec{p_\nu}}{E_\nu} + D\frac{\vec{p_e}\times\vec{p_\nu}}{E_e E_\nu}\right)\right) \tag{2.1}$$

This equation contains various parameters that couple the momenta of the daughter particles to the differential decay rate via combinations of Standard Model coupling constants, including G_F, the Fermi Constant, V_{ud}, and λ the ratio of vector to axial-vector coupling constants. A more precise understanding of these coupling constants can help to place limits on uncertainties associated with discrete symmetry breaking and CP violations in the Weak interaction, and motivate searches for exotic scalar and tensor interactions as described in Chapter 1.

Nab's primary measurement is of the electron-neutrino correlation coefficient, a, which can be expressed in the Standard Model as a function of λ as [24]

$$a = \frac{1 - |\lambda|^2}{1 + 3|\lambda|^2} \tag{2.2}$$

According to the Particle Data Group's latest publication, [20], measurements indicate that $a = -0.1049 \pm 0.0013$. Nab aims to measure a at the 0.1% level ($\delta a/a = 0.001$). If Nab successfully completes their measurement of a, their corresponding fractional uncertainty in λ will be 3×10^{-4}[24]. Some of the most precise calculations of λ come from measurements of beta asymmetry A, with polarized neutrons, from experiments like PERKKEO[25] and UCNA[26].

It should be noted here again that the expression for a and the coupling constants in equation 2.2 as expressed terms of λ in 1.5 are truncated to exclude the coupling constants from scalar and tensor interactions because these interactions are not considered part of the weak interaction under the Standard Model.

$$a = \frac{|M_F|^2 \left(|C_V|^2 - |C_s|^2\right) - \frac{1}{3}|M_{GT}|^2 \left(|C_A|^2 - |C_T|^2\right)}{|M_F|^2 \left(|C_V|^2 + |C_s|^2\right) + |M_{GT}|^2 \left(|C_A|^2 + |C_T|^2\right)} \tag{2.3}$$

Here M_F and M_{GT} are the matrix elements from Fermi and Gamov-Teller transitions, respectively[27, 16]. Disagreements between measurements of λ as extracted from a, A, and B could signal a need to further include exotic scalar and tensor interactions as part of the structure of the weak interaction.

Many nuclear experiments use measurements of the energy spectrum of the ion (nucleus) re-

sulting from a beta decay to examine the energy spectrum of the resulting ions to determine values for the vector or axial vector coupling constants, but these measurements are made in much more complicated systems and have to include corrections from many other nuclear interactions. Nuclei used for these kinds of measurements include proton-rich isotopes of light noble gasses and other light metals[11]. These lighter nuclei make good candidates for comparisons between measurement and calculation, as some possess convenient nucleon symmetries that allow the nuclear structure to be calculated more easily[27]. The Beta-decay Paul Trap, at Argonne National Lab uses ^{8}Li and ^{8}B measures coincidences and momenta of the daughter particles as these nuclei undergo Gamov-Teller decay transitions. They aim to place limits on tensor interaction couplings at the 0.1% level[28]. ^{6}He and ^{6}Li also undergo Gamov-Teller decays, and are studied at CERN's ISOLDE facility uses produces various isotopes of Argon, which can be used to probe both Fermi and Gamov-Teller transitions. They aim to measure these two contributions to a separately, with a precision of 10^{-3}, and with some improvements may also be able to measure the Fierz Interference term, b[29]. These experiments are competitive with Nab and the other free neutron experiments that aim to measure a.

Previous measurements of a in free neutrons include the aSPECT experiment at the Institut Laue-Langevin, and the aCORN at the National Institute for Standards and Technology. aSPECT uses a magnetic adiabatic collimation with an electrostatic filter (MAC-E) system, which takes the momenta of the protons generated by beta decay from a continuous reactor source, and directs them along a magnetic field. A retarding potential is then applied to produce a threshold, blocking protons below a specified energy from making it to a detector. By varying this threshold, the proton energy spectrum can be measured, and fit to extract a, and therefore, λ. Their latest measurement of a is -0.10430 ± 0.00084 (approximately a 1% measurement) yielding a λ value of 1.2677 ± 0.0028[30]. The aCORN experiment uses a nearly uniform magnetic field to guide daughter particles to specific ends of a collimating chamber. At one end of the chamber, the electron energy is measured via a scintillation detector, and at the other end, protons are collected, and their time-of-flight is recorded, based on when the relativistic electron was detected.

Because of the 3-body kinematics associated with the beta decay, when the proton time of flight is plotted with respect to the energy of the electron, a characteristic "wishbone" shape emerges, each branch of the wishbone corresponding to a spatial region that would contain the undetected neutrino- A 'fast proton' region, where the proton and the neutrino move in opposite directions, and a 'slow proton' region, where they move in roughly the same direction. The asymmetry in the wishbone shape at different energies here can be used to extract a. As of 2020, they obtained a value for $a = 0.10782 \pm 0.00182$ (approximately a 1.7% measurement). The corresponding result for $\lambda = 1.2796 \pm 0.0062$.[31]. The Nab experiment's measurement of a is an important improvement on and cross-check of these previous measurements, as the methods used here are associated with different systematic errors.

As noted in the derivation in Chapter 1, the Fierz Interference term, b, term is only nonzero if scalar and tensor interactions are present in Weak decay. These interactions are not currently included within the Standard Model, which is only formulated to include vector and axial-vector interactions. A nonzero value for b would indicate that other interactions contribute to neutron beta decay, and could help to explain discrepancies in neutron lifetime measurements, as well as pose limits on searches for completely new physics. In the Nab experiment, b can be determined from a careful examination of the electron spectrum, and a comparison of the measured electron spectrum with the electron spectrum expected for $b = 0$.[32]. The Nab measurement of b will be a first of its kind among free neutrons. The only other evaluation of b in free neutrons was determined from an analysis of the beta spectrum from the PERKKEO III experiment, which used polarized neutrons to measure the beta asymmetry, A [23]. This analysis determined $b = 0.017 \pm 0.020$. This measurement was limited by statistics and had to reject a large segment of data because of other experimental effects[23]. Other experiments that aim to measure Fierz interference with a precision goal similar to Nab include NOSMOS, which uses an RxB magnetic spectrometer to measure the drift velocities of the daughter particles[33], and PERC, which will make improvements on the PERKKEO measurement[34].

Other limits on b have been placed by measurements of Fermi and Gamov-Teller decays in

different kinds of nuclei, but those limits remain consistent with a zero value[32]. These nuclei include ^{45}Ca, which was studied in close conjunction with the Nab experiment, as it uses similar detectors, methods for precisely determining the electron energy, and methods for extraction of b. They determined $b = 0.40 \pm 0.05$stat, $+0.78, -0.47$sys.[27]. Other promising nuclei for a measurement of Fierz interference at the 0.1% level include ^{6}He, ^{14}O, ^{19}Ne, $^{2}0$F, and ^{114}In[11].

2.2 Nab Measurement Principle

If the terms that couple to the polarization are neglected, Equation 2.2 becomes:

$$\frac{\partial w}{\partial E_e \partial \Omega_e \partial \Omega_\nu} \propto 1 + a\frac{\vec{p_e} \cdot \vec{p_\nu}}{E_e E_\nu} + b\frac{m_e}{E_e} \tag{2.4}$$

The term that couples the dot product depends on the momenta and energy of the electron and anti-neutrino, however, since the anti-neutrino doesn't interact with much in this universe, and would be incredibly difficult to measure, this relationship must be recast in terms of the proton energy and momenta. The dot product $\vec{p_e} \cdot \vec{p_\nu}$ can also be expressed as

$$\vec{p_e} \cdot \vec{p_\nu} = |\vec{p_e}||\vec{p_\nu}| \cos\theta_{e\nu} \tag{2.5}$$

where $\theta_{e\nu}$ is the angle between the momenta of the electron and neutrino as they leave the collision. When a neutron decays at rest (in its rest frame), momentum and energy are conserved. The momenta of the daughter particles add up to zero- the vectors that represent them form a closed triangle. The Law of Cosines dictates that their momentum is related to $\cos\theta_{e\nu}$ as:

$$\cos\theta_{e\nu} = \frac{p_p^2 - p_e^2 - p_\nu^2}{2|p_e||p_\nu|} \tag{2.6}$$

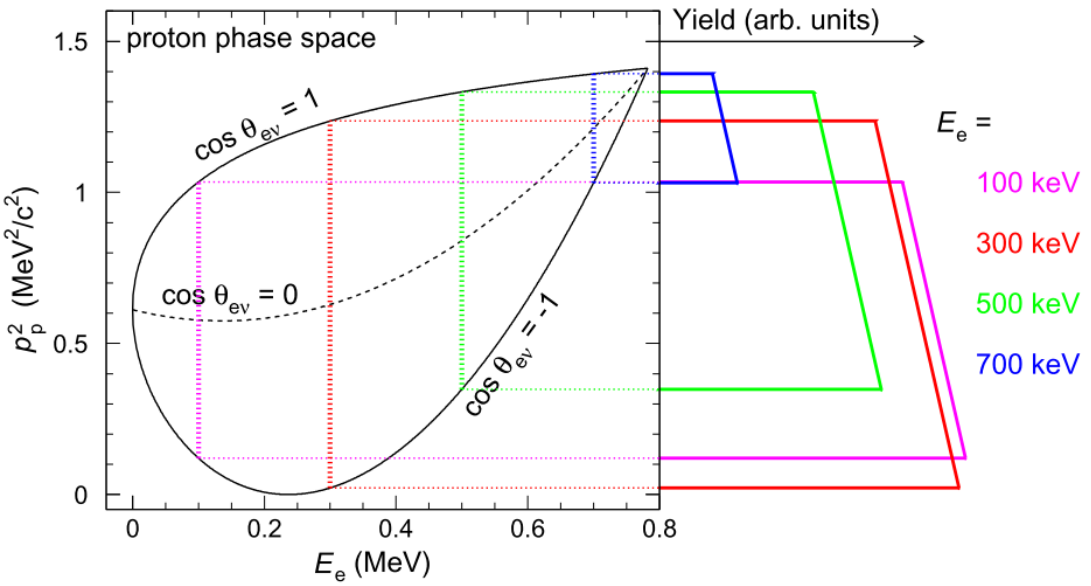

Figure 2.1: A plot of the phase space of the experiment, in proton-momentum-squared (p_p^2), and electron energy (E_e). This characteristic teardrop shape is defined by the limits of $\cos\theta_{e\nu}$. When cuts to this phase space are made along specific values of E_e, the slope across of the trapezoid formed is related to a. Image reproduced from [24] with permission.

This relation also demonstrates that equation 2.4 can further be expressed as:

$$\frac{\partial w}{\partial E_e \partial\Omega_e \partial\Omega_\nu} \propto 1 + a\frac{p_p^2 - p_e^2 - p_\nu^2}{2E_eE_\nu} + b\frac{m_e}{E_e} \tag{2.7}$$

Because the energy of the neutrino is related to the energy of the proton and the electron via the Q-factor of the decay, this is linear with respect to p_p^2 for specific values of the electron energy, E_e. This also leads to a particularly well defined shape in the phase space, as pictured in Figure 2.1. This is sometimes referred to as the "Teardrop Plot"- the outer edges of the phase space (where $\cos\theta_{e\nu} = \pm 1$) form a teardrop shape. If this phase space were a cake, and one were to cut the cake at various electron energy levels, one would find that the cross-section of the slice would be linear across the top, with a slope related to a and the electron energy where the cake was cut.

The Nab experiment performs coincidence measurements of the daughter protons and electrons. When a neutron decays inside the decay volume of the spectrometer and the electron is headed towards the lower silicon detector, its energy is recorded and a clock begins ticking. If the associated

proton is headed in the opposite direction, towards the upper detector, the clock stops when the proton reaches the upper detector, measuring the proton time-of-flight (TOF). This works because the electron is relativistic, and the time it takes to get to the lower detector from the decay volume is negligible in comparison to the proton. The proton does not have enough energy for the energy or momentum to be measured accurately in the upper detector, but because of the properties of the magnetic spectrometer, the time it spends traversing the magnetic field can be mapped back to the proton momentum- This is the primary task of the Nab analysis methods when measuring a.

The Fierz Interference term, b can be deduced from a careful examination of the energy spectrum associated with the electrons produced by the beta decays in the experiment. Because Nab uses coincidence counting to determine which events to include in analysis, this lowers backgrounds, and improves sensitivity to lower energy electrons, where a deviation in the spectral shape due to a non-zero b will be most pronounced[32]. It can also be examined as part of the intercept from data collected at each energy level, when examining the proton decay data to determine a, although this method is made slightly more difficult because of the detector response functions to the proton[17].

2.3 The Experiment

Neutrons for the Nab experiment are created when a short pulse, approximately 1μs, of protons from an accelerator source strikes a Mercury target at the center of the SNS facility at roughly 1GeV. Each mercury-proton interaction serves up 20-30 hot, fresh neutrons, which are then cooled by a liquid hydrogen moderator to a more reasonable 20K [35]. These cold neutrons travel through several segments of different supermirror guides, some of which curve the path of these neutrons, so that the experiment at the end of the beamline does not have a direct line of sight to the moderator and target. This bending reduces backgrounds from unmoderated fast neutrons and gammas produced in the target.

The guides that bring neutrons to the Nab experiment also contain a monochromator, which can

be inserted along the guide to sip off $8.9\mathring{A}$ neutrons, diverting them to a slightly different guide (BL13-A), for an experiment on the neutron dipole moment[36]. The rest of the neutrons travel along BL13-B to the heart of the Nab spectrometer magnet, where a portion of them will decay. The Nab experiment expects to see 1600 decays/s, of which 200 will be pointed in the proper direction for the spectrometer to guide the daughter particles to the detector[24].

2.3.1 The Spectrometer

The Spectrometer for the Nab experiment a 7m tall superconducting magnet. The superconducting coils are made of niobium-titanium, cooled to 4K, and are designed to operate with 137A of current. At the time of its design and construction, it boasted the title "World's Largest Cryogen-free Super Conducting Magnet," according to the CRYOGENICS Ltd, because it uses gaseous helium as its main coolant. It can also be pre-cooled by a liquid nitrogen loop[37].

The magnetic field inside the spectrometer is nominally vertical and about 1.7T in the decay region, where the neutron beam passes through the spectrometer bore. The field above the decay region increases to 4T, and curves strongly. This curve acts as a filter preventing protons from the decay with too shallow of an angle (and thus a very long TOF) from reaching the detector. Past the curve, the field magnitude decreases, and the field lines expand. This field expansion "longitudinalizes" the proton momentum, so that a majority of the proton momentum is focused in the vertical direction, and contributes to the TOF measurement. Near the detector, the magnitude of the field increases back to 1.5 T, to complete the field guide, and focus the protons on the area of the detector. Below the decay volume, the field decreases only slightly (to about 1T, to focus and guide electrons from the decay to the lower detector.

In order to boost the momenta of the proton and the electron, so they are more effectively detected by the silicon detectors, the top and bottom of the spectrometer also contain electrodes that apply an accelerating voltage to the particles just before they hit the detector. Figure 2.2 shows a picture of the magnet, and a plot of the electric and magnetic fields [17].

The goal of the Nab spectrometer is to guide protons to the detector in such a way that the time

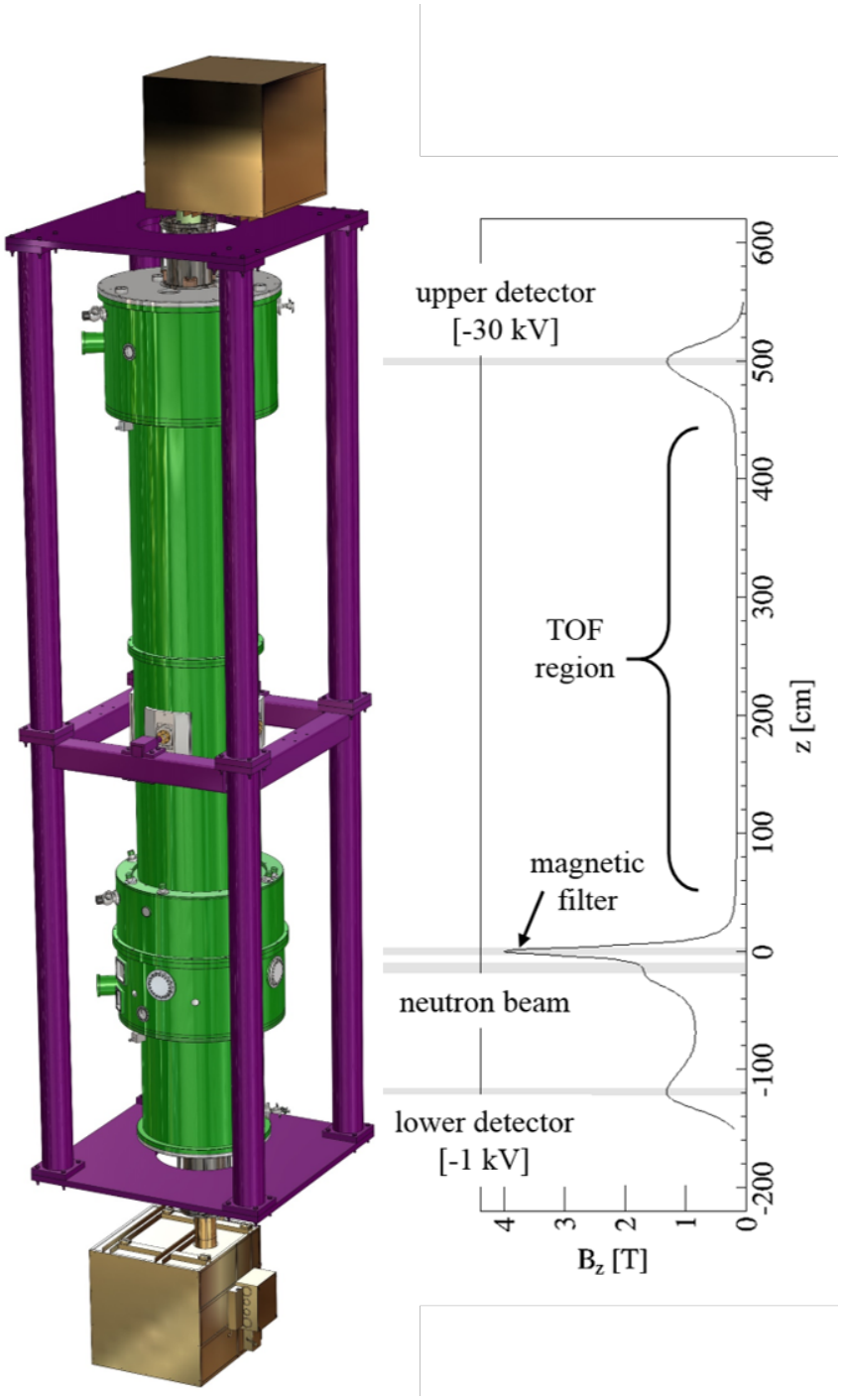

Figure 2.2: Left: a CAD image of the spectrometer cryostat (green) and its flux return (purple). Pictured above and below the spectrometer are the high-voltage cages for detector equipment. Right: a plot of the designed field magnitude at the center of the bore tube. Image courtesy A. Jazghani

it takes them to get there is still related to their momentum. In the simple case that the protons travel straight up towards the center of the detector, that time of flight is:

$$t_p = \frac{m_p L}{p_p} \tag{2.8}$$

Here, L is simply the vertical distance between where the proton was born in the decay region, and the detector. Things get more complicated as the protons leave the decay at some angle to the field, θ_0. Since the magnetic field is conservative, it cannot do any work on the proton. It has no effect on the parallel component of the proton's momentum. If the field were uniformly vertical, then the time of flight would become:

$$t_p = \frac{m_p L}{p_p \cos\theta_0} \tag{2.9}$$

In this case, there are many possible values for the proton momentum that could lead to a particular measured time of flight- both slower protons with a shallow angle, and faster protons with a higher angle could reach the detector in the same amount of time. How can these different paths be distinguished? One way to start accomplishing this is to longitudinalize the momentum of the proton so that a larger proportion of the momentum lies along the field. This requires changing the curvature and strength of the field and is what the Nab spectrometer is designed to do.

The magnetic field is conservative and does no work on the proton. It can't affect the parallel component of the proton's momentum, but it will bend the trajectory of the perpendicular component to move in a circle about the field. The radius of the path that a proton takes is related to the component of the momentum that is perpendicular to the field:

$$R = \frac{p_\perp}{qB} = \frac{p \sin\theta}{qB} \tag{2.10}$$

This moving charge looks like an effective current loop that circulates around the magnetic field

lines, I_{eff} with a magnetic moment, μ

$$I_{eff} = \frac{qp \sin\theta}{2\pi R m} \tag{2.11}$$

$$\mu = IA = \frac{qp \sin\theta R}{2m} = \frac{p^2 \sin^2\theta}{2mB} = \frac{T \sin^2\theta}{B} \tag{2.12}$$

When B changes, the radius of the proton orbit will change, but this changes both the current and the effective area in opposing ways, so the magnetic moment is an adiabatic invariant, which means that changing the field strength can change the angle of the proton's momentum with the field.

$$\sin^2\theta_2 = \frac{B_2 \sin^2\theta_1}{B_1} \tag{2.13}$$

This relationship describes the longitudinalization of the proton momentum. If the proton travels from a high field region to a lower field region ($B_1 > B_2$), then the angle between the field and the proton momentum will decrease, and a larger portion of the proton momentum will reach the detector. If $\cos\theta$ changes sign, the particle momentum can change from being positive to negative- It will be reflected away from the upper detector. This condition also leads to equation 2.14- the field conditions for reflecting protons that will spend too much time in the TOF region.

$$\cos\theta_{0,max} \geq \sqrt{1 - \frac{B_0}{B_F}} \tag{2.14}$$

Here B_0 is the value of the field in the decay region, and B_F is the value of the field at the filter peak. For the Nab spectrometer, $\cos\theta_{0,min}$ is 0.75, $\theta_{0,min} \approx 40^0$. Protons with a larger angle than this value have a higher probability of spending a longer in the time-of-flight region than the time between expected events and could interfere with the experiment's ability to distinguish coincidence counts.

Now that the proton's momentum is longitudinalized, the trajectory of the proton can be found in relation to the specific fields it experiences as it travels through the spectrometer. Using the conservation of energy in the fields one can find the following relation which describes the longitudinal

component of the proton momentum as a function of position inside the magnet, z:

$$p_{||} = p_0\sqrt{1 - \frac{\sin\theta_0}{B_0}B(z) - \frac{q}{T_0}(V(z) - V_0)} \tag{2.15}$$

The time, dt, a particle takes to go from z to $z + dz$ can be expressed as

$$dt = \frac{m_p dl}{p_{||}} = \frac{m_p dz}{p_0\sqrt{1 - \frac{\sin\theta_0}{B_0}B(z) - \frac{q}{T_0}(V(z) - V_0)}} \tag{2.16}$$

This expression can be integrated to find the total flight time, and then inverted to extract the proton momentum squared from a time-of flight measurement:

$$t_p = \frac{m_p}{p_0}\int_{z_0}^{L} \frac{dz}{\sqrt{1 - \frac{\sin\theta_0}{B_0}B(z) - \frac{q}{T_0}(V(z) - V_0)}} \tag{2.17}$$

$$p_0^2 = \frac{m_p^2}{t_p^2}\left[\int_{z_0}^{L} \frac{dz}{\sqrt{1 - \frac{\sin\theta_0}{B_0}B(z) - \frac{q}{T_0}(V(z) - V_0)}}\right]^2 \tag{2.18}$$

This extraction, of course, also relies on knowledge of of the decay, z_0 and the angle between the field and the proton at the time of decay, θ_0. These parameters cannot be measured by the Nab Experiment. Instead, the proton momentum squared can be thought of as a distribution related to the time of flight and the spectrometer response function, $\Phi(t_p)$. This spectrometer response function can be constructed in two ways.

The first of these methods, Method A, relies on expanding the integral in equation 2.18 into a series of parameters that can be fit to describe the spectrometer response for specific electron energies. The data to fit here is generated by highly detailed GEANT4 simulations of the propagation of protons through a simulated version of the spectrometer field. The second method, Method B, relies on constructing a fit of the field data, and calculating the spectrometer response function analytically from those fits[17, 32]. Both of these methods require precise knowledge of the field itself, and important characteristics of the field, like the ratio between the magnitudes of the field at the filter peak, and in the decay region and the TOF region. The portion of the experimental

uncertainty related to these quantities is given in Table 2.1.

Parameter	**Specification**	**Systematic Uncertainty** ($\Delta a/a$)
Field Curvature at Filter	$\frac{\Delta\gamma}{\gamma} = 2\%$with $\gamma = \frac{\frac{d^2 B_z(z)}{dz^2}}{B_z(0)}$	5.3×10^{-4}
Field Ratio $r_B = \frac{B_{TOF}}{B_F}$	$\frac{\Delta r_B}{r_b} = 1\%$	2.2×10^{-4}
Field Ratio $r_{DV} = \frac{B_{DV}}{B_F}$	$\frac{\Delta r_{DV}}{r_{DV}} = 1\%$	1.8×10^{-4}

Table 2.1: Parameters related to the magnetic field of the spectrometer and how they relate to the systematic uncertainty for the Nab measurement of a. Here B_{TOF} is the magnitude of the field in the middle of the time-of-flight region, B_F is the field magnitude at the filter peak, and B_{DV} is the magnitude of the field in the decay volume. [24]

In order to confirm that the field produced by the magnet matches the fields used to simulate the spectrometer response, and that it also conforms to the parameters associated with the uncertainties in the overall experiment, a precision magnetometry measurement was carried out. The field of the magnet was measured both on and off the central axis in several key regions. These measurements were then used to construct an expansion using modified Bessel functions as a basis. These functions were excellent candidates for mapping the field because of the spectrometer's cylindrical symmetry[17].

Performing this measurement was no small feat, and presented many challenges. One of the few devices that can accommodate measuring a field that ranges in magnitude from 0.001-4 T, with adequate precision is a small hall probe. In order for the hall probe that measures the field to function properly and stay calibrated, it has to operate at room temperature, but the bore of the magnet operates at closer to 70K[17]. To accommodate this, a large inverse dewar was inserted through the bore of the magnet, so that a trolley containing the hall probe could be raised and lowered through the bore tube at room temperature. This restricts the measurements that can be taken, and excludes certain regions of the full field from being mapped directly (hence the need for the expansion). The type of hall probe used is subject to the Planar Hall Effect, wherein, the probe cannot accurately measure the field's magnitude if the field is not perpendicular to the probe. This is not as big of a problem along the axis of the magnet, where the field is vertical, but for off-axis measurements, the probe must be tilted in order to align itself perpendicular to the field- to tilt

the probe, it was mounted inside the trolley on a pivoting table, and controlled with puppeteering strings from the roof of the magnet. These strings adjust the tilt angle until the reading from the probe was maximized, indicating alignment with the field. The trolley containing the probe also had to be tracked with a laser positioning system because the supports that move the trolley don't allow for precise control of the positioning. Analysis for magnetometry is underway. Current issues revolve around the fact that the axis of the measurements isn't exactly the true axis of the field, which means that expansions taken from different measurements (on axis vs off axis) only agree with each other at the 10^{-2} level. If the measured field data can be interpolated, and the true axis can be found, it is likely that this discrepancy can be eliminated[17].

2.3.1.1 Spectrometer Operation

In order to operate the magnet, it must be first evacuated, and cooled down to the desired temperature. This process is expected to take approximately 140 hours to complete, however it depends upon the orientation of the magnet, and the pressures of the various cooling gasses during operation. Adding small doses of nitrogen and helium to adjust the system pressure can help speed up the cooling process. The temperatures at various points inside the magnet are monitored continuously, however, it's worth noting that none of the temperature sensors sample the direct temperature of the coils- There are several which are very close to the coils, but they are on the outside of the insulation of the coil, and often sit at a temperature slightly higher than 4K.

Once the magnet is cooled, it can be energized. The spectrometer is divided into 4 circuits, LDET, UDET, Main, and Trim. The LDET and UDET coils generate the fields nearest the detectors. The Main operates the TOF region, as well as the coils that generate the high fields in the decay region and filter peak. The Trim circuit powers two smaller coils around the decay volume that are designed to be used in systematic testing, to vary the field outside of standard operating parameters. When a circuit is energized, a small section of the superconducting coil is heated by a heating coil, so that that small section is no longer superconducting. This opens the connection between the coils and the power supply so that a desired current can be started in the coil. Once

the desired current is reached, the heater is powered off, and the coil returns to a superconducting state, with the desired current circulating through the coil. This process is managed by the software that operates the magnet, and can also be used to adjust the current once the magnet is energized- The software increases the current in the power supply to match the current in the magnet. Then the heaters turn on and connect the magnet coils to the power supply. The current in the power supply is adjusted to the desired level, which in turn changes the current in the superconducting coils, and then the heaters turn off, the coils cool, the connection to the power supply is broken, and the power supply returns to its default state of zero current.

Powering up all the coils for full operation is a delicate process, as the heat load on the magnet must be carefully managed. If too much heat is generated in the process it is easy for the magnet to quench, and stop superconducting. Because the coolants in the magnet are already gaseous, this magnet does not release a characteristic plume of cooled gas when it quenches like many other superconducting magnets. Instead, it quietly stops conducting and dumps the energy in its circulating current as heat. This heats up the coils further, and they must be cooled back down into a super-conducting state before attempting to re-energize the magnet. Quenching does not just take up time-it is also bad for the health of the coils, and too many quenches may damage the superconductors. Diode circuits and other protective circuitry inside the magnet exist as a protective measure to prevent the current from changing too quickly during a quench. Quench conditions are recorded by the software that controls the magnet power supply and monitors its temperature, however, because the temperature is monitored in discrete intervals, and the temperature sensors are not directly in contact with the superconducting coils, it is usually the case that stored temperature data does not yield enough data to analyze precisely what quenches at the instant of a quench.

There are many things that can add heat to the magnet. The heaters, of course, add some heat to the system. The rate that the current changes can also affect how fast the system heats up and can unbalance the cooling load. As such, it is best practice to slow the rate at which the current is increased during the ramp. It is also common to pause at several points during a ramp to let the magnet cool down before proceeding to increase the current to its operational value. When a ramp

is paused, the temperature data recorded by the magnet software often reveals that temperatures will oscillate, passing heat from one coil to another, until the system settles back into a cooling equilibrium. Changing currents in one coil can also heat the other coils with induced currents during a ramp- so coils that are not actively being ramped may quench when the field is changing.

This magnet is also thought to occasionally exhibit a behavior known as "training quench." A training quench is a quench that occurs when attempting to energize the magnet after it has undergone a significant configuration change, and needs to adapt to a new position or heat load. The coils inside the magnet are mounted somewhat flexibly because the system needs to be able to adapt to a large range of temperature changes. When something happens to the magnet, like turning it from horizontal to vertical, or adding equipment near the bore tube (like installing the magnet inside the passive shielding or installing the detectors)- That can change the alignment of the magnet coils by just a little bit. Occasionally, when the coils shift back into their equilibrium positions, under the immense magnetic forces the coils exert on each other, some local friction can cause a small amount of heat and trigger a quench.

2.3.2 The Detectors

The Nab experiment uses two large-area, pixelated, thin dead-layer silicon detectors to count the products of the neutron beta decay. They were constructed by Micron Semiconductors Ltd, and composed of n-type on n-type doped silicon. In order to meet Nab's precision goals, they have to have a timing resolution on the order of 100ps, and an energy resolution of a few keV. In order to capture all the decay products that travel through the spectrometer, they have a diameter of about 11.5cm[38]. The pixelation of these large area detectors breaks that space up, and allows for better reconstruction of the electron energy, as electrons may bounce from one detector to another, depositing energy in each detector with each bounce[39, 32] See figure 2.3 for a photo of one of these Nab detector plates[17]

When a proton or electron nears the end of the spectrometer bore, it gets accelerated by a constant voltage electric field (see figure 2.2). This electric field boosts the speed of each particle,

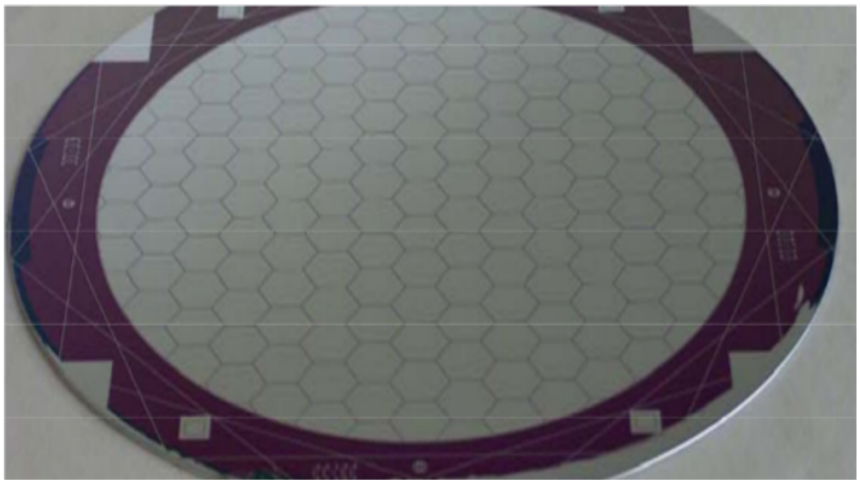

Figure 2.3: A photo of the pixelated detector plate. Image reproduced from [17] with permission

giving it a little bit more energy so that it can overcome the thin dead layer of the detector and deposit its energy. At the top of the spectrometer, where the detectors are mostly concerned with detecting non-relativistic protons, that accelerating potential is about -30kV. This is because the end point energy of the proton is only about 751eV– too small to accurately be detected by the detectors. The electrons do not technically require an accelerating voltage to be detected- its endpoint energy much much larger (700keV), but the -1kV bias is placed in the lower detector region to help prevent protons that that are reflected from the spectrometer filter from backscattering off the lower detector[39, 38].

Once the charge of the beta decay products is deposited in the front layers of the detector, electron-hole pairs in the semi-conductor material are set into motion, creating characteristic pulses associated with each kind of charge, and in the case of electrons, their energies. The motion of these charge carriers is then picked up and amplified by other FET electronics, and eventually digitized and stored for analysis. Figure 2.4 shows a schematic of the detector electronics, and how the system that's internal to the spectrometer magnet is assembled.

Because these detectors interface with the spectrometer magnet, they must be cooled. This cooling also helps to reduce thermal noise inside the detectors. This cooling is difficult to achieve, as all the electrical components associated with the detector come with a heat load. Mitigating this

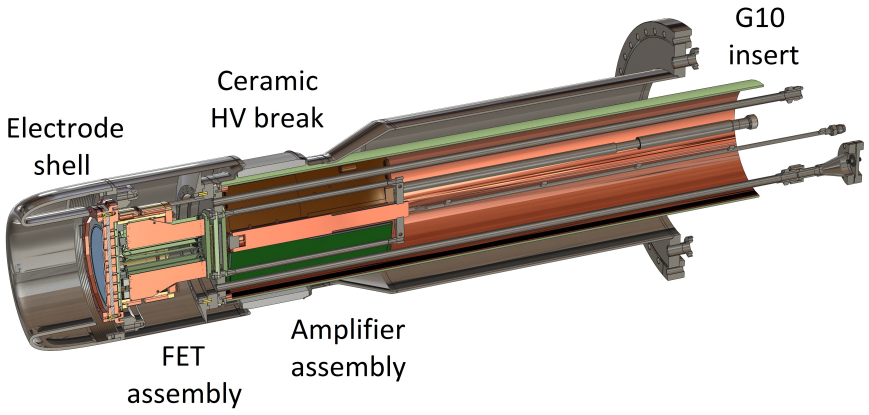

Figure 2.4: A schematic of the detector assembly, including the high-voltage electrodes which produce the accelerating potential, the silicon detector plates, and the FET assembly. Image courtesy the Nab Collaboration

heat load requires a sophisticated cooling system. Work is still ongoing to determine the best way to control the temperature of the detectors.

2.4 Neutron Polarization and the Nab Experiment

The subject of the rest of this thesis is neutron polarimetry. The Nab experiment's measurement of a requires unpolarized neutrons. It is clear from equation 2.2 that effects from the other terms that couple to the neutron polarization may affect the momentum spectra that Nab aims to measure- If the polarization of the neutron beam were zero, then the other terms in 2.2 would not affect the Nab measurement.

Because the neutrons are produced via spallation, it is a fairly safe assumption that the neutrons are unpolarized. However, the nickel guides that help guide the neutrons to the experiment may carry some residual magnetization which can polarize some of the neutrons along their path. It is currently unknown how often these interactions may occur. The bare polarization of the beamline where the Nab experiment takes place has not yet been measured.

What kind of problem would a residual beam polarization cause the Nab experiment? The answer to this question lies in the terms from equation 2.2 that couple to the polarization of the

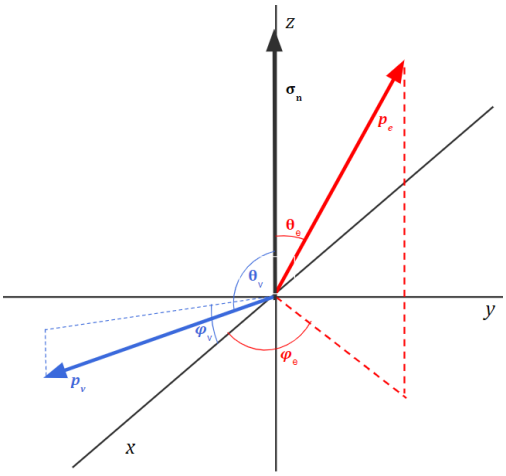

Figure 2.5: The relationship between the angles of the neutron spin and the electron and antineutrino momentum, where $\cos\theta_{e\nu}$ is the angle between the electron and neutrino momenta themselves (not pictured) $\cos\theta_\nu = \cos\theta_{e\nu}\cos\theta_e + \sin\theta_{e\nu}\sin\theta_e\cos\phi_e - \phi_\nu$

neutron:

$$\frac{\partial w}{\partial E_e \partial\Omega_e \partial\Omega_\nu} \propto \vec{\sigma_n}\cdot\left(A\frac{\vec{p_e}}{E_e} + B\frac{\vec{p_\nu}}{E_\nu} + D\frac{\vec{p_e}\times\vec{p_\nu}}{E_e E_\nu}\right) \tag{2.19}$$

The parameter D is predicted by the Standard Model to be zero, as it pertains to effects that would violate time reversal invariance. All of the most recent measurements (emiT, etc [40, 41]) that claim a value for D are consistent with this zero value. If this value were non-zero, it would describe how the differential decay rate couples to the sine of the angle between the electron and neutrino, and would also contribute to the error of the Nab experiment's measurement of a.

If the angle between the spin of the neutron and the electron's momentum (θ_e), and the angle between the momenta of the electron and neutrino ($\theta_{e\nu}$) are considered independent, then the cosine of the angle between the neutron spin and the antineutrino momentum (θ_ν) can be determined via the dot product in spherical coordinates, when the neutron spin is oriented along the vertical axis (see Figure 2.5 for a diagram of these angles):

$$\cos\theta_\nu = \cos\theta_{e\nu}\cos\theta_e + \sin\theta_{e\nu}\sin\theta_e\cos\left(\phi_e - \phi_\nu\right) \tag{2.20}$$

Because the spectrometer has cylindrical symmetry, the terms with ϕ_e and ϕ_ν integrate to zero – those angles represent the projection of the electron and neutrino in the plane perpendicular to the neutron spin, and there shouldn't be a preferential direction for the decay plane to orient itself around the spin (the angle the decay plane makes with the spin, however, is a different matter). The A and B terms become:

$$\frac{\partial w}{\partial E_e \partial \Omega_e \partial \Omega_\nu} \propto |\langle \sigma_n \rangle| \left(A \beta_e \langle \cos\theta_e \rangle + B \langle \cos\theta_e \rangle \cos\theta_{e\nu} \right) \tag{2.21}$$

The A term here does not depend on $\cos\theta_{e\nu}$, and would be interpreted in the Nab experiment's data as a false b. The B term is linear in $\cos\theta_{e\nu}$- It would contribute a false addition to Nab's measurement of a, the size of which depends on the polarization and the average value of $\cos\theta_e$.

$$\Delta a = \frac{B |\langle \cos\theta_e \rangle| \langle \sigma_n \rangle|}{\beta_e} \tag{2.22}$$

To stay within the systematic error budget, the fractional change in a associated with the polarization needs to be less than 10^{-4}.

$$\frac{\Delta a}{a} = \frac{B |\langle \cos\theta_e \rangle| \langle \sigma_n \rangle|}{\beta_e a} \leq 10^{-4} \tag{2.23}$$

The value for $\langle \cos\theta_e \rangle$ is related to the minimum acceptance angle of the spectrometer and the polarization of the neutron beam. Because the spectrometer has a particular acceptance angle, and can only see protons that leave the decay with a particular momentum relative to the spectrometer axis, the angles the electron momentum can make with the field, and thus the neutron spin are also limited. Since the neutrons are polarized either along the field, or anti-parallel to it the average polarization will also contribute to the average value of this angle.

This average can be calculated using a Monte-Carlo event generator. This event generator calculates the 4-vector momenta of the proton, electron and antineutrino in their decay plane, and then uses Euler angles to rotate that decay plane into 3-dimensional space. It then uses equation

2.2 to calculate the probability of such an event occurring, and either counts this event or rejects it based on that probability. Events are also accepted or rejected based on whether or not the proton momentum would be included in the spectrometer acceptance angle. Here the spin of the neutron that decays is given an upward spin or a downward spin along the vertical z-axis (the direction of the field), using a probability based on simulated polarization of the beam. This Monte Carlo simulation can also be used to construct the teardrop plot similar to that in Figure 2.1. A more detailed description of this type of event generator can be found in appendix A.

The results for the Monte Carlo average of $\langle \cos\theta_e \rangle$ as a function of the neutron polarization ($|\langle \sigma_n \rangle|$), at the known acceptance angle of the spectrometer($\cos\theta_{p,max}$ =0.758) are shown in Figure 2.6. When these values for $\langle \cos\theta_e \rangle$ are inserted back into the expression for the error on a, using the current Particle Data Group average for $B = 0.9807 \pm 0.0030 \approx 1$, $\beta_e \approx 1$, and $a \approx 0.105$, figure 2.7 results. This shows that the upper limit on the neutron beam polarization that keeps within Nab's error budget is $\approx 2 \times 10^{-5}$, but still carries some dependence on the polarization itself.

In order to verify that the beam polarization is below this value, it will be measured with a polarized Helium-3 analyzing cell and a pair of neutron monitors. It can also be measured using the ^{3}He analyzing cell, an adiabatic fast passage (AFP) spin flipper, and a pair of neutron monitors. Chapter 3 of this work describes the design and construction of an AFP Spin Flipper to be used for this experiment, and Chapter 5 describes the methods associated with the different types of polarization measurements, as well as methods for determining the efficiency of the AFP Spin Flipper.

At present, data to verify the beam polarization have not yet been taken. If it turns out that the polarization of the neutron beam is greater than 2×10^{-5} then the Nab experiment can run in "Spin Flipper Mode," wherein the AFP Spin Flipper can be used to flip the spins of neutrons in half the neutron pulses that reach the experiment. These flips would extinguish the polarization of the beam and lower it to a more acceptable value when the data collected for the experiment is averaged across multiple pulses.

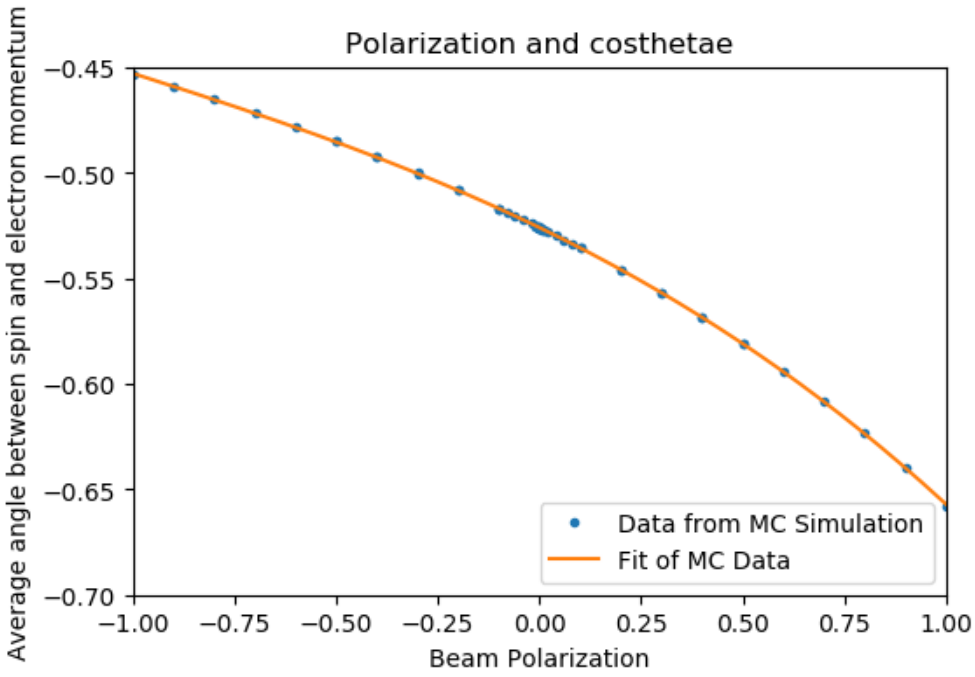

Figure 2.6: Monte Carlo Results: The average value of the cosine of the angle between the spin of the neutron and the momentum of the electron, $\cos\theta_e$, for various values of the neutron beam polarization, when the events seen by the spectrometer are restricted such that the angle between the proton momentum and the magnetic field of the spectrometer is less than 40^0

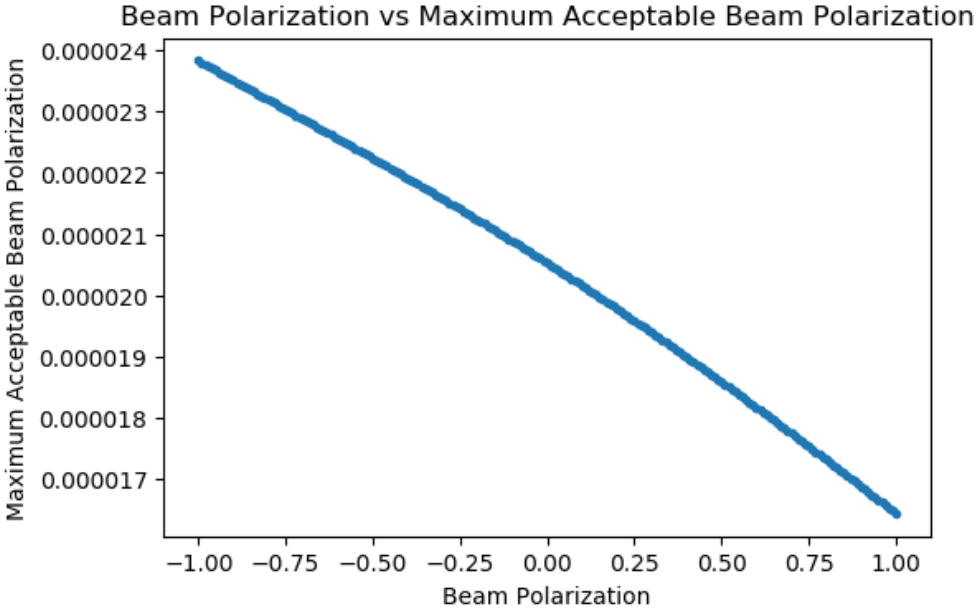

Figure 2.7: The maximum permissible neutron beam polarization permissible for beam polarizations between -1.0 and 1.0- The range of maximum permissible polarizations is between 1.6 and 2.4×10^{-5}. At those polarizations, the maximum allowed polarization is 2.05×10^{-5}

CHAPTER 3

Design and Construction of an Adiabatic Fast Passage Spin Rotator

Adiabatic Fast Passage (AFP) is a nuclear magnetic resonance (NMR) technique for flipping the magnetic moments (spins) of a population of atoms, molecules, or particles. It requires two types of fields, one static field (B_0), and a rotating field (B_1). Essentially, if the field conditions change, such that the system sweeps through resonance with the Larmor frequency of the particles, the magnetic moments of the particles can be reversed. Rather than precessing about the field, the magnetic moments will precess around a vector that is anti-parallel to the field. This chapter will describe AFP in greater detail, and then describe the design and operation of the AFP Spin Flipper built for the Nab Experiment.

3.1 Adiabatic Fast Passage and Spin Magnetic Resonance

3.1.1 Spin Magnetic Resonance from a Classical Perspective

Classically, a static magnetic field, $\vec{B}$ imposes a torque force on a particle's magnetic dipole moment, which changes the particle's angular momentum.

$$\vec{\tau} = \frac{d\vec{J}}{dt} = \vec{\mu} \times \vec{B} \tag{3.1}$$

Quantum mechanically, the component of the angular momentum of a particle related to its

spin, $\vec{J}$ is related to its intrinsic magnetic moment, $\vec{\mu}$, via it's gyro-magnetic ratio, γ. The torque force can be described in terms of that intrinsic magnetic moment.:

$$\frac{d\vec{\mu}}{dt} = \gamma\vec{\mu} \times \vec{B} \tag{3.2}$$

The time derivative of the torque equation, when the field is static yields:

$$\frac{d^2\vec{\mu}}{dt^2} = \gamma\frac{d\vec{\mu}}{dt} \times \vec{B} = \gamma^2\left(\vec{\mu} \times \vec{B}\right) \times \vec{B} \tag{3.3}$$

$$\frac{d^2\vec{\mu}}{dt^2} = -\gamma^2\left(|B|^2\vec{\mu} - \left(\vec{B} \cdot \vec{\mu}\right)\vec{B}\right) \tag{3.4}$$

The specific components of the second derivatives of μ, for a particle whose initial magnetic moment is in the x-z plane and makes an angle, θ with a field of strength B_0 aligned in the z-direction are:

$$\frac{d^2\mu_x}{dt^2} = \gamma^2 B_0^2\mu_x \tag{3.5}$$

$$\frac{d^2\mu_y}{dt^2} = \gamma^2 B_0^2\mu_y \tag{3.6}$$

$$\frac{d^2\mu_z}{dt^2} = 0 \tag{3.7}$$

The components of μ then work out to be:

$$\mu_x = \sin\theta\cos\left(\gamma B_0 t\right) \tag{3.8}$$

$$\mu_y = \sin\theta\sin\left(\gamma B_0 t\right) \tag{3.9}$$

$$\mu_z = cos\theta \tag{3.10}$$

The motion described by these equation is a precession of the magnetic moment vector about the magnetic field vector and is illustrated in Figure 3.1. This phenomenon arises because the torque (the change in angular momentum) is always perpendicular to both the angular momentum itself and the field, and is known as Larmor Precession. The frequency of this precession increases

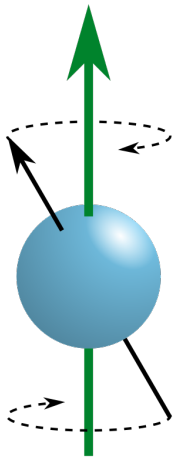

Figure 3.1: A diagram of the precession of the magnetic moment (black) around a magnetic field (green). (Image courtesy Wikimedia Commons)

with the strength of the field, and is known as the Larmor Frequency, $\omega_L = \gamma|\vec{B}|$.

To understand how this precession arises, it is also illustrative to examine the system in a frame rotating at a frequency $\vec{\omega}$, about an axis aligned with the static field[1]. In this rotating frame, the time derivative of $\vec{\mu}$ must be adapted to account for the time derivatives of the unit vectors that describe the motion of the frame. In this case, that motion contributes an additional apparent torque. This is a result of classical mechanics, known as the Transport Theorem, and is also responsible for things like the Coriolis effect [42].

$$\frac{d\vec{\mu}}{dt}_R = \frac{d\vec{\mu}}{dt} - \vec{\mu} \times \vec{\omega} \tag{3.11}$$

$$\frac{d\vec{\mu}}{dt}_R = \vec{\mu} \times \gamma \left(\vec{B} - \frac{\vec{\omega}}{\gamma} \right) \tag{3.12}$$

In this case, the torque acts in the same way that the torque caused by the field does. It acts like an additional "effective field" in this rotating frame.

[1]This is the first of many rotating frames. Switching between static and rotating reference frames too quickly may result in dizzines

$$\vec{B_{eff}} = \vec{B} - \frac{\vec{\omega}}{\gamma} \tag{3.13}$$

When the effective field cancels the real field, and $\vec{\omega} = \gamma\vec{B}$, and $|\omega| = |\omega_L|$, the magnetic moment no longer changes with time in this frame. The magnetic moment of the particle is static in this rotating reference frame but rotates at the frame's frequency, the Larmor frequency, when viewed by a static observer in the laboratory frame.

If a perpendicular field is applied that rotates in the lab frame with a magnitude B_1, at a frequency, ω_L, it would appear to be stationary in the rotating frame (it moves with the frame). At resonance, when a static field in the rest frame meets the Larmor condition, $B_0 = -\omega_L/\gamma$, the effective field experienced by the particle has the magnitude B_1 but is and is static in this frame. The magnetic moment will precess about this stationary effective field. If this resonance condition is maintained for a specific time interval, B_0 and B_1 can be used to tip the magnetic moment of our particle by a specific angle about the rotating field. If the magnetic moment is aligned with B_0 at the start of the process, then the angle, α over which the magnetic moment will tilt over a specific interval of time, t, can be expressed as [43]:

$$\cos\alpha = 1 - 2\sin^2\theta\sin^2\frac{at}{2} \tag{3.14}$$

$$a = -\gamma\left[\left(B_0 - \frac{\omega}{\gamma}\right)^2 + B_1^2\right]^{\frac{1}{2}} \tag{3.15}$$

$$\sin\theta = \frac{\gamma B_1}{a} \tag{3.16}$$

When $\alpha = \pi$, this formula describes a complete spin flip. This is also recognizable as the Rabi formula for a half-spin particle, which describes the probability of finding the particle in a rotating field in the spin-down state[43, 44]. See Section 3.1.2 for a discussion of the Rabi formula in a quantum mechanical picture.

Tipping spins in this manner is a common NMR technique and is often used in the lab to ex-

amine the nuclear magnetic signal from an ensemble of atoms and to induce Free Induction Decay signals. In practice, this technique can be used to produce a resonant spin flip in a neutron beam experiment. Spin flippers of this sort were used in the n3He and NPDGamma experiments at ORNL in static ambient magnetic fields of about 10G which were nearly uniform, to measure the polarization of a pulsed, polarized, neutron beam.[15, 45, 46]. Because neutrons move through these experiments and their fields at different speeds, individual neutrons will spend different amounts of time in the field. To produce a high-efficiency spin-flip, the magnitude and frequency of the oscillating field have to be modulated to account for the amount of time the particles spend in the field. The Nab Experiment is subject to the non-uniform fringing fields of the spectrometer, so a careful examination of what happens when B_0 changes is required. This will be carried out in the sections that follow, after a short discussion of the quantum mechanical description of Spin Magnetic Resonance.

3.1.2 Spin Magnetic Resonance and Adiabatic Fast Passage, from a Quantum Mechanical Perspective

From a quantum mechanical perspective, one can arrive at the same equations of motion for the components of the magnetic moment that result in Spin Magnetic Resonance using the Schrödinger equation[43].

$$i\hbar\frac{d\psi}{dt} = \mathbf{H}\psi \tag{3.17}$$

Here,ψ is the two-component vector representing the spin state, and the Hamiltonian, **H** is the energy associated with the spin of the particle in the field, **S** (**S** is $\hbar$ times the Pauli matrices, σ_x, σ_y, and σ_z):

$$\mathbf{H} = -\gamma\vec{B}\cdot\vec{\mathbf{S}} \tag{3.18}$$

$$\sigma_x = \begin{pmatrix} 0 & 1 \\ 1 & 0 \end{pmatrix}, \sigma_y = \begin{pmatrix} 0 & i \\ -i & 0 \end{pmatrix}, \sigma_z = \begin{pmatrix} 1 & 0 \\ 0 & -1 \end{pmatrix} \tag{3.19}$$

For a half-spin particle whose initial spin makes a small angle, θ with the z-axis, in a magnetic field chosen to be aligned with the z-axis. the solution to the Schrödinger equation describes a 2-state system with an energy separation of $\hbar\omega_L$, where ω_L is the Larmor frequency, γB.

$$\psi(t) = \begin{pmatrix} \cos\frac{\theta}{2} e^{i\gamma B_0 t/2} \\ \sin\frac{\theta}{2} e^{-i\gamma B_0 t/2} \end{pmatrix} \tag{3.20}$$

The equations of motion for the spin components, here given in the Heisenberg Picture, return the classical equations of motion[44]:

$$i\hbar\frac{d\vec{\mathbf{S}}}{dt} = -\gamma\left[\vec{\mathbf{S}}, \vec{B}\cdot\vec{\mathbf{S}}\right] \tag{3.21}$$

$$\frac{d\vec{\mathbf{S}}}{dt} = \gamma\vec{\mathbf{S}}\times\vec{B} \tag{3.22}$$

The expectation values for the components of the spin vector ($< \mathbf{S}_x >, < \mathbf{S}_y >$ and $< \mathbf{S}_z >$ demonstrates the same precession in the x-y plane at the Larmor frequency that the classical analysis does[47].

$$\langle \mathbf{S}_x \rangle = \frac{\hbar}{2}\sin\theta\cos(\gamma B_0 t) \tag{3.23}$$

$$\langle \mathbf{S}_x \rangle = \frac{\hbar}{2}\sin\theta\sin(\gamma B_0 t) \tag{3.24}$$

$$\langle \mathbf{S}_z \rangle = \frac{\hbar}{2}\cos\theta \tag{3.25}$$

If both the static and rotating fields are applied the time dependent Schrödinger equation can be expressed as follows:

$$i\frac{d\psi}{dt} = -\gamma\left(B_0\mathbf{S}_z + B_1\mathbf{S}_x\cos\omega t + B_1\mathbf{S}_y\sin\omega t\right)\psi \tag{3.26}$$

From here, the Rabi formula, equation 3.16[43], can be obtained by switching into a rotating frame, with the appropriate change-of-basis operators. When starting with a pure state, the probability of occupation for either spin state as a function of time can be obtained by integrating these formulas appropriately. [43].

The Schrödinger equation can also be expressed in terms of the raising and lowering operators, $\mathbf{S}_{\pm} = \mathbf{S}_x \pm i\mathbf{S}_y$:

$$i\frac{d\psi}{dt} = -\gamma\left(B_0\mathbf{S}_z + \frac{B_1}{2}\mathbf{S}_+e^{-i\omega t} + \frac{B_1}{2}\mathbf{S}_-e^{i\omega t}\right)\psi \tag{3.27}$$

The presence of the raising and lowering operators immediately signals that the oscillating field in this Hamiltonian couples between the up and down spin states, and promotes transitions from one state to the other.

From here, time-dependent perturbation theory can be used to derive the Rabi formula, by considering the part of the Hamiltonian associated with the rotating field to be a perturbation on the Hamiltonian associated with the particle in the static field [44]. In this case, the matrix develops off-diagonal elements related to the strength of the rotating field.

As demonstrated in the classical interpretation, the Rabi formula is applicable to the resonant case, where the magnitudes of the fields B_0 and B_1 are constant in time. If the magnitudes of the fields change, their adiabaticity must be considered.

3.1.3 Defining an Adiabatic Parameter for Adiabatic Fast Passage

By examining the fields from a rotating frame of reference, similarly to how the classical interpretation is carried out, a more precise definition of what ”slowly enough” means can be obtained. The rotating reference frame here is two-fold. The first rotation fixes B_1 along the x-axis by rotating at a frequency of ω with the field. The field experienced by the particle in this frame is the

effective field demonstrated in Section 3.1.1.

$$B_{R_1} = \vec{B_0}(t) - \frac{\omega}{\gamma}\hat{z} + B_1\hat{x} \tag{3.28}$$

A second rotation also fixes B_{R_1} on the z-axis, by rotating at a frequency of Ω inside the first rotating frame. Here. Ω is the vector that describes any change in the effective field in the first frame.

$$\vec{\Omega} = \frac{\vec{B_{R_1}} \times \frac{d\vec{B_{R_1}}}{dt}}{|B_{R_1}|^2} \tag{3.29}$$

Because first rotation fixes $\vec{B_1}$ along the x-axis, and the second frame fixes the whole effective field in the z direction, $\vec{\Omega}$ only has a y-component in the second rotating frame. The effective field experienced by the particle in this frame is:

$$\vec{B_{R_2}} = |B_{R_1}|\hat{z} - \frac{|\Omega|}{\gamma}\hat{y} \tag{3.30}$$

The equations of motion for the spin components in the Heisenberg picture become[48]:

$$\frac{\mathbf{S}_x}{\gamma} = \mathbf{S}_y|B_{R_1}| - \mathbf{S}_z\frac{|\Omega|}{\gamma} \tag{3.31}$$

$$\frac{\mathbf{S}_y}{\gamma} = -\mathbf{S}_x|B_{R_1}| \tag{3.32}$$

$$\mathbf{S}_z = \mathbf{S}_x|\Omega| \tag{3.33}$$

If $|\Omega|/\gamma$ is negligible compared to $|B_{R_1}|$, then only the pair $\mathbf{S}_x$ and $\mathbf{S}_y$ remain coupled, and the $\mathbf{S}_z$ component remains fixed. In this approximation, spin precession about $\vec{B_{R_1}}$ is preserved in this frame. As $\vec{B_0}(t) - \frac{\vec{\Omega}}{\gamma}$ changes, the spins will stay aligned with this field in the rotating frame. If B_0 is initially less than $\frac{\Omega}{\gamma}$, and increases past the Larmor frequency, the sign of this component of the field in the rotating frame will change. This is what causes a spin flip in the static lab frame. Figure 3.2 demonstrates a schematic diagram of what happens to the magnetic moment of a particle as it

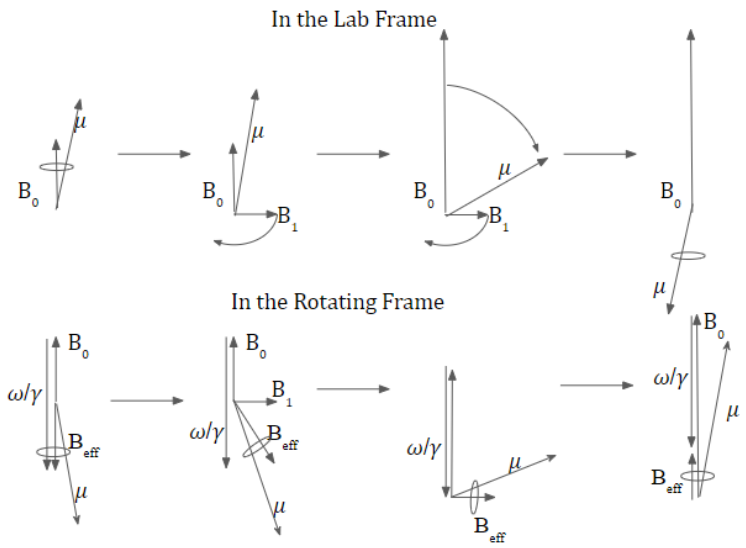

Figure 3.2: a diagram of the interactions between the fields and the magnetic moment of the particle in the lab and rotating reference frame. In the lab frame the magnetic moment, μ precesses about B_0, but flips to precess away from B_0 after the rotating field, B_1 is applied. In the rotating frame, μ precesses about the effective field, as all the fields are stationary in this picture. As B_0 increases, the relative direction between μ and B_0 changes sign in both frames.

undergoes reversal by AFP.

The condition that Ω/γ is negligible compared to $|B_{R_1}|$ can be configured into an adiabaticity parameter, a, such that Adiabatic Fast Passage can occur when $a << 1$:

$$a = \frac{|\Omega|}{\gamma |B_{R_1}|} \tag{3.34}$$

This looks suspiciously like a ratio between the change in the field, Ω, and the Larmor precession frequency associated with the magnitude of the whole field. Because Ω and B_1 are constant, and the direction of B_0 is fixed this simplifies to:

$$a = \frac{|\frac{dB_0}{dt}| \sin\theta}{\gamma B_{R_1}} \tag{3.35}$$

Here theta is the angle between the change in B_0 and B_{R_1}- $\sin\theta = \frac{B_1}{B_{R_1}}$, because B_0 is fixed along

the z-axis.

$$a = \frac{\frac{dB_0}{dt}|B_1|}{\gamma|B_{R_1}|^2} \tag{3.36}$$

This adiabatic parameter is related to the efficiency at which a field configuration will flip spins (defined here as a ratio between a final and initial projection of the spin along B_0) as follows[48]:

$$\epsilon_{SF} = \frac{1 - a^2}{1 + a^2} \tag{3.37}$$

Numerically, the specific components of the spin or the magnetic moment can be calculated by integrating equation 3.1 using an analytical expression for the fields as they change in time, or interpolated values of the field the particle experiences at each time step in the integration. This will be demonstrated in Section 3.4.

AFP can also be performed by sweeping the frequency of the oscillating field through the Larmor resonance frequency of a constant, uniform static field. This form of the technique will be applied to flip the spins of ^{3}He nuclei for polarimetry measurements in Chapter 4. It works in much the same way, however now, the frequency of the rotating frame changes, rather than the magnitude of the field.

3.2 Spin Flipper Design

In the Nab experiment, the neutrons are moving along the beamline at various speeds, and experience static fringe field from the Nab Spectrometer, which increases in magnitude as the neutrons approach the decay volume. In this case, it is easiest to apply a rotating field, B_1 with constant angular velocity, and the static field, B_0 can increase smoothly along the beamline, such that neutrons will experience an adiabatically increasing B_0 as they travel. This B_0 should be oriented vertically, as the fringing field from the Nab Spectrometer is also mostly vertical in that region, and the spin flipper will need to blend with these spectrometer fields. This leaves the horizontal plane of the

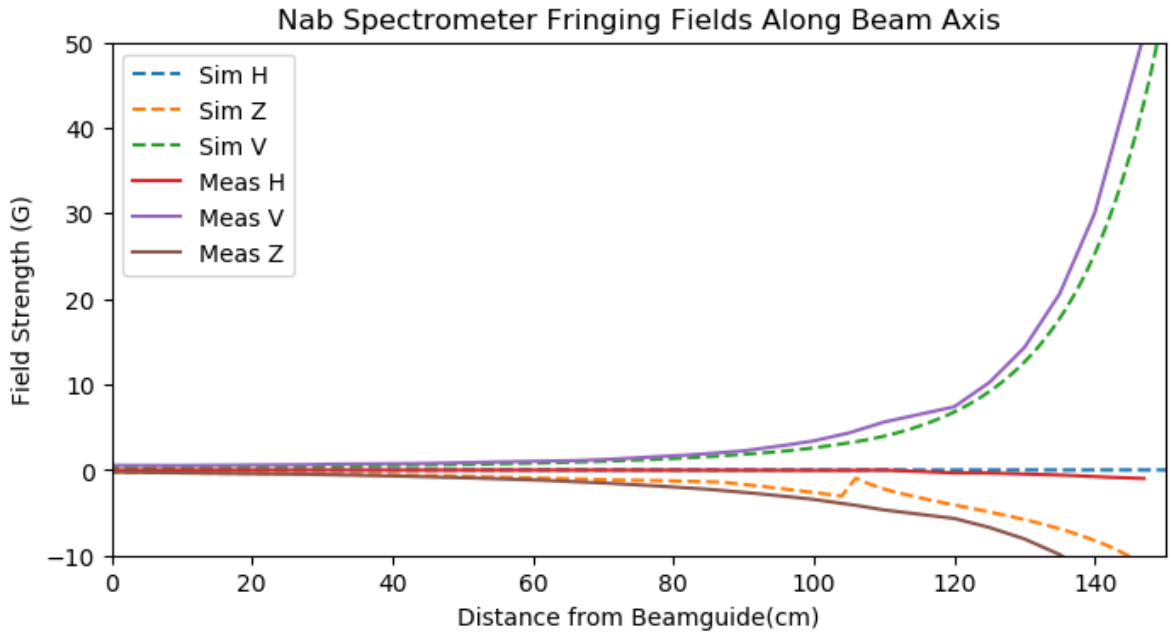

Figure 3.3: A plot of three components (horizontal, vertical and z, along the beamline) of the fringing fields of the Nab Spectrometer along the beamline, both measured (solid) and simulated (dashed) in Opera by R. Alarcon. Here kink in the fields at 110cm is associated with a change in granularity of the simulation. The field values are calculated on a much finer grid inside the passive shielding. The Spin Flipper's static coil box will be mounted such that the field it produces will be between 20-120 cm along the beamline

experiment for the rotating field.

The most straightforward thing to construct to generate B_1 is a solenoid that wraps around the beamline. When driven in an oscillating circuit, this will generate a field along the beam axis that oscillates, but that oscillation can be composed of two counter rotating fields:

$$\vec{B_1} = \frac{B_1}{2}\left(\cos\left(\omega t\right)\hat{x} + \sin\left(\omega t\right)\hat{y}\right) + \frac{B_1}{2}\left(\cos\left(\omega t\right)\hat{x} - \sin\left(\omega t\right)\hat{y}\right) \tag{3.38}$$

The field that rotates in the wrong direction is far off-resonance for the neutrons, and so its contribution to the spin flip is greatly reduced[15, 43]. This will be easy to construct, and its design and length can be determined by the space available, and the neutronics along the beamline that it must fit outside.

The design for the device that generates the static field, B_0 , however, does not have such

convenient symmetries. The field from the designed device must blend with the field from the spectrometer, so that the neutron spins are transported adiabatically through the experiment. There are also significant constraints associated with the size of the device, and how it fits with the assembly of the experiment.

Mechanically, the spin flipper device must separate in half, such that the bottom half could be put in place, the other beamline neutronics could be installed inside the spin flipper, and then the top of the device could be applied to close everything up. It would also be beneficial if all the neutronics inside the box could be rigidly mounted, such that leveling the spin flipper, once its installed, could help align the vacuum system between the beam guide and the spectrometer.

All of these different design constraints can be incorporated by employing the use of the Magneto-static scalar potential. According to Maxwell's equations, particularly Ampere's Law:

$$\vec{\nabla} \times \vec{B} = \vec{I} \tag{3.39}$$

In a region where no current is flowing, the curl of the magnetic field is zero. This is true of the region inside the spin flipper-Neutrons would scatter and interact with the wires that would run across the beam cross section. Since the field is curl-free in this region, it can be described as the gradient of a scalar field:

$$\vec{B} = -\vec{\nabla}\phi \tag{3.40}$$

Maxwell's equations also dictate that the divergence of $\vec{B}$ is zero, which implies that the Laplacian of ϕ is also zero:

$$\vec{\nabla} \cdot \vec{B} = \nabla^2\phi = 0 \tag{3.41}$$

Because the curl of $\vec{B}$ is a current, on the surface of the current-free volume, the following boundary conditions can be defined for the field on either side of the boundary and $\hat{n}$ is the normal

surface vector:

$$\left(\vec{B_2} - \vec{B_1}\right) \cdot \hat{n} = 0 \tag{3.42}$$

$$\left(\vec{B_2} - \vec{B_1}\right) \times \hat{n} = \vec{I} \tag{3.43}$$

These boundary conditions dictate that the components of the field that are perpendicular to the surface are continuous across the boundary, but the components that lie in the field parallel to the plane change in relation to a surface current. These conditions can also be expressed in relation to ψ:

$$-\nabla\left(\phi_2 - \phi_1\right) \cdot \hat{n} = 0 \tag{3.44}$$

$$-\nabla\left(\phi_2 - \phi_1\right) \times \hat{n} = \vec{I} \tag{3.45}$$

This implies that equipotential lines in ϕ on the surface of static field region, at specific intervals of $\Delta\phi$ represent the current that can be applied on this surface to generate the desired flux conditions on that surface and on the inside of the region. By solving Laplace's equation with the desired flux on the surface of the static field's volume, a Finite-Element solver can construct ϕ. A contour map of ϕ on the surface of the volume can be used as a map for the wire paths to construct the field. Just like an electric potential, the specific values of ϕ are immaterial- they can change with a choice of gauge, however the difference between the values of ψ are important.

For the Nab Spin Flipper, the size of the static field generator was determined by the diameter of the internal neutronics beampipe, and the diameter of the acrylic tube that fits outside of all of that for winding the RF coil. Because machining on a curved surface is difficult, and requires special equipment to perform, it was determined that the static field generator should be a box with a square cross-section, 12in on each side, that was 1.4m long. This geometry was constructed in Comsol^{TM}, a multiphysics software that can perform finite element analysis to solve Laplace's equations.

The boundary conditions in this simulation included an outward flux that increased linearly with the x-coordinate across the top of the box, and an inward flux that matched it along the bottom of the box. Because the field is intended to be vertical, the left and right sides of the box should have zero net flux. The remaining two faces of the static coil volume were given constraints that imposed that they both had zero flux, and that ϕ was zero on these faces. This constraint forbids the equipotential lines, and thus the wire paths of interest, from crossing the beam and scattering neutrons. The most important result from this finite element analysis is a plot of ϕ on the surface of the static coil box.

The particular values of the potential generated in Comsol^{TM} are not of particular importance, because the peak field strength, and thus the rate of change in the field along the beamline, can be controlled by adjusting the current applied to wires. The contours were chosen such that each one is separated by the same $\delta\phi$, so each loop in the figure should run on the same current, and the number of included contours was chosen based on the distance between the coils where they are most tightly packed-the minimum distance between two loops of wire couldn't be smaller than the diameter of the wire that would be chosen for winding the coil. A convenient symmetry between the top and bottom of the box also meant that, by choosing to incorporate an even number of contours, contours were prevented from crossing between the top and bottom of the box. This makes the top and bottom halves of the box separable, as was desired in this design. Figure 3.4 shows an image of the coil pattern that is generated from the Comsol^{TM} data.

Points from the contour plot can be exported, sorted, and imported into a different software, BiotSavart^{TM}, to simulate the field generated by these contours as wires. BiotSavart^{TM} is a piece of software that performs a numerical integration along simulated current-carrying paths, to calculate the magnetic field at particular probe points around the current-carrying configuration. The field along the central beam axis is plotted in Figure 3.5. This field demonstrates the desired increase along the box.

The values of the field along the axis can also be compared to values of the field off axis. While the vertical component of the field is fairly stable both on and off axis, the transverse components of

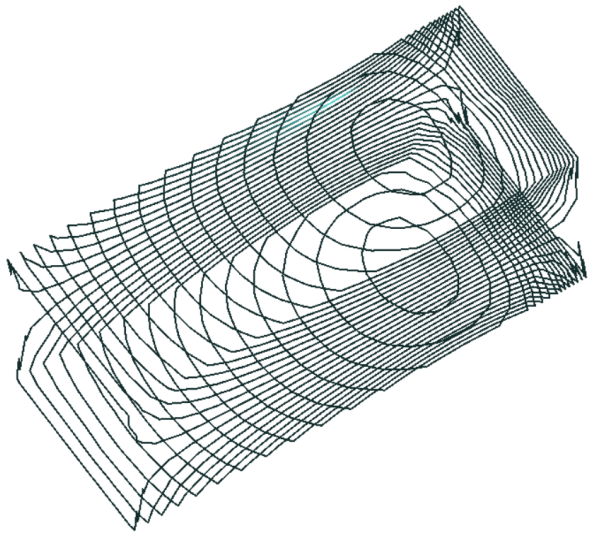

Figure 3.4: The coil pattern for the static coil of the spin flipper, rendered in BiotSavart ^{TM}

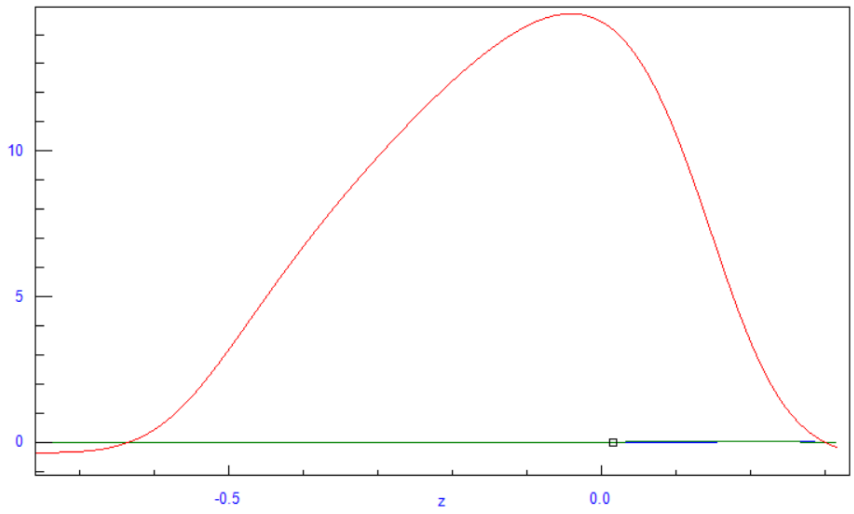

Figure 3.5: a plot of the simulated field along the central beam axis, generated by the wire patterns using BiotSavart ^{TM}. Here, z is in meters, and the z=0 is at the peak of the field, in the center of the smallest loop of the wire pattern.

the field to change across the box. These non-uniformities are a bi-product of Maxwell's equations, but are not sufficiently larger than the non-uniformities associated with the fringing field from the spectrometer, which has an entirely different symmetry. These field uniformities may cause some Stern-Gerlach steering, and bend the trajectory of the neutrons slightly, but the collimation here is also quite tight, so this is not expected to be a large effect on the counts received by the neutron monitors.

This coil shape design makes sense. One of the most basic types of magnetic fields is a simple dipole field, generated by a loop of wire. This design is effectively taking several dipoles, stacking them inside each other, and then shifting their centers to produce the desired linear increase. The peak of the field forms at the center of that central loop of wire, the steep drop-off occurs where the wires are all bunched up together, and along the top surface of the box, the wires are nearly equidistant where the field is increasing. The curved patterns along the side of the box

The Spin flipper was originally designed to achieve 30G at its peak, but over the course of its design, that has been reduced by quite a bit, because of its proximity to the spectrometer magnet. The original power required was quite substantial, and would have caused the device to get quite hot, especially in regions where the wires that generate the field are packed closely together. As such, a water cooling system was added, which circulates room temperature water through 6 channels of copper pipes, that are epoxied to the inside walls of the gradient coil with a heat-conducting epoxy. Water from a pump is pumped through a manifold, and split into the 6 channels with flexible plastic tubing. At the upstream edge of the Static Coil box, the plastic tubing is converted to copper, which runs along the inside of the box, ending back at the upstream edge of the box, where they are converted back to plastic, passed through analogue flow gauges- mounted on the side of the beam guide. Then they are merged back into one channel, and the water is recirculated through the pump.

The original design drawings, along with notes on updates made to the design years later are available on the Nab wiki archive

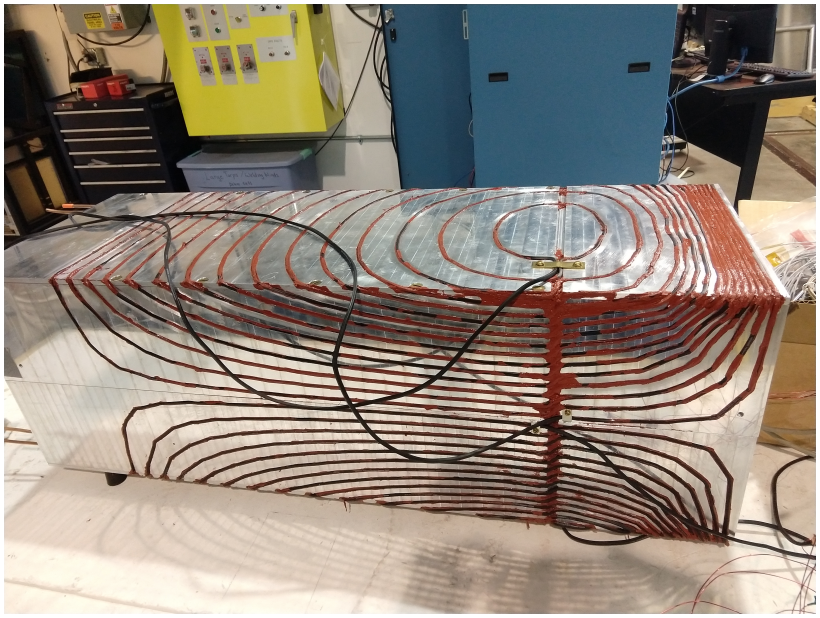

Figure 3.6: A photograph of the completed Static Coil in 2017, before the coil was later shortened in 2019 by cutting a few inches of the left end.

3.3 Spin Flipper Construction

3.3.1 Static Coil Construction

Grooves for the wires that map to the equipotential lines described in 3.2 were machined into half-inch aluminum plates. These grooves were constructed to fit #12 AWG speaker wire, which was glued into the grooves with room-temperature vulcanizing silicone adhesive. Each of the loops are wound in series, such that the leads that connect to the power supply and the leads that connect one loop to the next overlap each other. The space between the loops is too close to twist the incoming and outgoing wires, but they are run together to prevent them from contributing to the magnetic field.

Grooves were also milled on the inside of the box panels so that copper tubing for the water cooling system could be bent and then epoxied into place with a thermally conductive, aluminum loaded epoxy (70-3812NC Hi Thermal Transfer Epoxy from Epoxies Etc). These cooling lines are more dense in regions towards the downstream end of the box, where the current density is highest, and the box is more likely to get warm while operating.

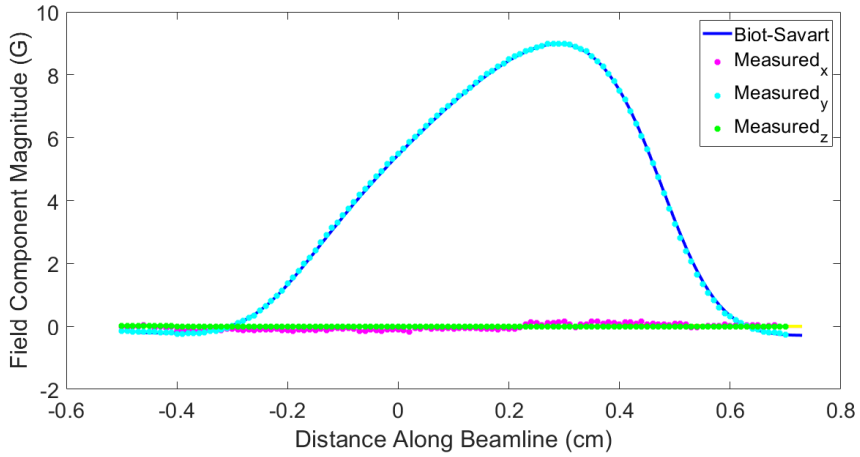

Figure 3.7: a comparison of a map of the field from the Static Coil, collected via a Bartington Fluxgate, and data from the computed model

After construction and assembly, the fields generated by the Static Coil were mapped, and compared to the model constructed in BiotSavart^{TM}. Figure 3.7 shows the on-axis data, compared to a scaled map from the mode. Figure 3.8 shows a data collected from across the cross section of the Static Coil at various points along its length. Figure 3.9 shows the projection of the field along the vertical axis (the vertical component of the field, divided by the field magnitude). This shows that the field is predominately vertical inside the spin flipper box, across the beam cross section.

The Static Coil is powered by a Kepco ATE 15/50 power supply. This supply is capable of applying 50A of current at 15V, at peak operating power, and was chosen for its low noise output. The resistance of the spin flipper coil itself is about half an ohm, neglecting any of the wires that connect the spin flipper to the power supply at the point where the leads exit the experiment's radiological shielding. The cable that connects the Static Coil to the power supply may contribute a significant resistance, and place a limit on how much power the Static Coil can use. The fluxgates used to measure the field can only measure fields less than 10G, so the mapping here was performed at reduced power. It will no longer be possible to measure the field inside the Static Coil once it is mounted on the beamline, so the proportionality constant between the field at the peak, and the applied current had to be measured. This data is displayed in figure 3.10. It serves as a way to judge the field created by the Static Coil, once it is mounted and encased in the lead shielding.

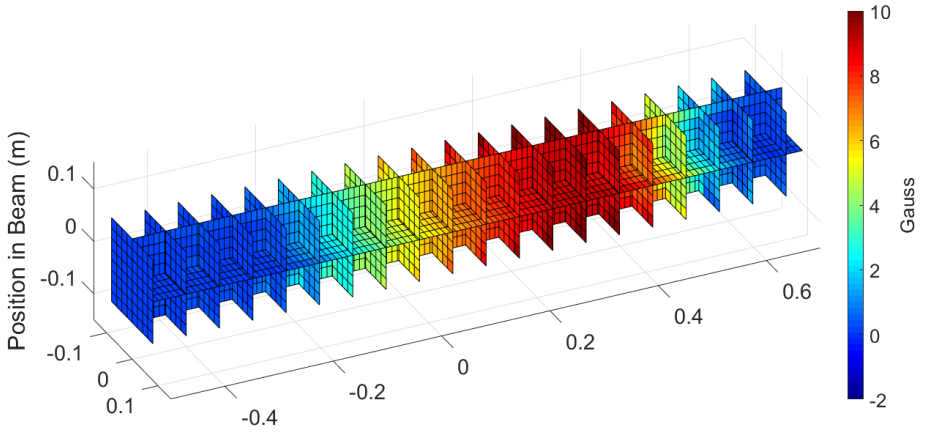

Figure 3.8: A map of the field magnitude from the Static Coil in several planes transverse to the beam axis. The peak of the field is at 0.3m along the axis

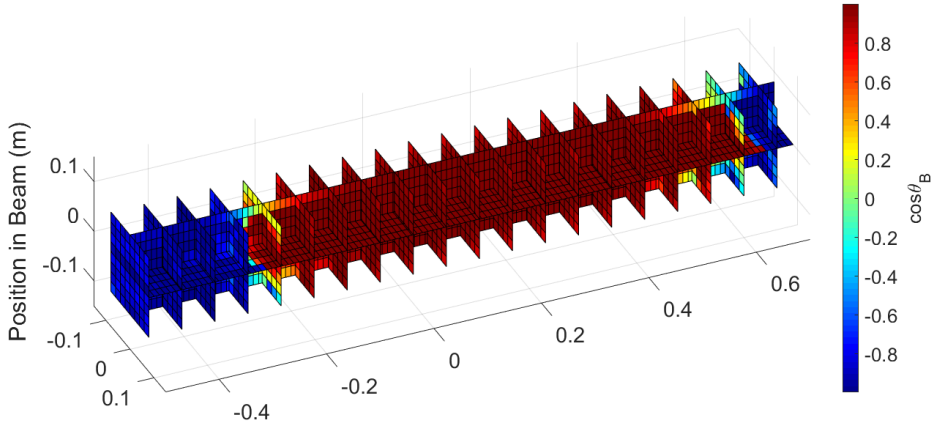

Figure 3.9: A map of the vertical projection of the field (the vertical component of the field, divided by the field magnitude), in the same transverse planes along the beamline as pictured in Figure 3.8. This shows that the projection of the field is mostly vertical, until the neutrons are exiting the field guide box, where the magnitude of the field drops of significantly, and bows out like one would expect of a dipole.

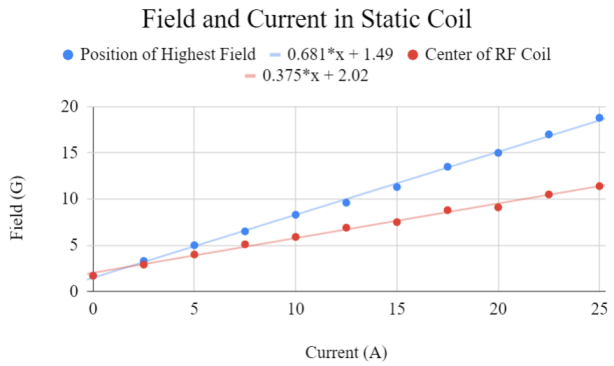

Figure 3.10: The field measured at two different points along the inner axis of the static coil (the peak of the field and the center of the RF coil mount) for different currents. This is a calibration of how the field changes with the current so that the current can be used to control the field without directly measuring the field inside the coil itself.

When the measured field from the spectrometer and the measured field from the Spin Flipper are added together, the resulting field along the beam axis has a dip. In order to accommodate some of the vacuum system, the Spin Flipper had to be moved upstream at some point in the design process, which means that its sitting at a lower point in the fringing fields. This dip in the field is below 13G, the intended resonance for the RF coil. This could cause spins to re-flip as they exit the Spin flipper. To solve this problem, an additional pair of vertical coils were constructed that can be used to pad out this field. They are approximately 1in thick, 90cm wide, and 50cm long. When 5A are applied, they produce a 10G vertical field. This provides just enough of an extension that the field says above the resonance point while the neutrons travel toward the decay volume. Figure 3.11 shows a comparison between the fields with compensation and without.

A second vertical coil pair was also constructed to pad the field upstream of the Spin Flipper. This extra set of coils can help control the fields in this region, and make sure that the field the neutrons experience is mostly vertical, and does not cross zero right before the neutrons enter the Spin Flipper. This additional field was useful in some simulations (see 3.4), however, there is no way to control the fields further upstream in the neutron guide. A field zero may be inevitable, and moving it further upstream using an additional coil set is arbitrary. This coil may also disturb the gradients of the holding fields used to prolong the ^{3}He polarization lifetime when the polarizer is

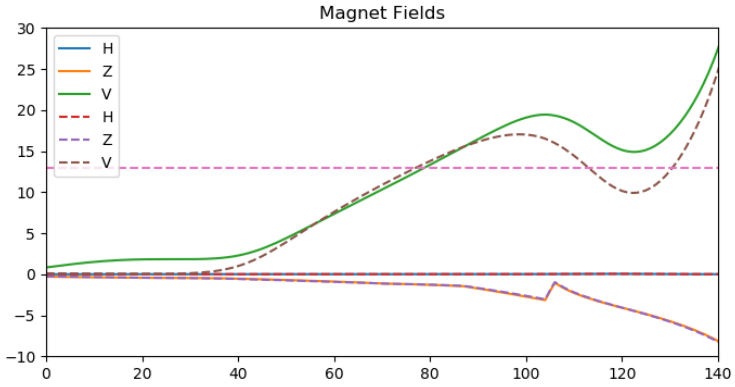

Figure 3.11: a comparison of the net field from the Spin Flipper and the Nab Spectrometer, with (solid) and without (dashed) compensation. The dashed horizontal line is at 13G, where it is intended the neutron spins will flip. If the field dips below 13G while still in the fringes of the RF field it may cause some spins to flip a second time.

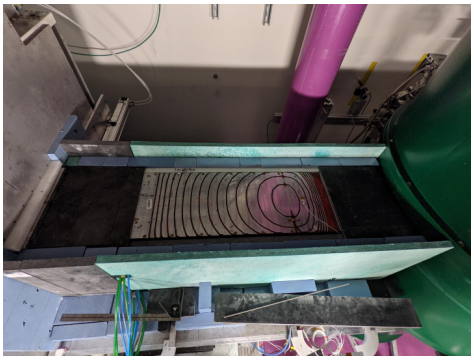

Figure 3.12: A photograph of the Static Coil installed on the FNPB at ORNL.

in use. More study of the background fields in this region would be useful, before deciding the proper operating procedure for this coil pair.

The Static Coil box was moved to Oak Ridge in 2017 and mounted on the beamline in 2021. In the summer of 2019, the box and some of its internal components were shortened, to better accommodate the ^{3}He holding field structures that polarize the beam, discussed in Chapter 4. Figure 3.12 shows the Static Coil mounted in place on the FNPB, along with its compensation coils.

3.3.2 RF Coil Construction

The RF Coil is a 9in OD acrylic cylinder wound with #18AWG wire in 3 sections, all exactly next to each other. These sections were intended to allow the center of the RF coil and its length to be slightly adjustable. The RF Coil is attached to a cradle, which is then attached to the Static Coil box. A G-10 tube gets inserted into the RF Coil tube. This G-10 tube contains the first few collimators for the experiment and serves as the beginning of the evacuated part of the beamline.

The two smaller sections on each end of the RF Coil are 10cm long. The "Upstream" section has 131 turns, and the "Downstream" section has 125 turns. After the system was shortened, these sections may have been placed on the beamline in the opposite order- It is difficult to distinguish between these sections with resistance measurements. The center section has 499 turns and is 40cm long. They are meant to be centered under the center of the inclining section of the field gradient and based on previous simulations, this works best using only the center and downstream most sections of the coil. The upstream section of the coil should be left disconnected, with its leads spaced apart so that it has too high of a resistance to produce a meaningful current when the adjacent coils are operating. The other two sections should be connected in series such that they experience a unified current.

The RF Coil is powered by a function generator and a Krohn-Hite Model No. 7500 amplifier. This amplifier can output 75W, and 625mA rms, dc to 100kHz[49]. The inductance of each section of the coil was measured, by putting that coil section in a series circuit with a 3.6nF capacitor (20% tolerance) to measure its inductance using a resonance sweep. The results of this measurement, as well as the other properties of the various RF Coil segments are summarized in Table 3.1.

Property	**Upstream Coil**	**Center Coil**	**Downstream Coil**
L(H)	0.00219 ± 0.00044	0.0125 ± 0.0025	0.00234 ± 0.00047
R(Ω)	3.6	11	3.6
Turns	125	499	131
Resonance Frequency with 3.6pF capacitor	56.7kHz	23.7kHz	54.9kHz

Table 3.1: A table outlining the properties of each RF Coil Segment

Based on these measurements, the inductance of the Center and Downstream sections put together is 0.0147+-0.0088H. The large uncertainty here is largely due to the tolerance on the capacitor. It was difficult to get a more precise measurement than the information printed on the side of the capacitor described. The long solenoid approximation, $L = \mu_0 N^2 A/l$, is not valid here. The radius is nearly on the order of the length for most of these coils. The aluminum plates that make up the Static Coil box also contribute to the inductance here, because they are meant to shield out the RF coil, and prevent RF noise from leaking into other electronics in the experiment.

The RF coil circuit is designed to be a simple LCR Circuit, that resonates at the Larmor Precession Frequency of neutrons in a 13G field (13G is roughly the midpoint of the incline where the field increases in the gradient coil, and larger than the 10G holding field necessary to maintain the polarization of the 3He upstream). That frequency is ≈ 38kHz.

3.4 Simulating the AFP Spin Flipper

Testing the Spin Flipper to assure that it performs as intended requires neutrons, which are hard to come by in the early phases of the experiment. Instead, simulated neutron spin transport through the fields of the experiment can be used to estimate the Spin Flipper efficiency, and better understand how the magnetic fields in the experiment interact with the neutrons.

To simulate spin transport, an adaptable step-size Runge-Kutta method is used to solve the differential equation:

$$\frac{d\vec{\mu}}{dt} = \gamma\vec{\mu} \times \vec{B(t)} \tag{3.46}$$

Here $\vec{B(t)}$ is the field that the neutron experiences as it travels. This simulation calculates the neutron's position in the field at each time step, and at the internal steps of the Runge-Kutta, based on an assigned initial wavelength (velocity). It uses this position and a map of the fields in the experiment to interpolate the field that the neutron experiences, and then calculates the new components of the unit vector that describes the magnetic moment.

3.4.1 Runge-Kutta Methods for Integrating Spin Tracking

The Runge-Kutta method is an extension of the Euler method for numerically solving a differential equation by linear extrapolation. These iterative methods extrapolate successive values of a function using the differential equation to generate the slope at the midpoint of the interval between a known point and the new point. Instead of taking one large step between a known and unknown value of a function, the Runge-Kutta method makes several smaller extrapolations and combines them, to produce a more accurate result. That is to say, if given a differential equation, and an initial condition[50]:

$$\frac{dy}{dt} = f(y,t) \tag{3.47}$$

$$y(t_0) = y_0 \tag{3.48}$$

then other values, y_n, can be calculated using the following prescription

$$y_{n+1} = y_n + h\sum_{i=1}^{s} b_i k_i \tag{3.49}$$

$$k_i = f\left(t_n + hc_n, y_n + h\sum_{j=1}^{i-1} a_{ij}k_j\right) \tag{3.50}$$

Here s is the order of the Runge Kutta, which describes how the step size, h, is related to the truncation ($\mathcal{O}\left(h^{s+1}\right)$) and accumulated ($\mathcal{O}\left(H^{s}\right)$) error of and the coefficients a_{ij}, b_n, and c_n are derived by equating orders of the Taylor expansion of the function, with derivatives of the differential equation[51]. These coefficients are often given by a Butcher tableau. (See Table 3.2.)

The most commonly used Runge-Kutta method is the 4th-order method, with the tableau denoted in Table 3.3. This type of Runge-Kutta is not the most accurate, most sophisticated, or most computationally efficient method for solving ordinary differential equations, but it is incredibly well understood, and easy to implement and customize. The accuracy of this method depends

0					
c_2	a_{21}				
c_3	a_{31}	a_{32}			
$\vdots$	$\vdots$		$\ddots$		
c_s	a_{s1}	a_{s2}	$\dots$	$a_{s,s-1}$	
	b_1	b_2	$\dots$	b_{s-1}	b_s

Table 3.2: The general form of a Butcher Tableau

0				
1/2	1/2			
1/2	0	1/2		
1	0	0	1	
	1/6	1/3	1/3	1/6

Table 3.3: The Butcher Tableau for a 4th Order Runge-Kutta[50]

strongly on the step size used to compute the values of the function. A smaller step size will always be more accurate, because it can calculate closer to a continuum limit. The continuum limit, however, is not practically realizable- if the step size moves towards zero, the integration trends towards taking an infinite time to complete. Instead, the step size must be tweaked to balance accuracy and computation time. To achieve good accuracy, the step size can be chosen in relation to the scales over the function is known to change. In the case of spin tracking, this means that the step size has to be able to accommodate enough points to accurately map the precession- The step size has to be about an order of magnitude smaller than the period of Larmor Precession.

The Larmor Precession frequency changes with the field, here. In the immediate vicinity of the Spin Flipper, the field varies between 0G-50G. The step size here could be chosen as a constant, and left to run through the desired region, without much loss in efficiency. Along the entirety of the beamline, however, the field increases to approximately 2T- that's 4 orders of magnitude higher, requiring a significantly smaller step size. In this case, many steps are "wasted" in low field regions where the simulation could progress much more quickly, in order to achieve accuracy when the spins are moving much more quickly and require a smaller step size. In this case, it is desirable that the step size in the Runge-Kutta method be adaptable, so that it can step carefully

through regions where the field is high, and the spins change rapidly, and it can spend less time dwelling in regions of low field, where the motion is a bit more relaxed.

Because the error associated with a Runge-Kutta is one of truncation, the difference between a 4th and 5th order solutions can be taken as an estimate of the error associated with a time step. This error can then be used to correct the step size of the simulation to achieve the desired adaptability. If the difference between the 4th and 5th order solution is too high, the step size can be made smaller using the size of the error compared to some threshold as a guide, and if the accuracy is very good, the step size can be made larger up to some bound to save on computational time[50].

For this simulation, a Cash-Karp 4th/5th order embedded Runge-Kutta was used. See Table 3.4 for the tableau for this method relies on. Here the a and c coefficients are the same at both orders, but b_5 denotes coefficients that pertain to the 5th order calculation[50, 52].

0						
1/5	1/5					
3/10	3/40	9/40				
3/5	3/10	-9/10	6/5			
1	-11/54	5/2	-70/27	35/27		
7/8	1631/55296	175/512	575/13824	44275/110592	253/4096	
b_4	2825/27648	0	18575/48384	13525/55296	277/14336	1/4
b_5	37/378	0	250/621	125/594	0	512/1771

Table 3.4: The Butcher Tableau for an embedded 4th/5th Order Cash-Karp Runge-Kutta. Here b_4 yields 4th order solutions, and b_5 yields 5th order solutions.[50]

The scheme used to adapt the step size in this method compares the difference between the 4th and 5th order solutions in the Runge-Kutta for each component of $\vec{\mu}$, and compares the maximum value of that set, e to a maximum error (e_{max}) of 1×10^{10}. If the error is larger than the threshold, the current step size is subtracted from the current total time. If the error is smaller, the data from the step is logged. In both cases the step size, h is adjusted:

$$h' = h \left(\frac{e_{max}}{e} \right)^a b \tag{3.51}$$

Here, a and b are fractional parameters that help balance the shrink in step size a bit further. It

helps to stabilize the change, such that the step size changes smoothly, rather than crashing and recovering. In most cases chosen values a=0.2, and b=0.4 strike the balance between speed and accuracy quite nicely.

Lastly, the resulting step size is compared to the Larmor Frequency, and if it is larger than $1/(100 * \gamma_n|\vec{B}|)$, it gets reset to this value, so that the simulation continues to map each precession of the neutron with sufficient accuracy, and isn't stepping over precessions when the step size gets increased.

3.4.2 Interpolating Magnetic Field Data for Simulation

The other very central piece associated with simulating the Spin Flipper, is calculating the magnetic field at all the internal points of the simulation. These fields are generated by real devices, and for the most part, lack an analytical expression that can be easily evaluated at any point in space. What can be produced more readily, however, are simulations of the fields generated by finite element analyses of the currents and materials associated with the beamline and the spectrometer. Ideally, volumetric data could be used to simulate how the full cross-section of the beam would experience the fields, and determine how well the Spin Flipper works over that area.

Fields from the smaller devices along the beam line- the Static Coil, RF Coil, and the 3He holding field coils (see section 4.3) were simulated in BiotSavart^{TM}, which can produce data on a volumetric centimeter grid. These devices were incorporated into a single model, so that they all have the correct positions relative to each other, and can be simulated as one data set.

The magnetic field from the Nab Spectrometer was simulated using Opera^{TM}, a finite element analysis suite for modeling electromagnetic fields. Here, information from the Cryogenics design models associated with the superconducting currents and the passive shielding are imported from Computer-Assisted Design (CAD) models, and then the field is calculated on a volumetric centimeter grid. In order to simulate the motion of the charged daughter particles, the field inside the spectrometer is simulated on a very fine mesh. Outside the spectrometer, along the beamline, that mesh is significantly coarser. Where the two regions meet, there is a mis-match in the field data,

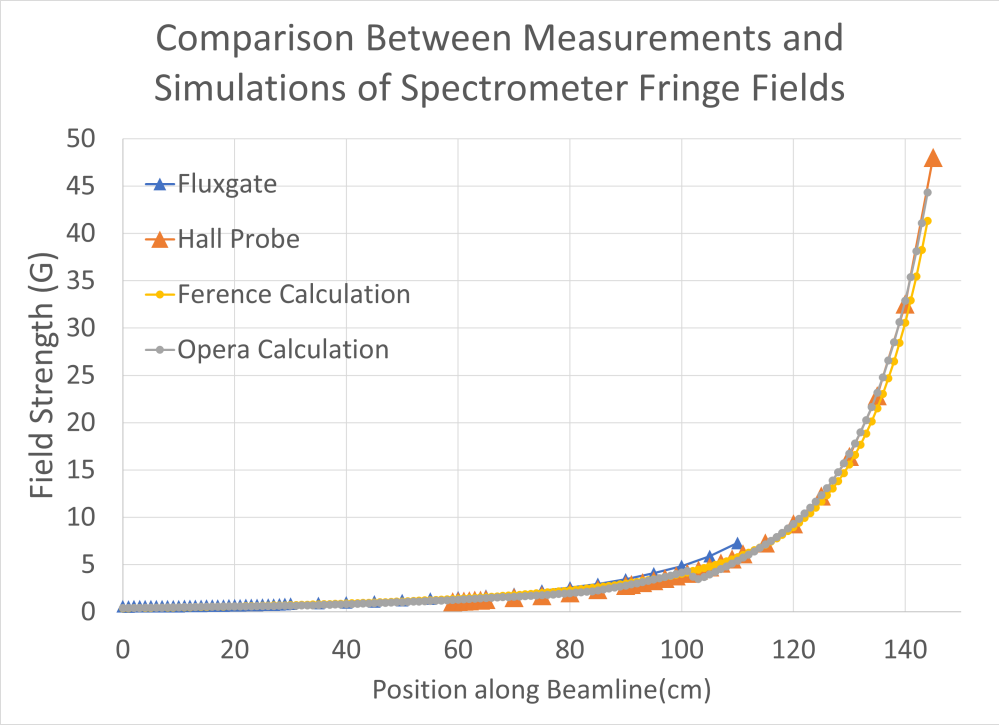

Figure 3.13: A comparison of measured and simulated data of the magnetic field generated by the Nab Spectrometer along the beamline, note the presence of the kink in the field at 105cm along the beamline.

that results in what looks like a kink in the field (see Figure 3.3). This field kink is not present in measurements of the field, and is definitely a spot where the field changes too quickly for adiabatic spin transport. This data is difficult to use in spin transport simulations.

Instead, the field from the spectrometer was measured via a fluxgate magnetometer and a hall probe, in 1cm increments along the center the beamline. The fluxgate was used where the field was below 10G, and the hall probe had to be used for higher fields. Figure 3.13 shows a comparison between each of these data sets. The measured data also encapsulates the ambient background fields in the experiment hall that the simulated data neglects. Using this measured data restricts these simulations to the axis of the beam, but it still yields a good sense of what's happening to the neutron spins as they travel.

When a spin transport simulation is performed, the step sizes required for accuracy in the Runge-kutta is smaller than this 1cm grid sizing. In the 30-50G range, the time steps are on

the order of $0.5 - 5 \times 10^{-7}$sec, and the neutrons move at speeds of about $1,000$ m/s. This leads to a spatial step size of about $1mm - 50\mu m$. In this case, a cubic spline interpolator is used to calculate off-grid field values.

A cubic spline interpolator uses the tabulated values of the field to construct estimates of the field values by enforcing that the interpolating function has a smooth first derivative, and a continuous second derivative. The interpolation at point y takes the form[50]:

$$y = Ay_j + By_{j+1} + Cy''_j + Dy''_{j+1} \tag{3.52}$$

Where the coefficients are related to the point of interpolation x:

$$A = \frac{x_{j+1} - x}{x_{j+1} - x_j} \tag{3.53}$$

$$B = \frac{x - x_j}{x_{j+1} - x_j} \tag{3.54}$$

$$C = \frac{1}{6}\left(A^3 - A\right)\left(x_{j+1} - x_j\right)^2 \tag{3.55}$$

$$D = \frac{1}{6}\left(B^3 - B\right)\left(x_{j+1} - x_j\right)^2 \tag{3.56}$$

A table of data for each component of the field ($B_x(x,y,z), B_y(x,y,z)$ and $B_z(x,y,z)$) is imported into the simulation, and sorted such that the indices of the grid points can easily be related to their position in space. This saves on computational time to look up the values for the grid points of nearest neighbors. Once the spline is in hand, it can easily be used to interpolate linear magnetic field data (data measured along the axis of the beam) by straightforwardly calculating the coefficients in 3.52.

Tables of the second derivative splines (y''_j) at each point are calculated examining the continuity of the first and second derivatives of the interpolating function (3.52) at each grid point, from each side, and matching them. The derivatives at the end points of the spline are set to zero- known as natural boundary conditions. Once those splines are in hand, the coefficients in the interpolating function can be calculated.

For volumetric data, the initial spline is calculated along the z direction for each x and y position in the table. These splines are used to calculate interpolated values along one axis at the point of interest. Those values are then used to construct a spline along a perpendicular axis at the point of interest, and a set of interpolated values is generate along that axis. Those interpolated values are then used to construct a final spline along the remaining axis, and the value of interest is interpolated from that spline.

This method of interpolation is incredibly common, however, it does not necessarily preserve the relationships associated with Maxwell's Equations- particularly because B_x, B_y, and B_z are calculated from independent tables. The results here are not necessarily divergence-free. This is known to affect the adiabaticity of the magnetic moment in calculations for particle tracking and can cause the length of the vector associated with the spin to drift[53, 54].

This is not a major concern in this case, as the grid size of the sampled points are much smaller than the size of the field sources, and the fields are expected to change slowly in these regions in order to transport the neutrons. This should be sufficient to constrain the interpolated values to within an acceptable margin of error to the data points, and the fields themselves- which do obey Maxwell's equations.

The adiabaticity can also be artificially constrained. If the magnetic moment, $\vec{\mu}$, is modeled as a unit-vector, its magnitude can be checked at the end of each step and the simulation can be stopped if it seems that the length of this vector is not preserved to within some accuracy limit. For the simulations shown in the results that follow in Section 3.4.3, the change in the length of $\vec{\mu}$ was required to be less than 1×10^{-5}.

It's worthwhile here to also note that there is quite a bit of unavoidable imprecision in what is known about the magnetic fields. The fields that are simulated are all simulated in different relative coordinate systems and have to be aligned the way they're spatially assembled in real life. The probes used for measuring field data can only be placed to within about half a millimeter of accuracy, and can also be tilted by a couple of degrees when measurements are taken. This means that, even if better interpolation methods were used, here, they would be incredibly more

computationally expensive, but they wouldn't necessarily yield more precise information on what the spins in the experiment are doing. These simulations are, instead, a very useful diagnostic tool to assess design issues in the design and structure of the fields, and find places where compensation and closer analysis may be necessary. The definitive test of how well the Spin Flipper performs will be a measurement of its efficiency using the neutron beam and polarized ^{3}He , as described in Section 5.5

3.4.3 Results of Simulations

At each time step, the Spin Transport simulator outputs the position, the components of the field, B_x, B_y, and B_z, the components of the unit vector describing the magnetic moment of the neutron, μ_x, μ_y, and μ_z, and the cosine of the angle between the field and the moment, $\cos\theta_{SB}$. This parameter ranges from -1, indicating the spins are anti-parallel to the field, to +1, indicating that the spins are aligned with the field.

A quick test of the simulation demonstrates that in a 1G field in the $\hat{z}$ direction, and for an arbitrary alignment, the simulated magnetic moment precesses about the field as expected. Figure 3.14 shows the components of the magnetic moment vector as they precess in this field. $\cos\theta_{SB}$ remains constant throughout the process, as does the component of the magnetic moment that is aligned with the field. The other two components demonstrate rotation in the x-y plane.

In order for polarimetry to work more broadly, the neutron spins must be transported adiabatically through the entirety of the beamline, to the neutron monitor located downstream of the Spectrometer. Magnetometry was not performed along the beamline, so the data from the Opera simulation must be used here. Figure 3.15 shows the alignment of the spins as they pass along the beamline and approach the center of the field. In this simulation, the neutrons are transported in excellent alignment with the field, until they approach the non-physical artifact in the simulated field data. After this point they precess about the field quite steadily- that is to say $\cos\theta_{SB}$ remains the same as the magnitude of the field changes inside the spectrometer shielding. If the simulation is started in alignment after that point (where the position is greater than 1.5m), then the spin

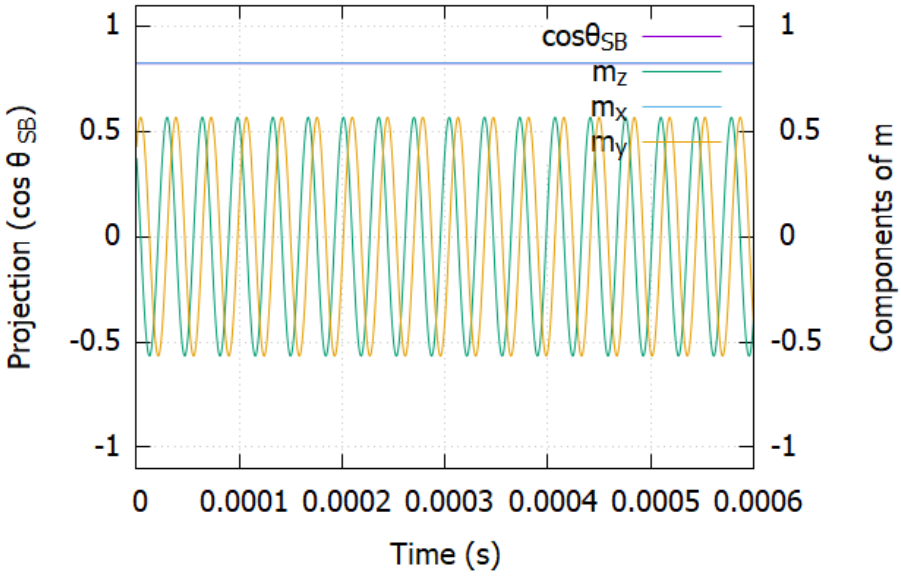

Figure 3.14: Simulated components of the magnetic moment vector precessing about a 1G vertical field. $\cos\theta_{SB}$ (purple) remains constant throughout the process, as does the component of the magnetic moment that is aligned with the field, (blue). The other two components demonstrate rotation in the x-y plane (yellow and green).

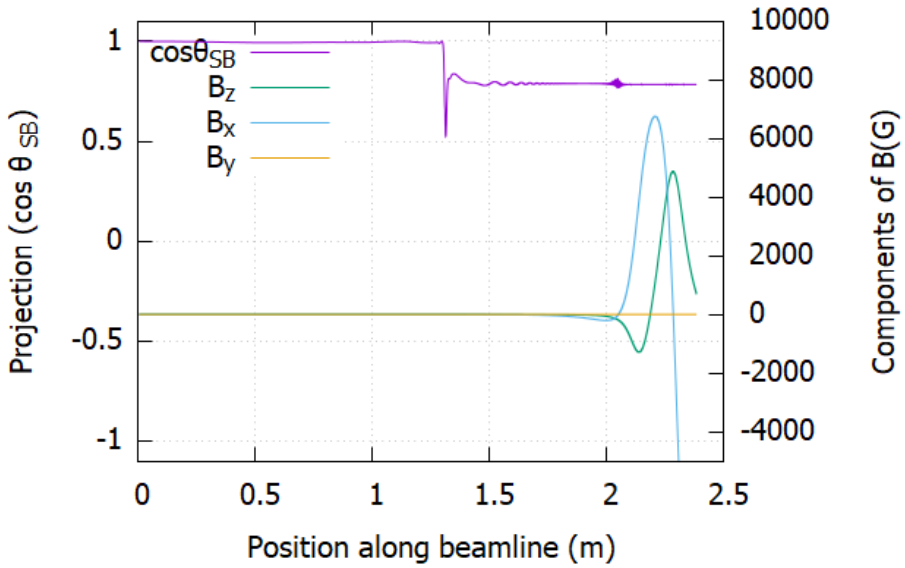

Figure 3.15: The alignment of the neutron spins as they pass through the spectrometer fields. They are transported adiabatically through the field for about 1.35m, where there is an artifact in the magnetic field data that causes a sudden change in the field. The neutron spins then precess about the field as they travel further into the magnet. Here, the fields are in blue and green, and $\cos\theta_{SB}$ is shown in purple

transport is preserved, as demonstrated in Figure 3.16.

A closer inspection of the fields in the immediate vicinity of the Spin Flipper allows for the measured data from the fields to be used, avoiding the kink in the spectrometer field. Figure 3.17 shows the alignment parameter, $\cos\theta_{SB}$ as the spins move through the first section of the field, demonstrating their adiabatic transport:

When the RF Field from the solenoid is applied, the neutron spins flip. Figure 3.18 shows the final results of the simulation, using the tuning scheme for the currents in the Spin Flipper and the transport coils described in Table 3.5.

This simulation shows that when operating at a frequency of 36.8kHz and a current of 22.5A the Spin Flipper should flip spins with an efficiency of nearly 100% at the center of the beamline.

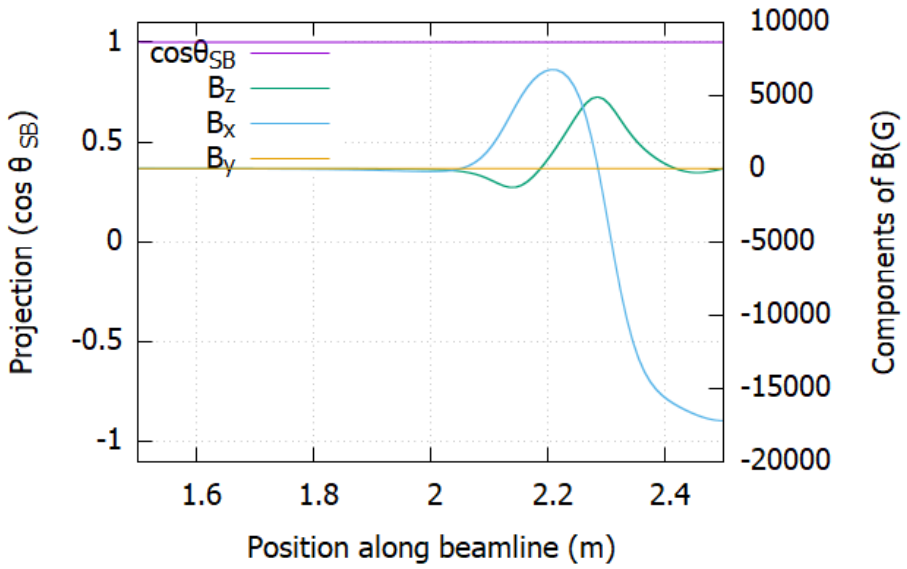

Figure 3.16: The alignment of the neutron spins as they pass through the spectrometer fields near the magnet center (x=2.5m). This shows that the field should transport spins adiabaticaly when the simulation artifact is removed.

Property	**Static Coil**	**Upstream Correction**	**Downstream Correction**
Current(A)	25A	5A	5A

Table 3.5: A table listing the currents used in the Spin Flipper model for the spin transport simulations. The Upstream Correction coil is necessary to prevent zero crossings in the simulation data, and may not be particularly useful in the real experiment.

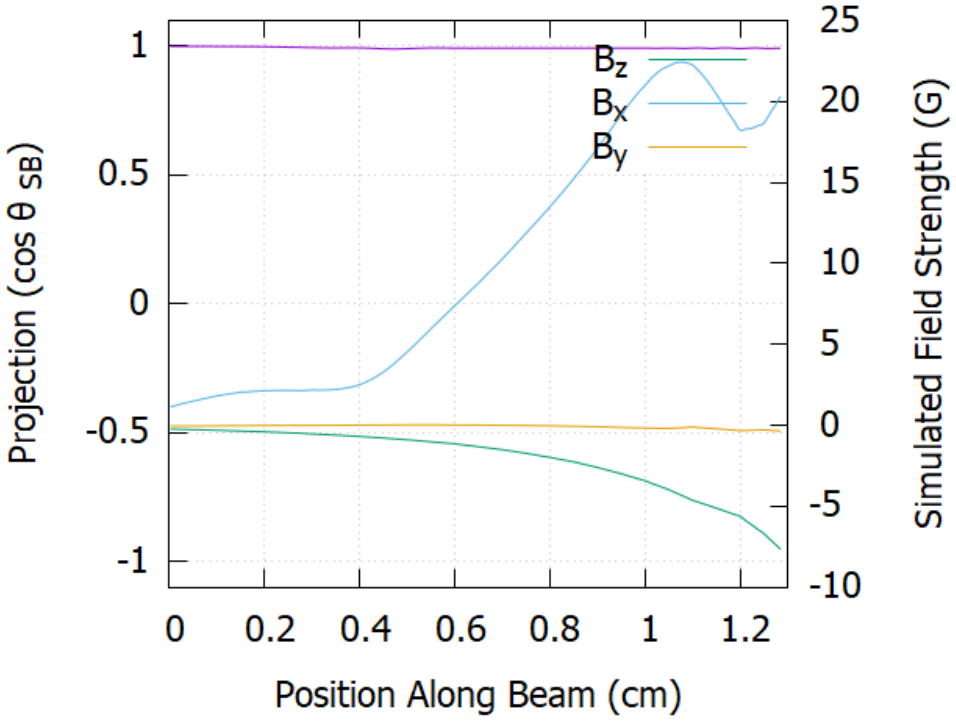

Figure 3.17: A plot $\cos\theta_{SB}$ in the magnetic fields upstream of the spectrometer with the spin flipper and compensation coils on, but no RF filed demonstrates adiabatic transport. This transport simulation uses measured data, rather than simulated data to avoid the kink.

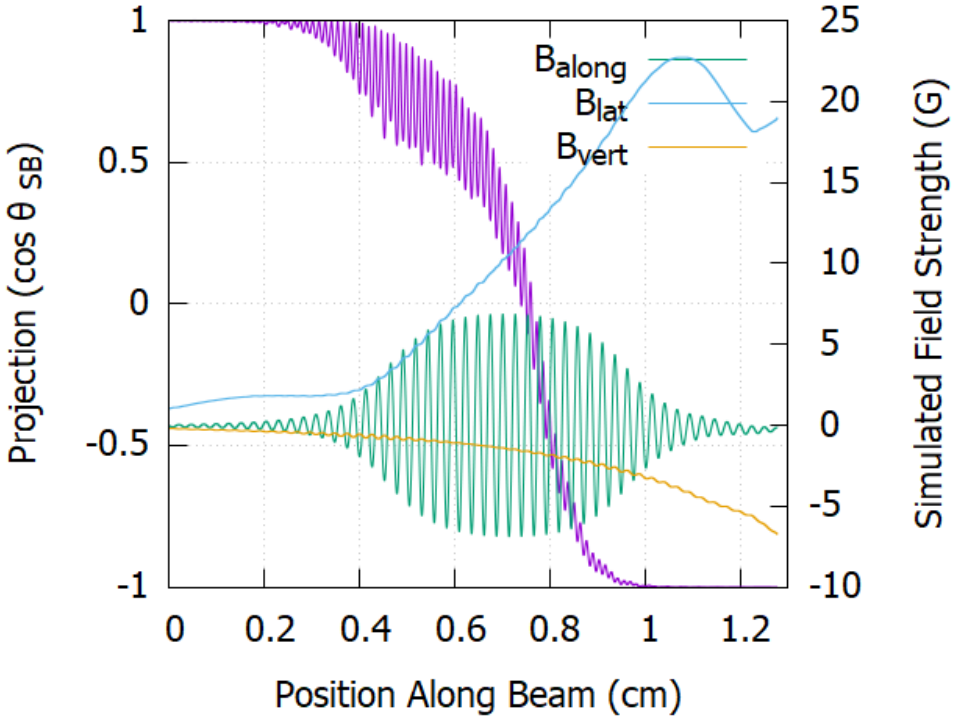

Figure 3.18: a diagram of the precession of the magnetic moment around a magnetic field when the whole Spin Flipper is on, including the RF coil. $\cos\theta_{SB}$ sweeps from +1 to -1, demonstrating a spin flip.

CHAPTER 4

^{3}He Neutron Spin Filters

As Chapter 5 will discuss in much greater detail, ^{3}He , and neutrons interact to produce an excited state of the more common ^{4}He, which has enough energy to then decay into a proton and a Triton[55]:

$$^3He + n \longrightarrow^4 He^* \longrightarrow p +^3 H \tag{4.1}$$

This interaction is only likely to occur if the spins of the neutron and the ^{3}He nuclei anti-parallel[55]. This spin dependence makes ^{3}He an excellent neutron polarizer, as small glass cells can be filled with ^{3}He , polarized, and placed in a neutron beam with relative ease. This chapter will describe methods used for polarizing ^{3}He cells, maintaining this polarization, and the cells used to analyze the neutron polarization of the FNPB.

4.1 ^{3}He Cell Fabrication

The cells used in this experiment were borrowed from an existing cell library at the SNS, and from NIST. This is because the process to create a good ^{3}He cell is somewhat of an art, and takes a considerable amount of time to do properly. Firstly, stock tubes of GE180 aluminosilicate glass are blown by a glass-blower to the proper size and shape. GE180 is used specifically because the standard borosilicate glass that a chemistry lab might use contains Boron, a neutron absorber. GE180 is also a "hard" glass, which means there is limited gas diffusion out of the cell, and

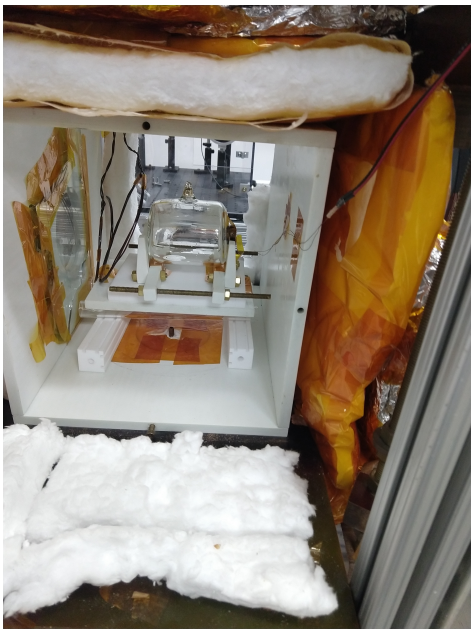

Figure 4.1: The cell Hedy Lamar on the polarizing station at the SNS

the gas atoms are less likely to interact or be adsorbed by the cell walls[56, 57]. The shaped cells are then cleaned with various chemicals and baked, to remove organic materials and other impurities, before being filled with a mixture of ^{3}He , ^{4}He, and nitrogen. Lastly, alkali metals (most commonly rubidium, but some cells also contain potassium) are chased into the cells via flame distillation, with a torch[45]. The particular cells used here are nicknamed "Scotty" and "Hedy Lamar," and Table 4.1 contains some information about the properties that distinguish them. The pressure of ^{3}He in these cells was measured by fitting the transmission spectrum of neutrons through unpolarized cells (see 5.2 for more information about this measurement).

Cell Name	**Diameter (cm)**	**Length (cm)**	**^{3}He Pressure (bar)**	**Alkali**
Hedy Lamar[58]	7.5	10	1.31	Rb +K
Scotty [59]	5.1	5.3	0.90	Rb

Table 4.1: A table containing several properties of the ^{3}He cells used for polarimetry measurements

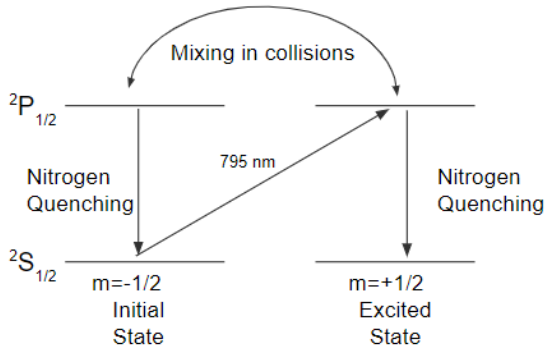

Figure 4.2: A diagram of the transitions and energy transfers associated with the electronic polarization of the rubidium atoms in SEOP. (adapted from [15]

4.2 Polarizing ^{3}He

4.2.1 Polarizing ^{3}He with SEOP

^{3}He polarizations of 70-75% are frequently achieved via Spin-Exchange Optical Pumping (SEOP) at the SNS[56]. In this process, circularly polarized laser light excites vaporized alkali atoms from the ground state ($^2S_{-1/2}$) to an excited state ($^2P_{+1/2}$), giving it a unit of angular momentum. For rubidium, the associated frequency of this transition is 795nm. The alkali atoms then collide with Nitrogen buffer gas in the cell transferring momentum between the $^2P_{+1/2}$ and $^2P_{-1/2}$ excited states. The nitrogen helps to quench some of these states, allowing some of the excited atoms to decay to the ground state and get pumped again. It also prevents radiation trapping, which de-excites atoms, and slows the polarization process. The end result of this process is a large population of alkali atoms in the spin up state ($^2S_{+1/2}$) [58, 15, 60].

The hyperfine interaction helps transfer some of the angular momentum from the electron spin to the nucleus of the atoms. The Rubidium atoms also collide with each other, further transferring nuclear polarization. Eventually, the rubidium reaches an equilibrium distribution among the sub populations of nuclear spin states, with probability of occupation ρ_a described by a spin tempera-

ture β[60, 61]:

$$\rho_a = \frac{\sinh(\beta/2)e^{\beta_a S_z}}{\sinh(\beta(S+1/2))} \frac{\sinh(\beta/2)e^{\beta_a I_{az}}}{\sinh(\beta(I+1/2))} \tag{4.2}$$

This equilibrium distribution arises quickly, but the precise rate depends on the intensity of the optical pumping light and the strength of the magnetic field in which the process occurs. [60]

The ^{3}He is polarized by interactions with the polarized alkali atoms, through both kinetic collisions, and the formation of van der Waals pairs. The polarization of the ^{3}He grows as an exponential that depends on the number density of the alkali atoms γ_{SE}, the polarization of the alkali atoms, P_A, and the rate at which the ^{3}He would naturally relax in the absence of the alkali vapors, Γ[61]:

$$P_{He} = \frac{\gamma_{SE} P_A}{\gamma_{SE} + \Gamma} \left(1 - e^{-t(\gamma_{SE}+\Gamma)}\right) \tag{4.3}$$

To perform SEOP in the polarization stations at the SNS, a prepared glass cell (see section 4.1) gets placed in an oven, and heated to ≈200 C. This vaporizes some of the alkali metal in the cell. While it is heating, the cell is exposed to laser light from a diode laser operating at 795nm. Light from this diode laser is first passed through a grating, which allows the wavelength to be finely tuned to the alkali transition. The laser light is then linearly polarized by a beam splitter, and shaped by two lenses, such that the beam covers the cell inside the oven. Lastly, the beam passes through a liquid crystal retarder, which circularly polarizes the light. At the SNS polarization station, two lasers are used, one incident on each side of the cell, such that the intensity of light across the volume of the cell is more uniform.

4.2.2 Free Induction Decay Measurements of ^{3}He Polarization

One of the most useful tools for monitoring the relative polarization of ^{3}He as it is polarized or while the polarization is decaying is Free Induction Decay. Free Induction Decay is an NMR technique wherein atoms that are aligned with a static holding field are tipped via the application

of a resonant pulse, and the oscillating signal from the atomic magnetic moments is measured as they relax.

During the SEOP procedure, the polarization of the ^{3}He is monitored by taking Free Induction Decay (FID) measurements once every 2-4hrs, while the cell polarizes overnight. When they are placed in the oven, the cells are fitted with a small pickup coil, composed of approximately 150 turns of #30 wire, with an approximate area of 1cm. This coil is usually attached to the pull-off stem, where the glass cell was originally connected to the tubes that filled it. The coil is placed such that its axis is perpendicular to the 12G holding field that surrounds the polarizing oven. A short pulse oscillating at the Larmor frequency of the ^{3}He atoms in the field is sent through the pickup coil. This tips the spins of the ^{3}He atoms, causing them to precess about the main holding field. The pickup coil then measures the signal from the precessing ^{3}He spins, as they return to alignment with the holding field. An example of an FID signal is shown in 4.3.

Software fits the FID signal for an amplitude, A, decaying exponential time constant T_2, and internal frequency, f:

$$V = Ae^{-2t}\sin(2\pi ft + \phi) \tag{4.4}$$

The amplitude of the FID signal, A, across successive measurements in the same field conditions can be used as a measure of the relative polarization. Figure 4.4 is an example plot of A, for a polarizing measurement. It demonstrates the signal saturation at the maximum achievable polarization for that cell configuration. This process takes approximately 10 hours to reach saturation but is usually left to run overnight, to be sure that the polarization process in the cell is complete. See section 4.4 for more details measurements of T_1 using FID signals.

The absolute polarization of the cell must be measured with Electron Paramagnetic Resonance (EPR), wherein a shift in the resonance frequency of the alkali atoms caused by the ^{3}He polarization is measured by monitoring the absorption of the laser light by the rubidium[62]. This can

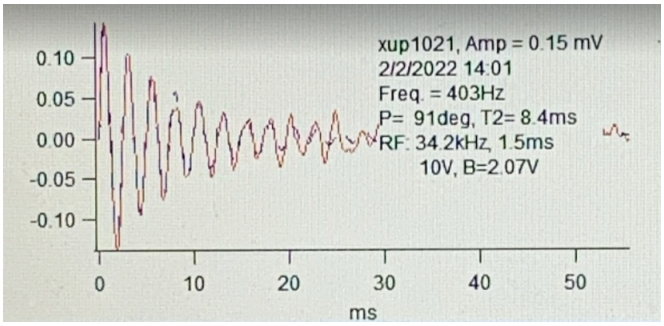

Figure 4.3: An example FID signal with associated fit parameters

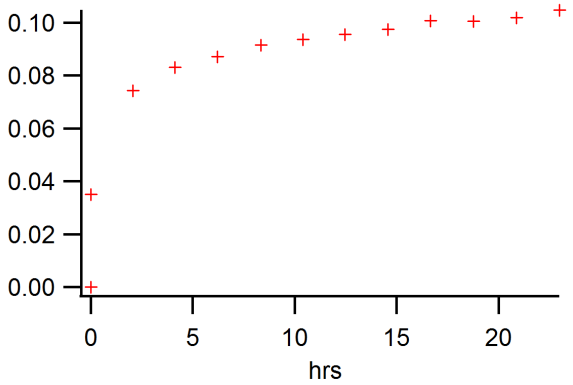

Figure 4.4: An example of the monitoring of the ^{3}He polarization as the cell saturates overnight. Here the y axis represents the strength of the emf signal induced in the pickup coil, in mV

only be performed while the cell is in the oven because the alkali metals must be in the vaporous state. This type of measurement is not particularly useful in this experiment, as once the cells are polarized, they are transported to different magnetic environments. Throughout this process, ^{3}He polarization is lost. Changes in the magnetic environment, the position of the pickup coil, and the Larmor frequency make it difficult to meaningfully compare the amplitudes of the FID signals when the cell is removed from the oven, and transported from place to place.

A better measure of the absolute ^{3}He polarization, more important to this polarimetry measurement, is the transmission spectrum of the neutron beam through the cell. This type of measurement will be discussed in Chapter 5. This type of measurement reveals the ^{3}He polarization as it sits in situ on the Nab beamline.

4.3 Maintaining ^{3}He Polarization in Magnetic Environments

4.3.1 Spin Relaxation

Once the SEOP process is complete and the ^{3}He in the cell is polarized, the laser and the heater are turned off. The alkali metals are allowed to cool and condense back into their solid forms. Since the system is not being actively pumped, the polarization of the ^{3}He begins to decay. This decay occurs via several mechanisms. The two most unavoidable mechanisms are interactions with the walls of the cells, and transverse relaxation, or spin-spin relaxation, designated T_2. Transverse relaxation occurs when the magnetic moments of the ^{3}He atoms de-phase because they precess at different frequencies while experiencing varying local magnetic fields. These variations can arise due to the presence of the magnetic moments of other nearby atoms, but can also be caused by variances in the ambient field the ^{3}He gas particles travel through (though in this case it is referred to as T_2^*). This relaxation causes the transverse components of the bulk magnetization to decay.[58, 61]This occurs on the order of milliseconds, and can be extended by assuring that ambient magnetic fields are as homogeneous as possible.

Longitudinal relaxation, or spin-lattice relaxation, is the most easily controlled mechanism

through which ^{3}He polarization is lost. This type of relaxation occurs when the ^{3}He atoms experience a change in the ambient field direction that is not adiabatic, as it travels throughout the cells. This causes a decay of the net magnetization along the prevailing field direction. The rate that this process occurs, designated as a lifetime, T_1 , is proportional to the relative transverse gradients in the cells:

$$\frac{1}{T_1} = D\frac{\nabla B_x^2 + \nabla B_y^2}{B^2} \tag{4.5}$$

where D is a diffusion constant, inversely proportional to the ^{3}He pressure in the cell.

To maintain ^{3}He polarization on the beamline, and assure that it is consistent between frames of neutron data, it is imperative that the magnetic environment that surrounds the cell maximizes T_1 , and minimizes transverse field gradients. This is most easily accomplished when there is a lot of space available for a set of coils over which to generate a field. For example, the holding field in the polarization station lab is produced by a 30-inch pair of Helmholtz coils. T_1 for "Scotty" in this coil pair is known to on the order of hundreds of hours. Space on the Nab beamline, however, is very limited, particularly in the upstream region. The coils that produce the holding fields on the beamline must fit inside the Nab shielding configuration, in cavities that aren't much bigger than 10 in. Several different types of field configurations were simulated, including various solenoids, Helmholtz pairs, magic boxes[63], and cosine(theta) coils[64], but very few of these produced adequate results. It also seems to be the case that, for many configurations, particularly where the prevailing field direction is not vertical, the field configurations that produce decent a ^{3}He T_1 do not transport the neutron spins adiabatically along the beamline. When T_1 is long, faster neutrons fall out of alignment with the static field by as much as 10%. This effect can be mitigated in the polarimetry measurement by examining the affected wavelengths a bit more closely, and gathering more statistics in the affected range.

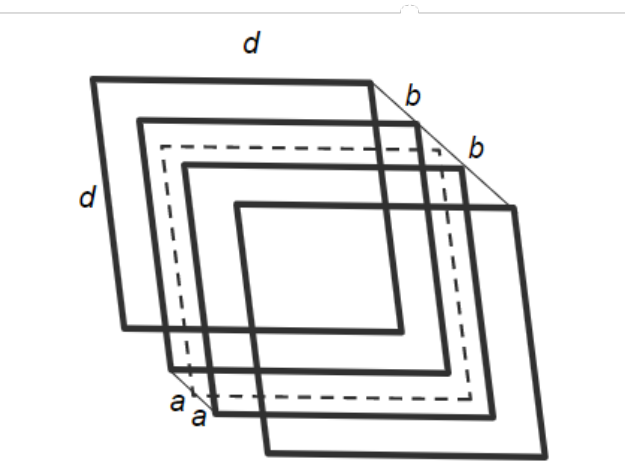

Figure 4.5: A schematic of the design for a 4-coil Merritt Coil. Here d represents the side length of each square coil, and the distances a and b are measured from the central axis of the configuration and give the spacing between the coils. (adapted from [65])

4.3.2 Merritt Coil Field Design

The best field design considered for this project is known as a Merritt coil, introduced by Merritt and Purcel in [65]. The basic principle behind this design is that adjusting parameters between pairs of square coil frames can cancel out even terms in the Taylor expansion of the fields. Because of the symmetry of these coils, the odd terms also vanish. Using four coils allows for the canceling of these expansion terms up to the 6th order. These coils will produce a particularly uniform field that points predominately along the neutron beamline, to avoid putting wires in the path of the neutron beam. A schematic diagram of the important characteristics of a Merritt coil is presented in figure 4.5.

The main dimension that defines the coil parameters is the side length of the square coil frames, d. From there, the distances between the center of the coil and each of the other coils and the

current ratio between the inner(I_i) and outer (I_o) pair can be determined:

$$\frac{a}{d} = 0.128106 \tag{4.6}$$

$$\frac{b}{d} = 0.505942 \tag{4.7}$$

$$\frac{I_i}{I_o} = 0.423514 \tag{4.8}$$

The currents are best approximated with a ratio of two integers which define the number of turns in the inner and outer coils, such that the coils can all be tied together in a series circuit and powered from a single power supply.

For this experiment, two separate coils were designed to fit in the different regions of the beamline. The upstream coil is 200mm, to fit in the smaller cavity near the beam guide exit, with some possibility to move the coils across the cross-section of the beam. The field strength upstream is limited to 10G, because a higher field may contribute to premature neutron spin flipping as they pass into fringe fields from the RF coil. They are expected to resonate and flip at 13G. The downstream coil is 220mm, which fills the space in the downstream shielding cavity. Since this coil is out of range of the spin flipper's RF field, this field can have a higher magnitude. The value of XXG in the center of the downstream Merritt coil was chosen, so that the neutron spins are transported smoothly through the coils and into the neutron monitor, and the polarization lifetime can be optimized by washing out field gradients from the spectrometer. Table 4.2 contains the rest of the properties of the two sets of coils as defined in Figure 4.5.

Simulations of these coils were constructed using BiotSavart™(see sect 3.3.1). This software outputs the magnitude of the magnetic field and its components produced by these currents on a 1 mm cubic grid. The gradients of this data were then taken and the relative transverse gradient was calculated, to estimate what the ^{3}He lifetime would be. In practice, a relative gradient less than $1 \times 10^{-5}\text{cm}^{-1}$ produces acceptably long lifetimes, but the accuracy of these estimates is strongly related the precision in the construction of the fields, and neglects contributions from other background fields. This method merely pre-screens candidates to see which field types can

perform better than others. These simulations also helped determine some of the winding details, like how the width of the frame or the depth of the turn stacking affects the relative gradient for a particular coil configuration. This is why the different coils have different sets of inner and outer pair turns. 11/26 worked well for the upstream coil, given a smaller, narrower frame. 36/85 turns produced a slightly larger relative gradient in this frame set. On the other hand, for the larger coils, 11/26 did not work as well as 26/85. Simulations with a few other pairs of integers were attempted, but it is also worth noting here that a smaller number of turns requires a higher, and sometimes unsafe, current to reach the desired field strength, and using many many turns becomes unwieldy to construct, and difficult to pack into a reasonable space, such that the width of each individual frame is small compared to the size of the Merritt Coil.

Property	**Upstream Merritt**	**Downstream Merritt**
d	200mm	220mm
a	2.56cm	2.82cm
b	10.11cm	11.12cm
Frame Thickness	3/8in	1/2 in
Inner Pair Turns	11	36
Outer Pair Turns	26	85
Current	4.285A	1.44A
Field at center	10G	10G

Table 4.2: A table containing the design properties of the two Merritt Coils designed for this experiment

The frames for these coils were constructed from aluminum u-track of the desired profile width, and then wound with #20 AWG copper wire. 3D printed plastic spacers were designed to hold the coils apart the correct distance.

4.4 Measuring T_1

To measure the lifetime (T_1) of the ^{3}He in these fields, a ^{3}He cell gets polarized in the polarization station at the SNS using SEOP. When the cell cools enough to handle, it is removed from the oven and that holding field, and moved carefully along magnetic field lines in order to avoid depolarizing

the cells with rapidly changing field directions. Once placed inside the Merritt coil, and transported to its intended location, FID measurements are tuned to accommodate the new field magnitude. The cell then gets left in the field to allow the ^{3}He polarization to decay, usually overnight. FID measurements are taken at intervals between 2 and 4 hrs, to monitor the decay. Amplitudes of successive FID measurements can then be fitted to an exponential decay model, to determine the value of T_1 in that cell and field configuration. The measured T_1 depends pretty significantly on the cell's position in the field. Small deviations in the cell's position account for large changes in the measured T_1 , because the lowes field gradients are in the center of the volume, but they get larger further from that center. Lifetimes on the order of 100hrs have been measured in the lab, however, measurements on the beamline have been difficult to achieve because of timing constraints and other logistical factors.

The value of T_1 on the beamline with the full fields of the spectrometer is what defines the "working time" of the cell on the beamline. A large portion of this working time will be spent re-stacking Nab's lead shielding after the cells and their holding fields have been put in place, which is why a significant T_1 is desirable.

Because the field from the Merritt coils points along the beamline, and the cell must be inserted into the beamline from above, Merritt coils themselves must also serve as the holding field that surrounds the cell in transportation from the ^{3}He polarizing lab to the beamline. Inserting the ^{3}He cell from above would pass the cell through the border of the Merritt coil, where the field switches direction, and depolarize the cell.

Previous experiments on the FNPB have transported cells using shielded solenoids and uninterruptible power supplies. The shielding configuration for Nab makes the use of a solenoid to transport the polarized ^{3}He cells to the beamline, and then insert them into the Merritt coils very difficult, and seriously increases the risks depolarizing the cell. Instead, the Merritt coils are designed such that the ^{3}He cell is inserted and secured to a v-block in the polarizing lab, and then the whole system is transported to the beamline. Once at the beamline, the Merritt coil assembly, complete with collimation, is lowered into place and surrounded with shielding. After perform-

ing this transport procedure a few times, checking the ^{3}He polarization with FID measurements before and after the cell in the holding field completes a round-trip to the beamline and back, it is estimated that about 10% of the ^{3}He polarization on the way to the beamline, after performing several round trips and measuring the relative polarization remaining when the cell returns to the polarization station. Because the saturated polarization is sufficiently large, and T_1 lifetime is long enough, this 10% loss shouldn't have a great effect on the polarimetry measurement. Figure 4.6 contains a photo of the final assembly of the Merritt coils, ready to be transported and placed on the beamline.

Several attempts at measuring T_1 on the beamline have been made, however, due to tuning errors, and other transportation issues, a consistent and repeatable T_1 has not yet been measured. Individual measurements have ranged from 40 to 100 hours, which is sufficient for use, however, methods for consistently maintaining long lifetimes on the beamline could still require some work.

4.5 Flipping ^{3}He Spins with AFP

To make some of the required measurements for polarimetry, and to understand some systematic errors, the spin of the polarized ^{3}He will need to be reversed. This spin flip can be completed with Adiabatic Fast Passage(AFP), just like the neutrons (see 3.1). However, unlike the neutrons, the ^{3}He atoms are not traveling along the beamline. They move as gaseous atoms, but they are pinned in a relatively uniform magnetic field inside the glass cell. In this case, to perform AFP, the static field rests at a constant value, and the frequency of the rotating field gets swept from below the Larmor Frequency to above the Larmor Frequency.

To produce the rotating field, two circular coils are attached to the outside of the Merrit coil. These coils can receive an oscillating signal from an amplified function generator, set to sweep through the proper frequency (see Figure 4.6)

To measure the efficiency of this system when flipping spins, several AFP flips are performed in close succession. A sweep takes about a few hundred milliseconds to complete. After a given

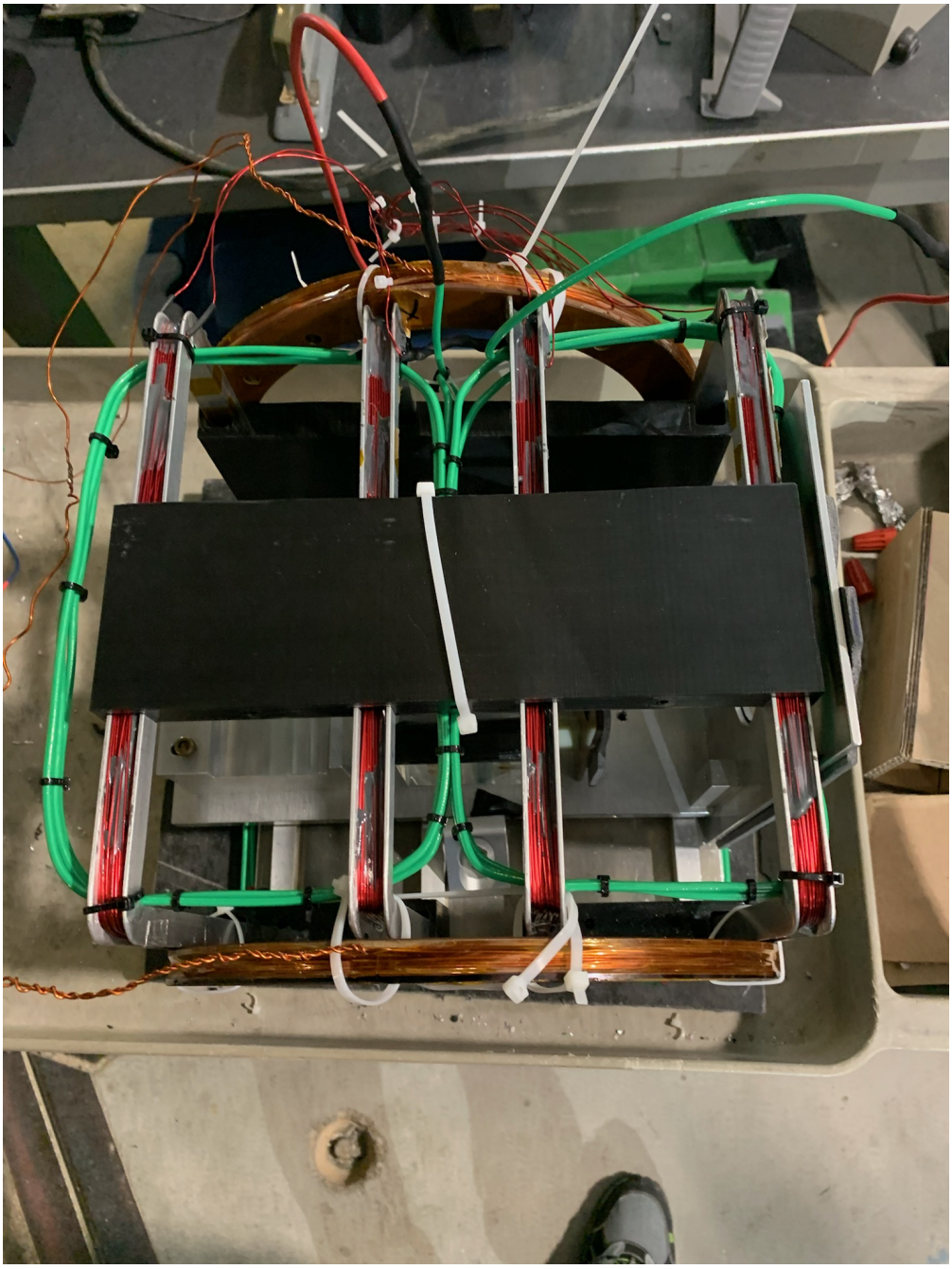

Figure 4.6: The Merritt coils as assembled for transport and placement on the beamline, complete with tuning coils to moderate background field gradients, and AFP coils to flip the ^{3}He spins.

number of sweeps, an FID measurement is taken. Because the coils and the ^{3}He are still in the same field, the amplitude of these FID measurements gives a reasonably accurate measurement of the relative polarization remaining after several flips.

After some final adjustments and tuning, it was estimated that the efficiency of this spin flip is 97% in the polarizing lab, however, this did not prove to be repeatable on the beamline, and may require a more powerful amplifier or some improved circuitry that may make the frequency sweep easier to perform.

4.6 Final Adjustments and Tuning

Based on some early measurements of T_1 for the ^{3}He cells on the beamline, as well as some simulations of the fringing fields from the magnetic spectrometer, the gradients associated with the spectrometer's field are too big to wash out simply by increasing the field in the Downstream Merritt coils themselves. To remedy this issue, two pairs of rectangular auxiliary coils were inserted inside the Merritt coil, such that they produce a vertical field. By running each vertical pair with a different current, these fields can be tuned to cancel out some of the gradient associated with the spectrometer fringing field.

By running the individual frames (or different pairs of frames) of the Merritt Coils on separate power supplies, gradients associated with the component along the beamline can also be tuned out. This doesn't have a major effect on T_1 , but it does extend T_2^*, and the lifetime of the oscillations in the FID signal. This extension makes the FID signals easier to fit, and improves the signal-to-noise ratio for the individual FID measurements. This has to be done delicately, however, because if the gradient of the field changes for one component, it also changes for the cross terms, inducing extra field gradients in the transverse components of the field that also need canceling by the vertical coil pair. As of this writing, these coils have not been tested or tuned on beamline conditions.

CHAPTER 5

Neutron Polarimetry with ^{3}He

As mentioned in Section 1.1, Neutrons, like electrons, protons, and neutrinos, are fermions; they have a spin of $\frac{1}{2}$. The spin polarization of an ensemble of neutrons can be defined as:

$$P = \frac{N_+ - N_-}{N_+ + N_-} = \frac{N_+ - N_-}{N} \tag{5.1}$$

where N_+ is the number of spin-up neutrons, N_- is the number of spin down neutrons, and $N_+ + N_- = N$, the total number of neutrons. A polarimetry measurement is simply a comparison of counts when the neutron beam is passed through filters that preferentially absorb neutrons in a particular spin state. In this case, these filters are glass cells filled with ^{3}He . This chapter will walk through a careful analysis of the different ways a polarimetry measurement can be made, and how the properties of the equipment used to perform a polarimetry measurement affect its results. Chapter 4 describes in much more detail the actual properties of the ^{3}He cells used in the experiment and how those cells and their polarizations are maintained.

As noted in Section 2.4, the beam polarization for the Nab experiment must be below 2×10^{-5}. If one could simply count the number of up neutrons and the number of down neutrons with a statistical error of $\sqrt{N_+}$ and $\sqrt{N_-}$ we would find that the uncertainty on our measurement looks like:

$$\sigma_{P_n} = \sqrt{\frac{1 - P_n^2}{N}} \tag{5.2}$$

If $\sigma_{P_n} = 1 \times 10^{-5}$, approximately 10^{10} neutrons will need to be counted in this experiment, which can happen very quickly when all the neutrons in the beam can be utilized.

5.1 Data Acquisition with the 60Hz DAQ

The Data Acquisition system for this polarimetry measurement is constructed around a D-tAcq ACQ1002R unit (the DAQ unit) - A 24-bit analog-to-digital converter that records several channels of analog voltage data. It was previously used in the NPDGamma experiment, for similar purposes. The DAQ unit is triggered at a rate of 60Hz, usually with the trigger syncing signal from the SNS Accelerator T0 signal- The TTL logic pulse that indicates a proton pulse has been released from the accelerator to strike the mercury target. When it receives this trigger, it waits for some specified time delay (this is a delay time associated with the neutrons traveling down the beamguide before they reach either monitor). Then, it records a series of 1333 voltage samples at 80kHz cycling through each of its active channels. 32 consecutive samples are averaged together to smooth out the data, resulting in an ”event.” Each ”event” is a 16.66ms histogram of ADC bins from the various channels, divided into 40 time bins. While the DAQ is running, it collects consecutive events into a file of a specified size or run length. These data files are archived for analysis later. They cannot be accessed while a file is being recorded.

The DAQ is connected to a 32-Channel breakout box. The DAQ can technically accommodate up to 48 channels of data, but some seem to exhibit quite a bit of cross-talk and extra noise. Only a handful of channels are required for monitoring this experiment, anyway. These signals also come through the DAQ, so that everything is correlated to the time/event that it was observed alongside. These signals include but are not necessarily limited to:

- The voltage across a shunt resistor connected to constant current supplies, to monitor fluctuations in the field associated with the Gradient coil, transport coils, and other static fields.
- The voltage across a shunt resistor connected to the RF coil to determine whether the RF Coil is oscillating, powered off, or in a transient state. (a copy of the channel that provides

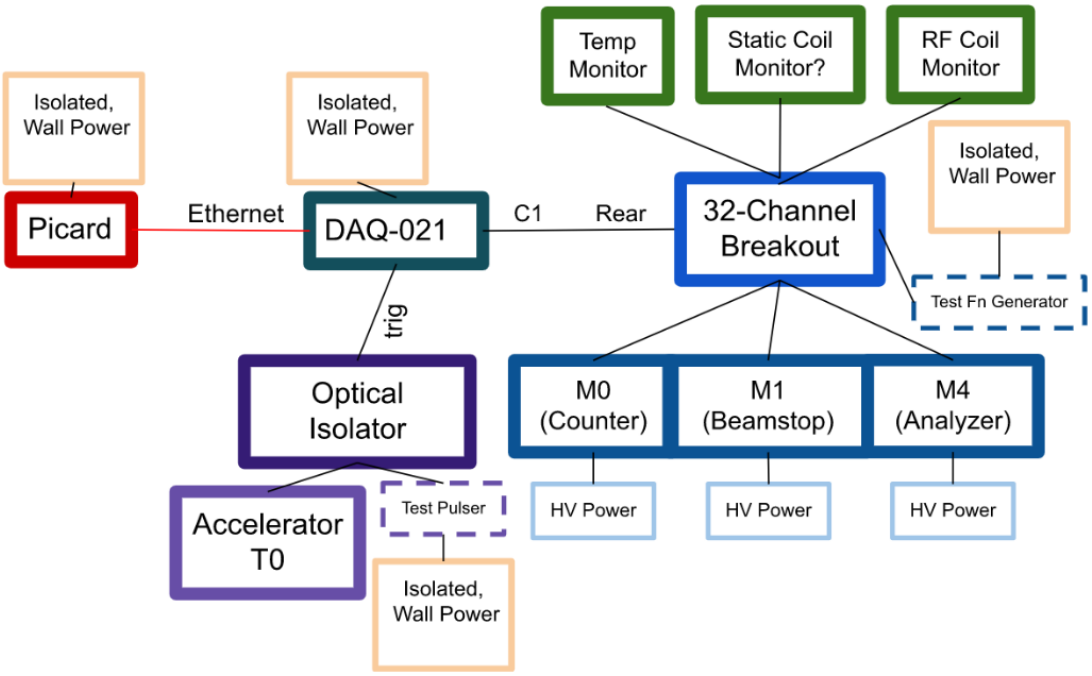

Figure 5.1: A map of the Data Acquisition system and its connections to other systems that should be monitored during polarimetry

the control signal to the RF coil may also be included)

- The temperature of the Gradient coil-if the gradient coil exceeds a certain temperature threshold, it should be shut down. This would indicate a major cooling system failure.

- Neutron Monitors

Figure 5.1 shows a map of the DAQ and its connected equipment.

5.1.1 The Neutron Monitors

The most important channels of information on the DAQ are the data from the neutron monitors. There should usually be 2 monitors in operation. The first is a normalizing monitor, used to monitor the incoming beam so that each pulse can be normalized against fluctuations in the neutron source intensity. The monitor used for this purpose is a low detection efficiency single-wire counter chamber. Because of its low efficiency, it tends to display individual counts- particularly at low

count rates, yielding a discontinuous signal that is difficult to interpret with our 60Hz DAQ. In this case, a shaping capacitor was added to the amplifier on the monitor output to expand these pulses, which allows them to pile up in such a way that the neutron flux can be inferred from the signal in an event. The monitor is also used with a Rate meter, which can convert a count rate into an analog voltage signal that can be read smoothly by the DAQ. An example plot of an event as seen by the normalizing monitor is shown in Figure 5.2.

The second monitor is located downstream of the spectrometer. It has much higher efficiency and will serve as the main source of the neutron transmission signals necessary to obtain a polarimetry measurement. It naturally operates in "current mode," so the voltage signal read by the DAQ is proportional to the neutron flux through the monitor. An example of a few events as seen by the analyzing monitor can be seen in Figure 5.2. The monitor signals have different biases but demonstrate the expected features of the neutron. The large peak that is synced with the trigger signal in the normalizing monitor is an electronic effect. It can be removed when the capacitance added to the normalizing monitor is balanced properly.

Because both monitors are a fixed distance from the pulsed neutron source, the time bin labels of the histograms can be converted to represent the wavelengths of the neutrons, according to the following formula:

$$\lambda_i = \frac{h}{m_n d}\left(\frac{T}{N}t_i - t_{off}\right) \tag{5.3}$$

Here, T, is the period of the event, N is the number of time bins, and t_{off} is the offset time that the DAQ waits after receiving a trigger to record. The distance to the monitor, d can be calculated using known wavelengths associated with neutrons that are scattered out of the beamline by the aluminum windows via Bragg diffraction. The spectrum observed on BL13 is fairly consistent with a thermal distribution, however, because of this Bragg scattering, there are several narrow dips in the spectrum(see Figure5.2 Table 5.1 shows the calculated distance between each monitor and the moderator, using known wavelengths from a dip in the spectrum. Those wavelengths are

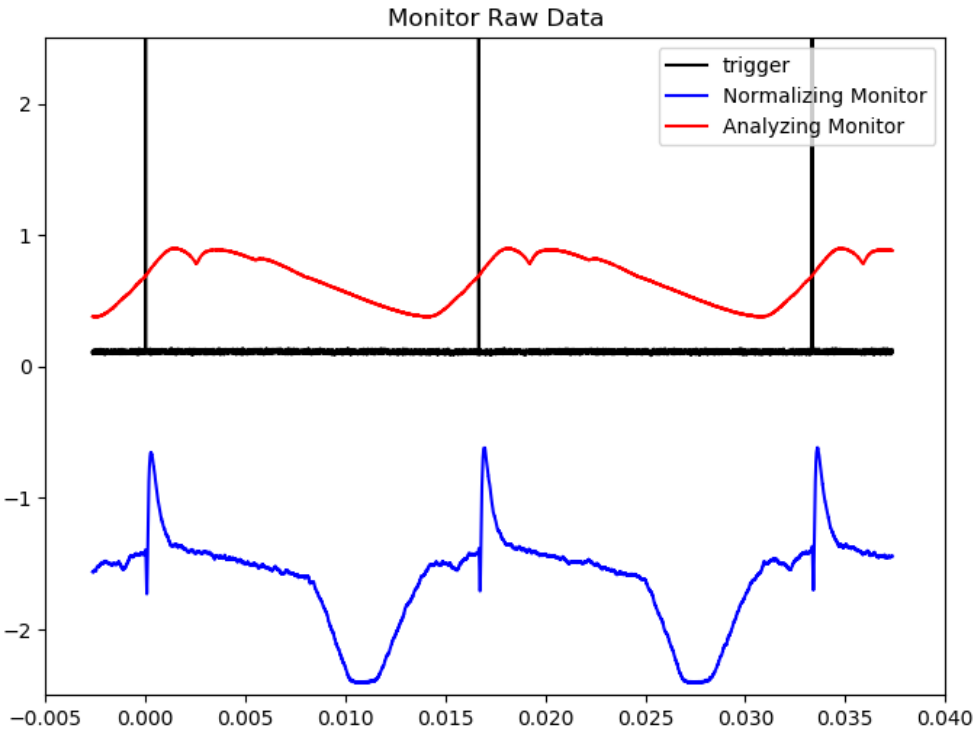

Figure 5.2: A sample of a few event pulses (denoted by the trigger) as seen by the neutron monitors on an oscilloscope. These monitors have different biases but demonstrate the expected features of the neutron. The large peak that is synced with the trigger signal in the normalizing monitor is an electronic effect. It can be removed when the capacitance added to the normalizing monitor is balanced properly. The dips in both of the monitor signals are from neutrons that are scattered away from the beamline by aluminum windows in the beam via Bragg scattering.

Source	Wavelength	Distance to Normalizing Monitor	Distance to Analyzing Monitor
Aluminum Bragg diffraction	$4.05 \times 10^{-10} m$	15.1	18.6

Table 5.1: A table containing estimations of the distance between the source moderator and the monitors, calculated by lining up the Bragg diffraction dips in the spectrum with their proper wavelength.

Property	Chopper 1	Chopper 2
Distance from Moderator	5.5m	7.5m
Cutout Angle	131^0	167^0
Set Phase	c_1	c_2

Table 5.2: A table containing the parameters associated with each chopper on the beamline. The choppers rotate at the repetition rate of the proton source, so setting the phases of the choppers, c_1 and c_2 can selectively block neutrons that do not pass through the cutout on the chopper disk.[36]

4.05×10^{-10}m and 4.68×10^{-10}m[58].

5.1.2 Choppers and Frame Overlap

The neutron pulses that come from the SNS demonstrate a considerable frame overlap- slower neutrons from one pulse arrive at the experiment along with the start of laser pulses. Figure 5.3 shows the layers of overlap that contribute to a neutron signal as seen by the monitors, based on a simulated thermal spectrum (see section 5.2). Usually, choppers along the beam can be employed to block these overlapped neutrons. These choppers are large metal disks coated with neutron absorbers, that contain windows that allow neutrons to pass through as they rotate past the beam. Table 5.2 contains some of the relevant chopper properties for this experiment[36]. By adjusting the phase of the chopper rotations, different bands of neutron velocities can be selected, because only certain neutrons are allowed to pass through the chopper window.

In order to maximize statistics for the Nab experiment, it should ideally run without choppers, however, the analysis for polarimetry requires spectra to be compared wavelength by wavelength (see the following sections), and not by sum. The choppers need to run for at least parts of polarimetry so that these comparisons can be made accurately, however, there are some concerns that

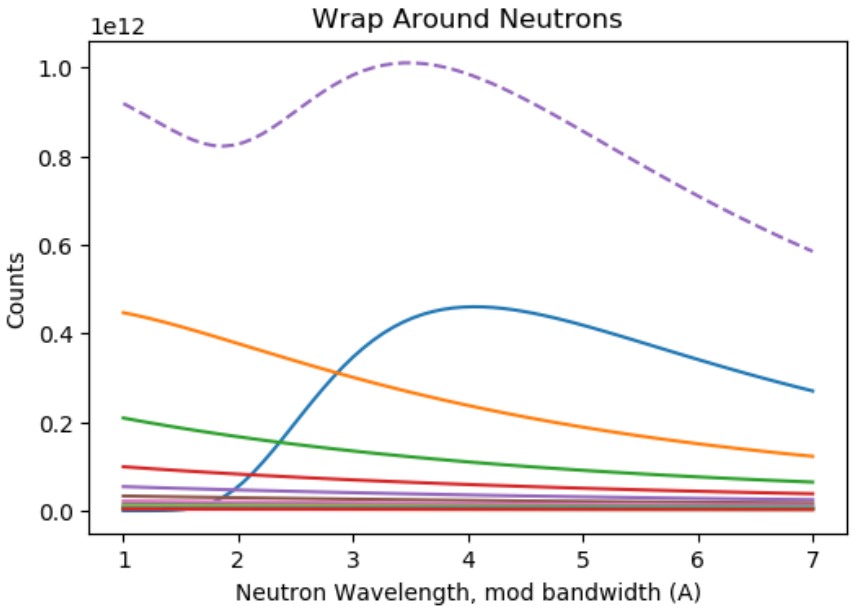

Figure 5.3: The frame overlap of neutrons from previous pulses in one event as viewed by the analyzing monitor. Here the total accumulated signal is given by the dashed line, and each solid line represents a portion of slow neutrons that make it to the monitor from previous pulses of the proton source.

the running of the choppers themselves will contribute to or alter the beam polarization. This will need to be checked, by running both with and without choppers, to see if a distinguishable change in the signal is present.

5.2 Neutron Transmission through Polarized ^{3}He

^{3}He , a somewhat rare isotope of Helium, is an incredibly useful tool in detecting and measuring an ensemble of neutrons. In the singlet state, neutrons collide with ^{3}He nuclei to produce an excited state of the more common ^{4}He, which has enough energy to then decay into a proton and a Triton[55]:

$$^3He + n \longrightarrow^4 He^* \longrightarrow p +^3 H \tag{5.4}$$

This interaction is often applied in neutron beam monitors because the resultant proton can be

captured across a potential difference and used to induce a current, but this interaction also carries a significant spin dependence- That is to say, the neutron is only likely to be absorbed by the ^{3}He if the spins of the neutron and the ^{3}He nuclei interact in the singlet state, and their nuclear spins are antiparallel. The cross-section, in this case, is about 6000 bn/angstrom (note: it also carries a wavelength dependence), whereas the parallel spin configuration has a cross-section of about 599 bn [55]. The cross-section, particularly at short wavelengths is also linear with respect to the wavelength (it follows the $1/v$ law)[58, 15]:

$$\sigma_n(\lambda) = \frac{\sigma_0}{\lambda_0}\lambda \tag{5.5}$$

The reference values commonly used for the cells in this work are $\sigma_0 = 5316bn$ and $\lambda_0 = 1.798 * 10^{-10}m$[15]. This may vary from cell to cell, based on how other aspects of the cell's composition affect the neutron capture cross-section in the cell.

The change in spin-up neutron transmission across a thin layer of polarized ^{3}He can be described by the number of interactions that occur in that film ($n_\downarrow$, the number density of the ^{3}He in the opposite state, σ is the cross-section, and dx is the width of the layer):

$$\frac{dT_\uparrow}{T_\uparrow} = -\, n_\downarrow \sigma_{\uparrow\downarrow}(\lambda) dx \tag{5.6}$$

$$n_\downarrow = \frac{n}{2}\left(1 - P_H\right), \quad \sigma_{\uparrow\downarrow} = 2\sigma(\lambda) \tag{5.7}$$

$$\frac{dT_\uparrow}{T_\uparrow} = -\,\frac{n\sigma_0}{\lambda_0}\lambda\left(1 - P_H\right) dx \tag{5.8}$$

If the transmission through this thin layer is integrated across a thickness, h of a ^{3}He cell, the number of spin-up neutrons transmitted at each wavelength λ are given by the following:

$$T_\uparrow = N_s(\lambda)\frac{1 + P_n}{2} e^{-nh\frac{\sigma_0}{\lambda_0}\lambda(1-P_H)} \tag{5.9}$$

The Number of spin-down neutrons transmitted at each wavelength can be found by swapping the

relative polarizations and is given by:

$$T_{\downarrow} = N_s(\lambda)\frac{1-P_n}{2}e^{-nh\frac{\sigma_0}{\lambda_0}\lambda(1+P_H)} \tag{5.10}$$

The total number of transmitted neutrons that make it to the detector is then

$$T(\lambda) = N_s(\lambda)e^{-\frac{nh\sigma_0}{\lambda_0}\lambda}\left(\cosh\left(\frac{nh\sigma_0}{\lambda_0}\lambda P_H\right) + P_n \sinh\left(\frac{nh\sigma_0}{\lambda_0}\lambda P_H\right)\right) \tag{5.11}$$

$N_s(\lambda)$ is the underlying spectrum of neutrons in one pulse of the beam. Here it will be approximated by a thermal spectrum at 20K (the temperature of the moderator at the SNS)[36], though an expression like this neglects brag diffraction of neutrons of a specific wavelength and the monochromator that sips neutrons off of BL13 beam for the nEDM experiment on BL13A.

$$N_s(\lambda) = N_0\left(\frac{m}{2\pi kT}\right)^{3/2}\frac{4\pi h^2}{m^2\lambda^g}e^{\frac{-h^2}{2mkT\lambda^2}} \tag{5.12}$$

The free parameter g is used to parameterize some uncertainty associated with the shape of the underlying spectrum, including shifts that result from the way the distribution is sampled based on collimation and other effects. It should have a value between 2 and 4, and will be fit to the data. It is anticipated that the spectral shape from the source moderator should be somewhat consistent from pulse to pulse, and should then divide out in ratios of measurements, however, in practice an upstream normalizing monitor will be employed to track fluctuations in the source output spectrum when possible.

To make the analysis a little easier to follow from here, the following parameters are defined:

$$a = N_0\left(\frac{m}{2\pi kT}\right)^{3/2}\frac{4\pi h^2}{m^2} \tag{5.13}$$

$$b = \frac{h^2}{2mkT} \tag{5.14}$$

$$c = \frac{nh\sigma_0}{\lambda_0} \tag{5.15}$$

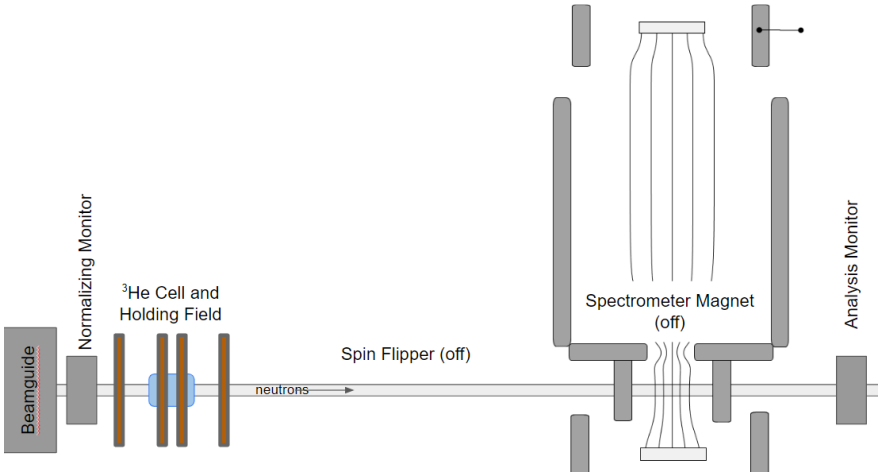

Figure 5.4: A schematic (not to scale) of the setup associated with a ^{3}He only polarimetry measurement. The beam exits the beam guide, and passes through a low-efficiency normalizing monitor, the ^{3}He cell, and then further down the beamline, an analyzing monitor. The polarization of the ^{3}He can be manipulated using AFP. The Spectrometer and the Spin Flipper remain off for this measurement.

So, more explicitly, the wavelength dependence on a thermal spectrum of neutrons transmitted through a sample of polarized ^{3}He can be expressed as:

$$N(\lambda) = \frac{a}{\lambda^g} e^{-\left(b/\lambda^2 + c\lambda\right)} \left(\cosh\left(cP_H\lambda\right) + P_n \sinh\left(cP_H\lambda\right)\right) \tag{5.16}$$

5.3 Neutron Polarimetry Without a Spin Flipper

One way to obtain an estimate of the polarization of the beam as it exits the beam guide is to compare transmission measurements of the beam through a single ^{3}He cell, placed right at the beam guide exit. See Figure 5.4 for a schematic drawing of this kind of setup. This is similar to what the aCORN experiment used to measure their beam polarization, however, the functional form of their data was integrated across neutron wavelengths because the experiment took place on a continuous beam, and wavelength information could not necessarily be extracted from time-of-flight data.[66]

The beam exits the beam guide and passes through a low-efficiency normalizing monitor, the

^{3}He cell. 3m further down the beamline on the other side of the Spectrometer Magnet (which is here powered off), the neutrons are counted in an analyzing monitor. To change which spins are filtered to the analyzing monitor, the spins of the ^{3}He can be flipped with Adiabatic Fast Passage (See sections 3.1 and 4.5)

This method of measurement is flexible and convenient to perform because it does not rely on a thorough understanding of the efficiency of the Spin Flipper. In fact, except for the holding field that maintains the ^{3}He polarization, all the other experimental fields can be turned off. The cell in the upstream position filters out the desired spin state and the neutrons are free to travel through the rest of the evacuated beam pipe to the analyzing monitor, but they do not need to be transported adiabatically–the undesired spin state is already gone. Turning off the background fields will improve the working lifetime of the ^{3}He cell and generate better statistics. FID measurements and fits of the neutron spectra themselves can also be used as an independent measure of the AFP spin flip efficiency on the ^{3}He spins.

The drawback to this method, however, lies in the analysis. Because the polarization of the ^{3}He is changing between configurations, the transmission measurement ratios aren't as easily reducible to a polarization measurement as can be seen in Section 5.4, a polarimetry measurement with the neutron Spin Flipper. It is made significantly easier if the method used to flip the ^{3}He spin is very high efficiency.

The ^{3}He -Only polarimetry requires four different transmission measurements. The first is of the beam directly on the monitors, with no ^{3}He cell in place. This helps to obtain the average beam characteristics-the parameters a, b, c, and g, and how those parameters might vary from pulse to pulse 5.16:

$$N_s(\lambda) = \frac{a}{\lambda^g} e^{-\left(b/\lambda^2\right)} \tag{5.17}$$

The second transmission measurement is through a polarized ^{3}He cell, N_+:

$$N_+(\lambda) = \frac{a}{\lambda^g} e^{-\left(b/\lambda^2 + c\lambda\right)} \left(\cosh\left(cP_H\lambda\right) + P_n \sinh\left(cP_H\lambda\right)\right) \tag{5.18}$$

The third, N_-, is a transmission measurement through that same cell, but with the polarization of the cell reversed with Adiabatic Fast Passage (AFP). Here the helium polarization is multiplied by a factor of $(1 - 2\epsilon_H)$, which represents the efficiency of the AFP flip.

$$N_-(\lambda) = \frac{a}{\lambda^g} e^{-\left(b/\lambda^2 + c\lambda\right)} \left(\cosh\left(c\left(1 - 2\epsilon_H\right)P_H\lambda\right) + P_n \sinh\left(c\left(1 - 2\epsilon_H\right)P_H\lambda\right)\right) \tag{5.19}$$

And the last is through an unpolarized ^{3}He cell. This is simply the previous equations, but P_H is zero, so the hyperbolic trig functions simplify to zero and 1.

$$N_0(\lambda) = \frac{a}{\lambda^g} e^{-\left(b/\lambda^2 + c\lambda\right)} \tag{5.20}$$

When performed in this order, all the data required for one polarimetry measurement can be taken during one placement of the ^{3}He cell. The cell can be polarized, brought to the beamline in its holding field, and put in place for the polarized measurement. Then the lead shielding can be stacked back around the holding field device. While exposed to neutrons, the ^{3}He spins can then be flipped several times over the lifetime of the ^{3}He spin polarization (T_1) inside the shielding to produce measurements of both N_+ and N_-. The relative polarization of the ^{3}He cell can be checked on occasion using FID measurements. Once the ^{3}He polarization has decayed sufficiently, the cell can be "scrambled" by de-tuning the holding field coils, and applying a field with a very high transverse gradient. When the ^{3}He polarization is scrambled, a measurement of N_0 can be performed. Then the shielding can be unstacked and the holding field can be removed to re-polarize the cell and take new measurements.

The ratio between the bare beam and the unpolarized beam, R_{0s}, can be used to extract c, and measure the "thickness" of the ^{3}He cell. This is a property of the cell itself, and shouldn't fluctuate

between measurements.

$$R_{0s} = \frac{N_0}{N_s} = e^{-\lambda c} \tag{5.21}$$

Then, the ratios between the polarized ^{3}He runs and the unpolarized ^{3}He runs should be constructed.

$$R_+ = \frac{N_+}{N_0} = \cosh\left(cP_H\lambda\right) + P_n \sinh\left(cP_H\lambda\right) \tag{5.22}$$

$$R_- = \frac{N_-}{N_0} = \cosh\left(c\left(1-2\epsilon_H\right)P_H\lambda\right) - P_n \sinh\left(c\left(1-2\epsilon_H\right)P_H\lambda\right) \tag{5.23}$$

These ratios can be fitted with a least-squares fitting method to extract the product cP_H, and obtain an estimate of the ^{3}He polarization. Pairs of measurements with the ^{3}He flipped and unflipped can be compared to determine a value for ϵ_H associated with that pair of measurements, and then the ratios between flipped and unflipped measurements can be combined to create a Combined Transmission Ratio (CTR):

$$CTR = \frac{R_+ - R_-}{R_+ + R_-} = \tanh\left(cP_H\lambda\epsilon_H\right)\left[\frac{\sinh\left(\frac{cP_H\lambda}{2}\left(1-\epsilon_H\right)\right) - P_n\cosh\left(\frac{cP_H\lambda}{2}\left(1-\epsilon_H\right)\right)}{\cosh\left(\frac{cP_H\lambda}{2}\left(1-\epsilon_H\right)\right) + P_n\sinh\left(\frac{cP_H\lambda}{2}\left(1-\epsilon_H\right)\right)}\right] \tag{5.24}$$

As ϵ_H approaches 1, the CTR becomes a $\tanh$ function, and the polarization is merely the amplitude associated with that function:

$$CTR_{\epsilon_H\to 1} = \frac{R_+ - R_-}{R_+ + R_-} = -P_n \tanh\left(cP_H\lambda\right) \tag{5.25}$$

This $\tanh$ function can be fit using standard least squares curve fitting methods, but P_n is small, and the product of c, P_H, and λ is usually of order 1. The question remains, how close must ϵ_h be to 1 in order for this fit to be valid?

If the bracketed expression in 5.24 is Taylor expanded to second order about where $\left(1-\epsilon_H\right)$ is

very small, that expression becomes:

$$-P_n + \left(\frac{cP_H\lambda}{2}\right)\left(P_n^2+1\right)(1-\epsilon_H) - \left(\frac{cP_H\lambda}{2}\right)^2 P_n(P_n^2+1)(1-\epsilon_H)^2 \tag{5.26}$$

It will be important to keep track of the size of corrections to this term, depending on the measured value of ϵ_H.

The polarization, P_H itself will also be decaying with time. Section 4.5 describes how AFP can be used to flip the ^{3}He spins, and how ϵ_H can be measured with free-induction decay measurements. In order to measure the absolute polarization of the ^{3}He cells on the beamline, however, it is best to fit the spectra, and then the absolute efficiency between any pair of measurements can be determined exactly.

The uncertainty in the CTR, σ_{CTR} is the uncertainty on the transmission measurements, added in quadrature:

$$\sigma_{CTR}^2 = \left(\frac{\partial CTR}{\partial R_+}\right)^2 \sigma_{R_+}^2 + \left(\frac{\partial CTR}{\partial R_-}\right)^2 \sigma_{R_-}^2 \tag{5.27}$$

$$= \frac{4\left(R_-^2\sigma_{R_+}^2 + R_+^2{\sigma_{R_-}}^2\right)}{\left(R_+ + R_-\right)^4} \tag{5.28}$$

The uncertainty on the transmission measurements caused by the uncertainty in the ^{3}He polarization is:

$$\sigma_{R_+}^2 = \left(\frac{\partial R_+}{\partial P_H}\sigma_{P_H}\right)^2 = \left(c\lambda\sigma_{P_H}\left[\sinh\left(cP_H\lambda\right) + P_n\cosh\left(cP_H\lambda\right)\right]\right)^2 \tag{5.29}$$

$$\sigma_{R_-}^2 = \left(\frac{\partial R_-}{\partial P_H}\sigma_{P_H}\right)^2 = \left(c\lambda\left(1-2\epsilon_H\right)\sigma_{P_H}\left[\sinh\left(cP_H\left(1-2\epsilon_H\right)\lambda\right) + P_n\cosh\left(cP_H\left(1-2\epsilon_H\right)\lambda\right)\right]\right)^2 \tag{5.30}$$

(Note, this can also be expanded to encompass uncertainties in the wavelength and counting statistics by adding them in quadrature) This leads to a fractional uncertainty that can be expressed

as:

$$\frac{\sigma_{CTR}}{CTR} = \frac{4\left(R_-^2\sigma_{R_+}^2 + R_+^2\sigma_{R_-}^2\right)}{\left(R_+ + R_-\right)^3\left(R_+ - R_-\right)} \tag{5.31}$$

These uncertainties and their affect on the uncertainty of the polarization will need calculated when the ^{3}He polarization and its decay are better understood.

5.4 Neutron Polarimetry With a Spin Flipper

Neutron Polarimetry with a Spin Flipper requires more or less the same set of measurements, but the setup is a little different. This type of measurement requires all the experimental fields to be powered on and tuned such that the neutron spins are transported adiabatically through the experiment. The neutrons leave the beam guide, and pass through a normalizing monitor, the Spin Flipper, the decay region of the spectrometer, and then a ^{3}He analyzer and neutron monitor further downstream. Because the position of the monitor will move relative to the Spin-Flipper free measurement the baseline measurements, N_s and N_0, will need to be retaken. They will look similar, mathematically, but it is likely that different ^{3}He cells will be used for this measurement, and a different overall beam intensity will be observed further down the beamline in the analyzing monitor's new position.

See Figure 5.5 for a schematic diagram of this type of experiment. This measurement also requires a thorough understanding of the efficiency of the Spin Flipper, which will need to be measured in a different suite of measurements. See section 5.5 for a discussion of this measurement.

Mathematically, the neutron polarization gets multiplied by $(1-2\epsilon_n)$, where ϵ_n is the efficiency of the Spin Flipper when the neutrons are flipped. The neutron transmission through the analyzer

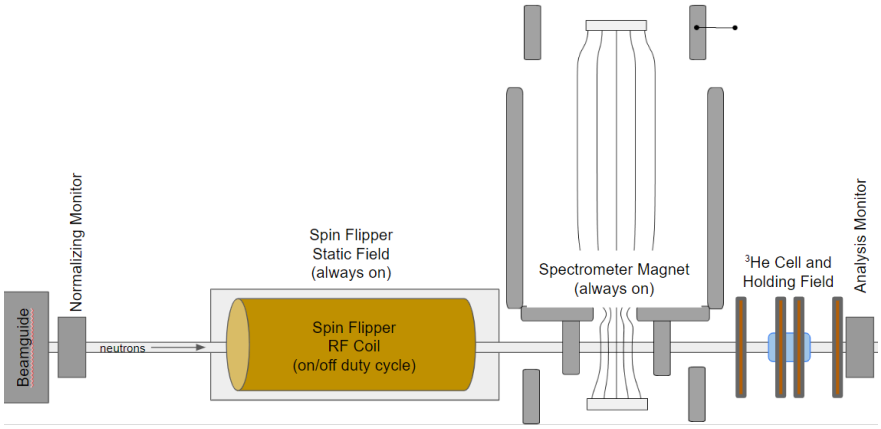

Figure 5.5: Schematic (not to scale) of a polarimetry measurement with the spin flipper. The beam exits the beamguide, and passes through a low-efficiency monitor. The neutrons are carried adiabatically through the static fields of the experiment setup to ^{3}He analyzer cell and the final monitor. At certain time intervals, the RF coil inside the Spin Flipper is turned on to flip the spins of the neutrons relative to the field and the spins of the ^{3}He in the analyzer cell.

for the four necessary measurements here can be expressed as:

$$N_s(\lambda) = \frac{a}{\lambda^g} e^{-\left(b/\lambda^2\right)} \tag{5.32}$$

$$N_0(\lambda) = \frac{a}{\lambda^g} e^{-\left(b/\lambda^2 + c\lambda\right)} \tag{5.33}$$

$$N_+(\lambda) = \frac{a}{\lambda^g} e^{-\left(b/\lambda^2 + c\lambda\right)} \left(\cosh\left(cP_H\lambda\right) + P_n \sinh\left(cP_H\lambda\right)\right) \tag{5.34}$$

$$N_-(\lambda) = \frac{a}{\lambda^g} e^{-\left(b/\lambda^2 + c\lambda\right)} \left(\cosh\left(cP_H\lambda\right) + \left(1 - 2\epsilon_n\right) P_n \sinh\left(cP_H\lambda\right)\right) \tag{5.35}$$

As long as the ^{3}He polarization doesn't change appreciably between measurements of N_+ and N_-, these measurements can be recombined to yield the beam polarization [45]:

$$P_n = \frac{N_+ - N_-}{\sqrt{\left[\left(2\epsilon - 1\right) N_+ + N_-\right]^2 - 4N_0^2\epsilon_n^2}} \tag{5.36}$$

But what does it mean for the polarization to change appreciably? When these measurements are taken, a ^{3}He cell must be polarized and brought to the beamline in a holding field, just like in the ^{3}He only measurement, and then it gets sealed behind the lead shielding for a measurement.

The Spin Flipper can then be turned off and on to collect measurements of N_+ and N_-, with some duty cycle and pulse structure, to cancel out drifts associated with other aspects of the experiment. All the while, the ^{3}He polarization is decaying. Each pulse of the neutron source will pass through a ^{3}He cell with a slightly different polarization. If the change in the neutron counts that results from a change in the ^{3}He polarization (P_H becomes $P_H(1-d)$) is significantly less than the statistical fluctuations in the counts that would be naturally expected ($\sqrt{N}$), then the ^{3}He polarization change does not have an appreciable effect on the measurement and equation 5.36 is appropriate to use.

$$\frac{\sqrt{N}}{N} >> 1 - \frac{N'}{N} \tag{5.37}$$

$$\frac{\sqrt{N}}{N} >> 1 - \frac{\cosh cP_H\lambda\,(1-d) + P_n \sinh cP_H\lambda\,(1-d)}{\cosh cP_H\lambda + P_n \sinh cP_H\lambda} \tag{5.38}$$

This can be expanded when d is very small:

$$\frac{\sqrt{N}}{N} >> cP_H\lambda d \frac{P_N \cosh cP_H\lambda + \sinh cP_H\lambda}{P_N \sinh cP_H\lambda + \cosh cP_H\lambda} \tag{5.39}$$

This condition sets the acceptable amount of ^{3}He polarization loss, d. Because the ^{3}He decays exponentially, The fractional change in ^{3}He polarization over some time interval (Δt) is:

$$d = 1 - e^{-\frac{\Delta t}{T_1}} \tag{5.40}$$

Here, T_1 is the polarization of the ^{3}He cell. This shows that the duty cycle of the spin flipper can be tuned to keep the ^{3}He polarization from changing too much between measurements. The fastest it can flip is pulse-by-pulse (in an ideal world), but there is also some ring down associated with the circuit, which means that pulses during a flip will have to be dropped, as the Spin Flipper is neither off nor on. Changing the spin flipper more often lowers the number of events counted in a given time period- either lowering the measurement statistics or forcing a longer measurement. A less strict condition on the duty cycle timing is also the time interval associated with a change in polarization that is less than the uncertainty to which we can measure the ^{3}He polarization. This

depends on the measured lifetime of the cell on the beamline, which has yet to be measured to an appropriate uncertainty but is estimated to last approximately 40hrs. With a lifetime of 40hrs, the ^{3}He polarization decays by roughly .1% every 2.5 minutes, and 0.04% every 60 seconds.

Usually, in an experiment like this, a pattern of spin flipper states is chosen such that larger linear and quadratic drifts can be canceled out- essentially these patterns aim to ensure that the change of the spin flipper state doesn't systematically coincide with anything that drifts on a similar time scale. Here, the main source of drifts are likely to be a combination of shifts in the magnetic field, which are known to vary mostly with atmospheric changes in temperature, and fluctuations in the neutron source and its temperature. It is likely that the moderator temperature decreases when a pulse from the proton accelerator is dropped (which happens once every 600 reps), and then rises over the rest of the cycles, until the next pulse drops. This is not very well characterized and needs more study.

5.5 Measuring the Spin Flipper Efficiency

In the process of measuring the beam polarization with the Spin Flipper, it will be absolutely imperative to understand the efficiency of the spin flipper. Estimates of the Spin Flipper efficiency from spin tracking simulations are demonstrated in Section 3.4, and predict that the AFP Spin Flipper described in that chapter should flip spins to a high efficiency. It will also be important to measure this quantity, to verify that the operational parameters of the Spin Flipper (field strength, RF frequency, RF magnitude) are tuned to their optimal values. Because the polarization of the beam is expected to be very low, it will be difficult to see a difference between spin-up filtered states, and spin-down filtered states. As such, the beam will need to be artificially polarized by a polarized ^{3}He cell, on the upstream end of the beamline (See schematic in figure 5.7. For a ^{3}He polarizer cell with a polarization P_{H_P}, the resulting beam polarization is:

$$P_P(\lambda) = \frac{P_N \cosh\left(cP_{H_P}\lambda\right) - \sinh\left(cP_{H_P}\lambda\right)}{\cosh\left(cP_{H_P}\lambda\right) + P_N \sinh\left(cP_{H_P}\lambda\right)} \tag{5.41}$$

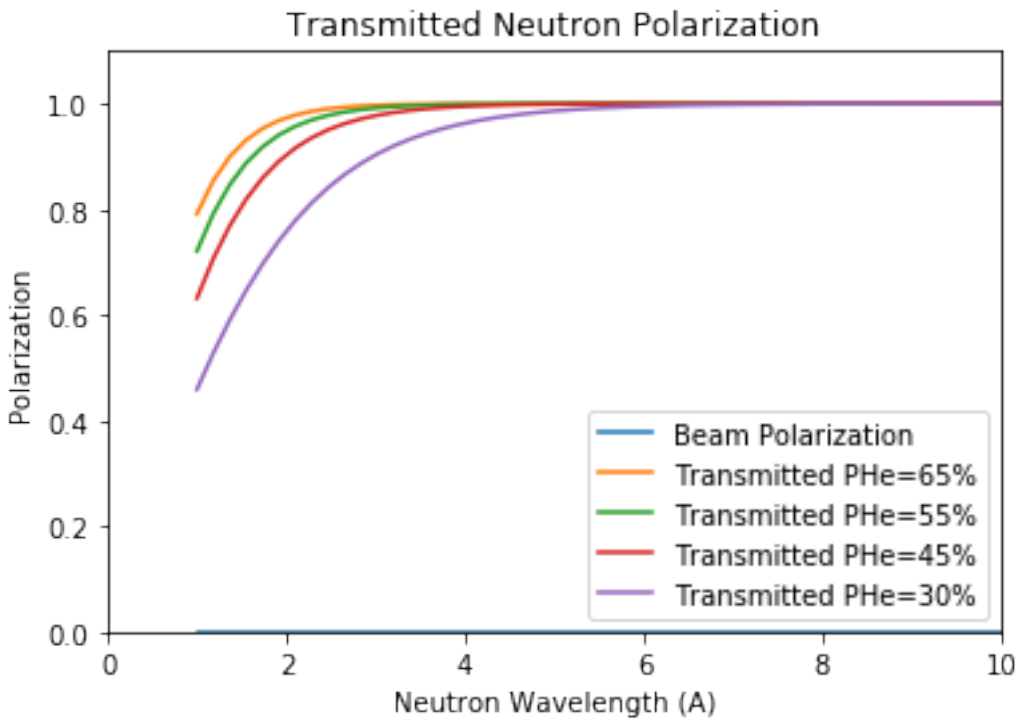

Figure 5.6: The polarization of the beam resulting from different values of ^{3}He polarization in the upstream polarizing cell

This ^{3}He cell's polarization will decay over the course of several measurements. The polarization of the beam transmitted by the cell remains high and fairly constant across wavelengths for several different values of ^{3}He polarization. Figure 5.6 shows a plot of the beam polarization calculated at several different values of ^{3}He polarization, for comparison. The fringing fields from the spectrometer magnet, the Static Coil, and the RF field are all superimposed in the small space available to put a polarizing cell, where they all produce nonuniform gradients. See Chapter 4 for more information on how the holding field designed for use with this cell aims to prolong the ^{3}He polarization lifetime.

This experiment will also employ an upstream normalizing monitor, the Spin Flipper, a polarized ^{3}He analyzing cell (with polarization P_{H_A}), and an analyzing monitor. Figure 5.7 contains a schematic diagram of the equipment used in this set of measurements.

This measurement will involve a comparison of all the different combinations of spin states that can be filtered through the Spin flipper and the analyzer. First, the ^{3}He cells will need to

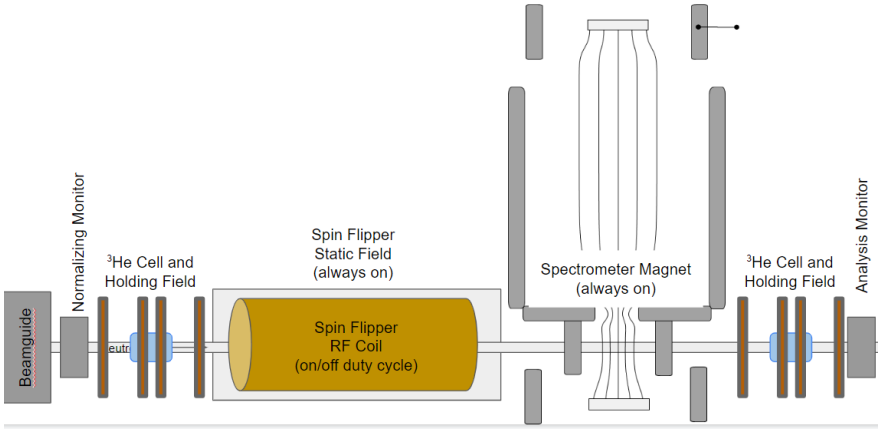

Figure 5.7: A schematic of the Spin Flipper Efficiency measurement. The neutron beam exits the guide and passes through a low-efficiency monitor, and a ^{3}He polarizing cell. Then it is carried adiabatically through the static fields of the experiment, just like in the polarization measurement with the spin flipper. Additionally, the polarization of the analyzer cell in front of the final monitor will also be flipped, so that all four possible combinations of helium and neutron interactions (Flipped and unflipped) can be analyzed.

be polarized, brought to the beamline, and installed. Then transmission measurements should be taken through the analyzing monitor, as the RF coil switches between being on or off, with the same duty cycle established for the polarimetry measurements in section 5.4. This provides 2 of the necessary measurements for comparison, N_{++} and N_{+}.Those measurements will need to be compared to measurements of the other spin state that can be filtered by the ^{3}He , N_{+-} and N_{--}. Using the transmission equations, and multiplying by the appropriate transformation that represents a flip, the expected spectra are expressed in equations 5.45 Here the first subscript indicates the status of the spin flipper, (off=+, and flipping=-), and the second represents the status of the ^{3}He spins (up=+, flipped=-), ϵ_n is the spin flipper efficiency, and ϵ_H is the efficiency of AFP

^{3}He flips.

$$N_{++} = \frac{a}{\lambda^g} e^{-\left(b/\lambda^2 + c\lambda\right)} \left[\cosh\left(cP_{H_A}\lambda\right) + P_P \sinh\left(cP_{H_A}\lambda\right)\right] \tag{5.42}$$

$$N_{-+} = \frac{a}{\lambda^g} e^{-\left(b/\lambda^2 + c\lambda\right)} \left[\cosh\left(cP_{H_A}\lambda\right) + \left(1 - 2\epsilon_n\right) P_P \sinh\left(cP_{H_A}\lambda\right)\right] \tag{5.43}$$

$$N_{+-} = \frac{a}{\lambda^g} e^{-\left(b/\lambda^2 + c\lambda\right)} \left[\cosh\left(cP_{H_A}\lambda\left(1 - 2\epsilon_H\right)\right) + P_P \sinh\left(cP_{H_A}\lambda\left(1 - 2\epsilon_H\right)\right)\right] \tag{5.44}$$

$$N_{+-} = \frac{a}{\lambda^g} e^{-\left(b/\lambda^2 + c\lambda\right)} \left[\cosh\left(cP_{H_A}\lambda\left(1 - 2\epsilon_H\right)\right) + \left(1 - 2\epsilon_n\right) P_P \sinh\left(cP_{H_A}\lambda\left(1 - 2\epsilon_H\right)\right)\right] \tag{5.45}$$

There are two ways to obtain this data. One is to flip the spins of the ^{3}He analyzer every other duty cycle of the spin flipper. The other is to take a measurement with the ^{3}He cell polarized, flipping the spin flipper until the ^{3}He polarization has decayed sufficiently. Then the cell gets removed from the shielding and re-polarized. The ^{3}He spins should be flipped with AFP, and then the flipped cell can be returned to the beamline to take the second set of measurements, flipping the spin flipper back and forth. The choice of which method will be used will depend on the ^{3}He polarization lifetime in the polarizer when the RF Coil is on, and whether or not a measurement of that length of time provides enough statistics.

To analyze this data, two Combined Transmission Ratios can be made, comparing the measurements with the spin flipper on, and those with the spin flipper off

$$CTR_{off} = \frac{N_{++} - N_{+-}}{N_{++} + N_{+-}} = \tanh\left(cP_{H_A}\lambda\epsilon_H\right) \left[\frac{\sinh\left(cP_{H_A}\lambda\left(1 - \epsilon\right)\right) + P_P \cosh\left(cP_{H_A}\lambda\left(1 - \epsilon\right)\right)}{cosh(cP_{H_A}\lambda\left(1 - \epsilon\right)) + P_P \sinh\left(cP_{H_A}\lambda\left(1 - 2\epsilon\right)\right)}\right] \tag{5.46}$$

$$CTR_{on} = \frac{N_{-+} - N_{--}}{N_{-+} + N_{--}} = \tanh\left(cP_{H_A}\lambda\epsilon_H\right) \left[\frac{\sinh\left(cP_{H_A}\lambda\left(1 - \epsilon\right)\right) + \left(1 - 2\epsilon_n\right) P_P \cosh\left(cP_{H_A}\lambda\left(1 - \epsilon\right)\right)}{cosh(cP_{H_A}\lambda\left(1 - \epsilon\right)) + \left(1 - 2\epsilon_n\right) P_P \sinh\left(cP_{H_A}\lambda\left(1 - \epsilon\right)\right)}\right] \tag{5.47}$$

These CTRs are similar to those of the Spin-Flipper-Free polarimetry measurement, described in Section 5.3. As ϵ_H approaches 1, The expressions in the brackets of the CTRs simply become the beam polarization (times the spin flipper efficiency if applicable). The ratio of the CTRs in this

limit is the efficiency factor associated with flipping the spins using the Spin Flipper:

$$\epsilon_n = \frac{1}{2}\left(1 - \frac{CTR_{on}}{CTR_{off}}\right) \tag{5.48}$$

But if the efficiency of the AFP ^{3}He flip is too low, the combined CTR will have to be examined more carefully.

$$\frac{CTR_{on}}{CTR_{off}} = \frac{\left[\frac{\sinh\left(cP_H\lambda(1-2\epsilon_H)\right)+(1-2\epsilon_n)P_P\cosh\left(cP_H\lambda(1-2\epsilon_H)\right)}{\cosh\left(cP_H\lambda(1-2\epsilon_H)\right)+(1-2\epsilon_n)P_P\sinh\left(cP_H\lambda(1-2\epsilon_H)\right)}\right]}{\left[\frac{\sinh\left(cP_H\lambda(1-2\epsilon_H)\right)+P_P\cosh\left(cP_H\lambda(1-2\epsilon_H)\right)}{\cosh\left(cP_H\lambda(1-2\epsilon_H)\right)+P_P\sinh\left(cP_H\lambda(1-2\epsilon_H)\right)}\right]} \tag{5.49}$$

CHAPTER 6

Summary, Conclusions and Future Work

6.1 Summary

This work describes the preparation for a polarimetry measurement on the Fundamental Physics Beamline (BL13) at the Spallation Neutron Source. The polarimetry measurement is intended to be an important check on systematic errors associated with the Nab experiment, as described in Chapter 2. The Nab experiment aims to precisely measure a, the electron-neutrino angle coupling constant which is related coupling constants that dictate the structure of the weak interaction, $\lambda = G_A/G_V$, the ratio of vector-to-axial-vector coupling constants in the standard model. The Nab experiment also aims to measure b, the Fierz interference term, which may indicate the need to expand the Standard Model to include some scalar and tensor interactions. When combined with measurements of the neutron lifetime, a measurement of λ can be used to calculate V_{ud}, one of the components of the CKM quark mixing matrix. This is an important test of the unitarity of the CKM matrix[27, 8, 11]. While it is anticipated that the neutron beam for the experiment is not likely to be polarized to a degree that will affect the results, it is important to verify that this is true. In order to stay within the systematic error budget for the Nab experiment, the beam polarization must be below 2×10^{-5}.

An important part of the preparations for a polarimetry measurement was the designing, simulating, and constructing of an Adiabatic Fast Passage Spin Flipper, which could also be used to mitigate any undesired residual polarization should the need arise. This Spin Flipper is described

in detail in Chapter3. This Spin flipper contains two parts- a static guiding field that transports the neutron spins adiabatically and an oscillating radio-frequency field. A simulation of the desired magneto-static potential was used to designate where the windings for the currents that generate a static field to orient the neutrons. This field was also required to blend in with the fringing fields from the Nab spectrometer. Then, a large simple solenoid was constructed to provide the oscillating field which causes the neutron spins to flip relative to the guide field when the field oscillations match the Larmor precision frequency of the neutrons.

The operation of the Spin Flipper was simulated using a Runge-Kutta integration of the torque on the neutron's magnetic moment, in a simulated version of the Nab experiment's field. These simulations indicate that the Spin Flipper should flip neutron spins with 99.98% efficiency under ideal conditions. The Spin Flipper efficiency has not been measured on the beamline, however, a method for doing so is indicated in Section 5.5. The efficiency of the Spin Flipper could hypothetically be measured on an auxiliary beamline with polarized neutrons, however, a facility with the extra beam time and space for the Spin Flipper and its compensation coils could not be found.

The polarimetry measurement for the Nab experiment also requires careful management of the ambient magnetic fields along the beamline, so that ^{3}He can be used as a neutron spin filter while performing the polarimetry measurements. When ^{3}He is polarized for use as a neutron polarizer, its polarization will decay in an ambient field- and it will decay faster if that ambient field has considerable gradients. Chapter 4 outlines how ^{3}He cells are constructed and polarized with Spin-Exchange Optical Pumping, and the physics associated with ^{3}He neutron spin filters. This chapter also describes some of the necessary conditions on the fields in order to maintain the ^{3}He polarization, and the equipment being used to generate these conditions.

The best candidate for achieving low enough magnetic field gradients while still fitting in the space allotted is a set of Merritt Coils, which are described in Section 4.3.2. In order to be useful, the field coil must produce a low static field gradient to maintain polarization during transportation between the SEOP polarization station and the beamline. Once these coils are on the beamline, they will need quickly tuned so that the gradients cancel those of the ambient field. External

coils which can apply an oscillating field and efficiently flip the ^{3}He spins on the beamline are also necessary for polarimetry measurements. These coils are easily attached to the Merritt coils, however, tuning them to achieve a high efficiency is a work in progress. Efficiencies as high as 97% have been achieved in a few measurements, however, it has been difficult to achieve this high efficiency consistently with the current equipment.

The polarimetry measurement itself requires several iterations of measurements with different configurations of ^{3}He polarization, and neutron beam polarization. Chapter 5 lays out a discussion of several ways a polarimetry measurement could be taken on BL13 with the Nab equipment, and some of the challenges associated with those measurements. The first method uses a ^{3}He spin filter in place on the upstream end of the beamline but does not require the use of the other fields in the experiment. This is convenient because the holding field for the ^{3}He cells only needs to be tuned once- It should be sufficiently strong to dominate over fluctuations in the ambient fields. This measurement also directly measures the polarization of the beam almost immediately after it exits the beam guide- it may prove useful to other experiments that later use this beamline. This measurement is not sensitive, however, to any fluctuations in polarization that may occur after the beam exits the beam guide. These would be caused by magnetic interactions with the field from the spectrometer, which is expected to transport neutron spins adiabatically (as shown in Section 3.4.3) but can not be well mapped in this region.

A second method for measuring the beam polarization outlined in Chapter 4 uses the Spin Flipper and polarized ^{3}He filters to measure the beam polarization. Because the Spin Flipper must be used in this measurement, the efficiency of the Spin Flipper must also be well-understood, and all of the fields from the spectrometer must be up and running. The analysis for this method works out very nicely if the polarization of the ^{3}He is stable between measurements, and has a long lifetime, however getting all the fields to work in concert for this measurement has been a difficult process. Some tuning still needs completing in order to get the ^{3}He system stable enough to make a measurement. There are also several tune-able parameters on the Spin Flipper, namely the slope of the gradient of the Static Coil, and the frequency and magnitude of the RF coil can be adjusted

to improve the Spin Flipper efficiency.

6.2 Future work

At the time of writing, the Nab experiment has only had a brief time available to use neutrons on the beamline, polarization measurements have not been taken with any discernible precision. Several steps are required before reliable polarimetry data can be taken. Among those steps is a careful calibration characterization of the neutron monitors and better optimization of the electronics that control their readout. At the time of this writing, this calibration is well on its way, however, the capacitance that spreads the pulses in one of the monitors' readout needs to be adjusted.

The Merritt coils and the AFP system that flips the ^{3}He spins on the beamline also need adjusting. A small amount of data has been taken to measure the lifetime of the ^{3}He polarization on the beamline, but a consistent method for transporting cells to the beamline and installing the coils that reliably preserves the ^{3}He polarization is proving to be quite the challenge. These lifetime measurements have been very inconsistent, and several unchecked sources of noise need to be investigated around the beamline to clean up these results.

Once reliable neutron data can be obtained, and the polarization of the ^{3}He , when installed on the beamline, is better understood, then the Spin Flipper can be tuned up to match the spectrometer fields, and its efficiency can be measured. The efficiency of the Spin Flipper can be adjusted by adjusting the static field strength, and the strength and frequency of the RF coil. Because the Spin Flipper's tuning can affect its efficiency, and the degree of ^{3}He polarization that reliably makes it to the beamline is poorly known, it is difficult to predict how close this measurement will come to verifying that the polarization is below the acceptable threshold of $P_n < 2 \times 10^{-5}$. This will depend strongly on how much time can be devoted to adjusting the tuning parameters.

If the polarization measured by our method is larger than the acceptable threshold, then the experiment can run in "Spin Flipper Mode," wherein the static field of the Spin Flipper will be on, and the RF coil will be cycled on and off with some duty cycle with respect to the beam pulses,

such that half the neutrons analyzed by the experiment are flipped with respect to their original polarization. This reduces the beam polarization by a factor of $1 - \epsilon_{SF}$, where ϵ_{SF} is the measured efficiency of the spin flipper.

This is mildly inconvenient because it will likely decrease the available statistics for the experiment- neutron pulses will need to be dropped when the RF coil rings down and the spin flipper changes states. There is also some concern that the neutron beam choppers may need to be used during the experiment in this case, to verify that the experiment is only using neutrons in the part of the spectrum where the Spin Flipper is most efficient. These choppers may interact magnetically with the neutron beam, and induce a component of polarization that wouldn't be measured on the whole beam. Extra polarimetry would need to be performed on a chopped beam to understand the presence of these effects, and whether or not they are successfully mitigated.

When the Nab experiment is complete, future plans for the Fundamental Physics Beamline include pNab[67, 68], which uses the Nab equipment and a polarized beam to measure the beta asymmetry, A and the neutrino asymmetry, B. This experiment will require that a more permanent polarizer be added to the beamline, but the Spin Flipper designed for the Nab experiment could also play an important part in evaluating systematic errors and helping this experiment to reach its goals as well.

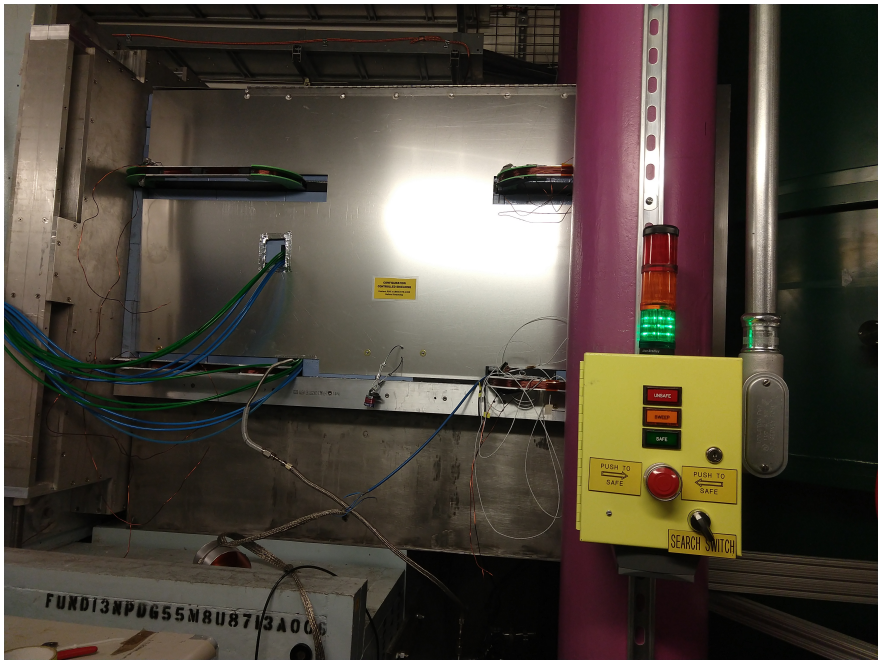

Figure 6.1: A photograph of the Spin Flipper and its compensation coils sealed up in the experiment's lead shielding

APPENDIX A

Monte Carlo Simulations of Neutron Beta Decay Events

As noted in Section 2.4, a Monte-Carlo event generator was used to simulate a distribution of beta decay events in order to more closely examine the phase space associated with neutron beta decay, and understand how our experiment places some limits on that phase space. This simulation is simpler than might be found under the hood in commercial software, like GEANT, but is meant for quick estimates, like how a beam polarization might affect the experiment's measurement of a, or how the proton momentum cutoff angle imposed by the spectrometer affects the distribution of events that Nab can count.

This simulation starts with a neutron decaying in its own rest frame. The neutron has a spin, which is either upward or downward along the z-axis, as defined by a probability associated with the intended beam polarization, which is set in the preamble of this simulation. The z-axis is chosen here because the neutron spins are expected to be polarized along the magnetic field of the Spectrometer, which points predominately in the vertical direction in the region where the neutrons that make it into the spectrometer are expected to decay.

Constraining the decay to the neutron rest frame and a single decay plane constrains the momenta of the daughter particles to sum to zero. To simplify the calculation, the momentum of the electron is chosen to lie on the x-axis. The energy of the electron, E_e, is chosen between 0 and the zero-point energy, E_0, from a random uniform distribution. The angle between the electron and neutrino ($\theta_{e\nu}$ is also chosen at random, such that the distribution of $\cos\theta_{e\nu}$ is uniform. The

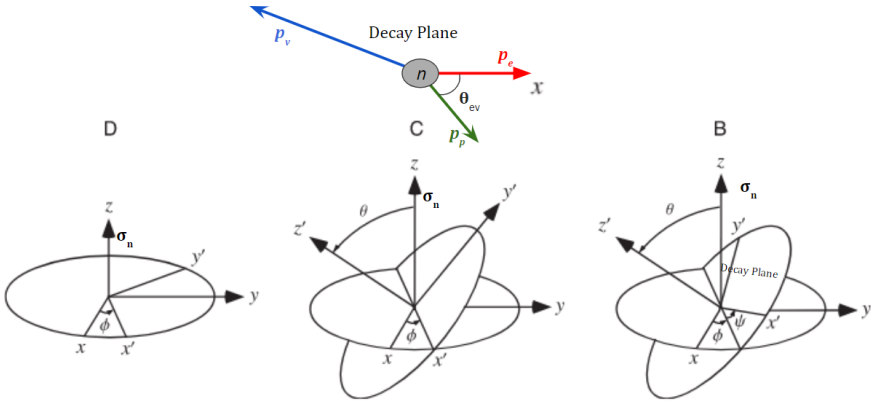

Figure A.1: A schematic illustration of the neutron decay plane, and how it gets rotated by Euler angles, ϕ, θ, and ψ into 3-dimensional space about the neutron spin, orient in the z-direction in the lab frame. Euler angle image is courtesy Wolfram Math World, [69]

4 momenta of each daughter particle are calculated using relativistic mechanics. The magnitude of the electron and neutrino momentum can be calculated. Once the momenta are established in the decay plane, three Euler angles[69] are chosen and used to rotate the decay plane randomly into 3-D space about the spin, which is oriented vertically in the lab frame. See figure A.1 for a schematic diagram of these rotations.

The probability of this event occurring is calculated using the differential decay rate equation, equation 2.2. The events are then sorted and counted based on a sampling rejection scheme[50]. In this scheme, the event probability is compared to a random number generated between (0,1), and if the random number is lower than the calculated event probability, the event is partially accepted. The event is fully accepted if the simulation verifies that the accepted event is visible to the spectrometer- That is to say that the angle between proton momentum the neutron spin (and thus the magnetic field) is inside the cutoff angle, as described in section 2.2.

When an event is inside the spectrometer's acceptance angle, it gets counted into a bin based on the electron energy, and the proton momentum squared. These counts can be plotted to produce the heat map of the teardrop-shaped phase space, or summed to produce the proton energy spectrum or the beta energy spectrum. Figure A.2 shows an example of the phase space teardrop plot, similar to the one in Chapter 2, however this one is a full heat map. Figure A.3 shows a slices of the

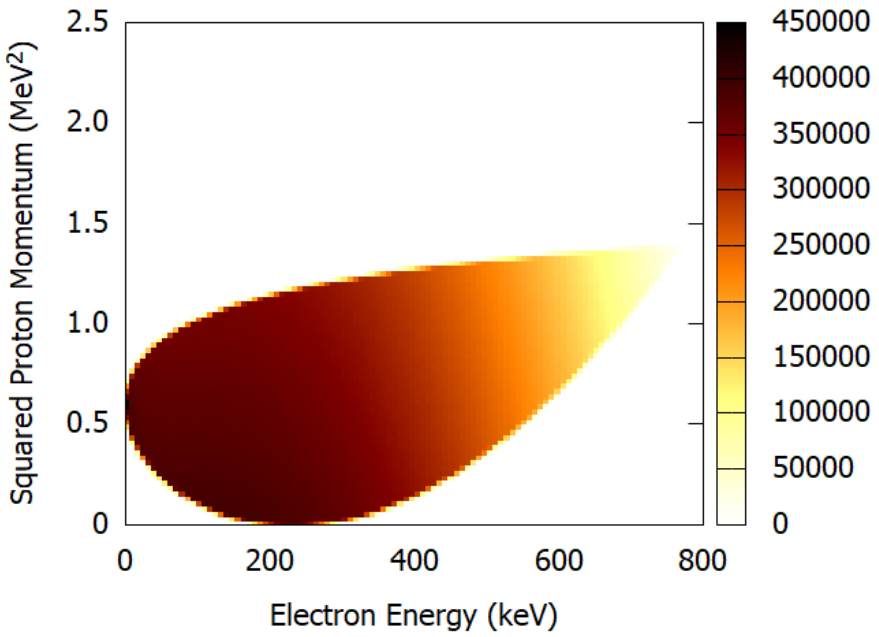

Figure A.2: The teardrop shaped phase space associated with the Nab experiment, the proton squared momentum, in MeV2, and the electron energy in keV. This is similar to figure 2.1, in Chapter 2

phase space; plot of the trapezoids whose slopes are related to the product $\beta_e a$, at various electron energies, Figure A.4 shows the energy spectrum of the full for 10^9 counted events. The plotted spectrum here is given for $b = 0$. This Monte Carlo could be used to examine the beta spectrum for other possible values of b.

In order to produce the estimates associated with the average angle the electron momentum makes with the neutron spin, an average was taken over the cosine of that angle, using the vector dot product. Several iterations of this simulation were run, with various values for the beam polarization in order to produce the figures at the end of Chapter 2.

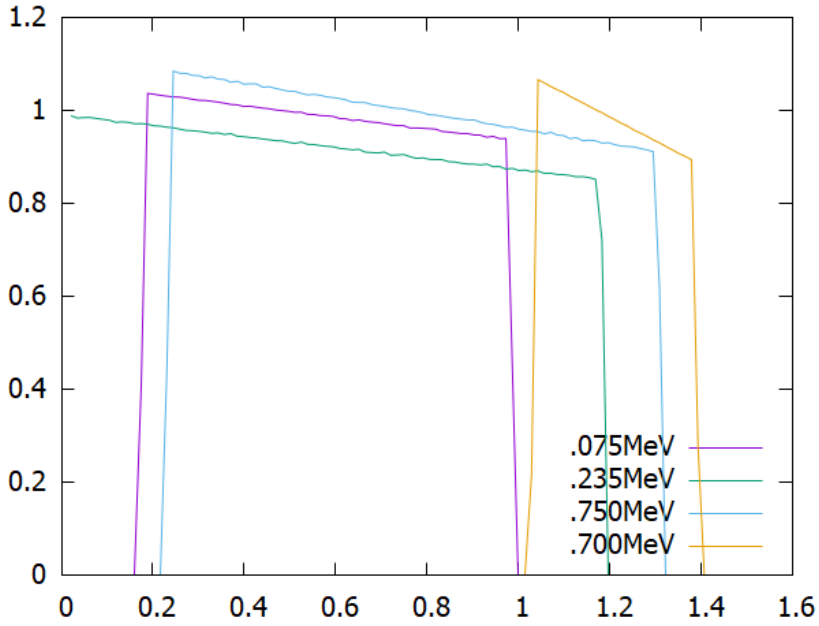

Figure A.3: A plot of the trapezoids whose slopes are related to the product $\beta_e a$, at various electron energies for 10^9 counted events. Here the vertical axis represents the yield in arbitrary units, and the horizontal axis is the energy in MeV.

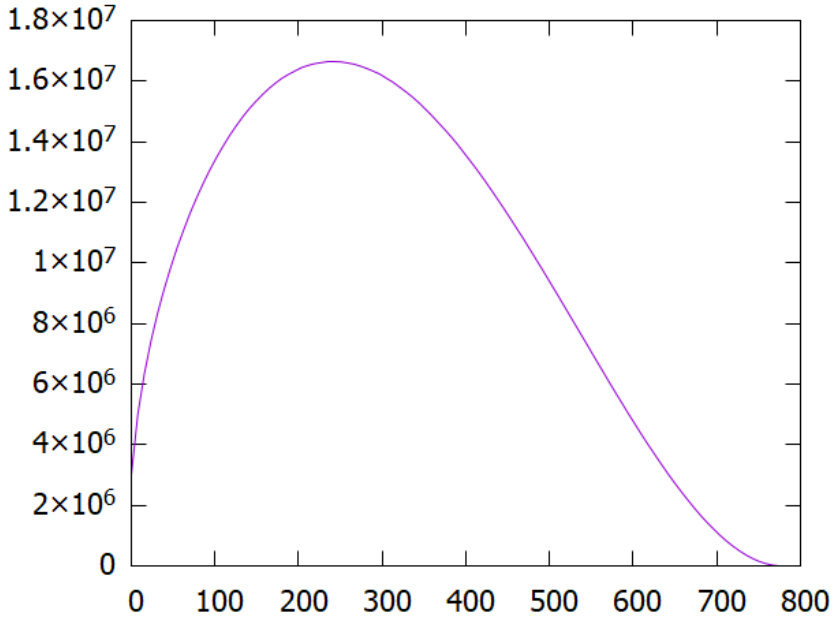

Figure A.4: A plot of the beta spectrum generated by the Monte Carlo, when b=0.

APPENDIX B

Drawings of the Spin Flipper Static Coil

Included here are the drawings for the Spin Flipper static coil. The coil as-built on the beamline at the SNS differs from these drawings only in that the box was shortened on the downstream end to be 0.825m long, in order to make more room for the ^{3}He holding fields on the beamline. Detailed drawings of the other pieces of the beamline assembly are available via the Nab wiki.

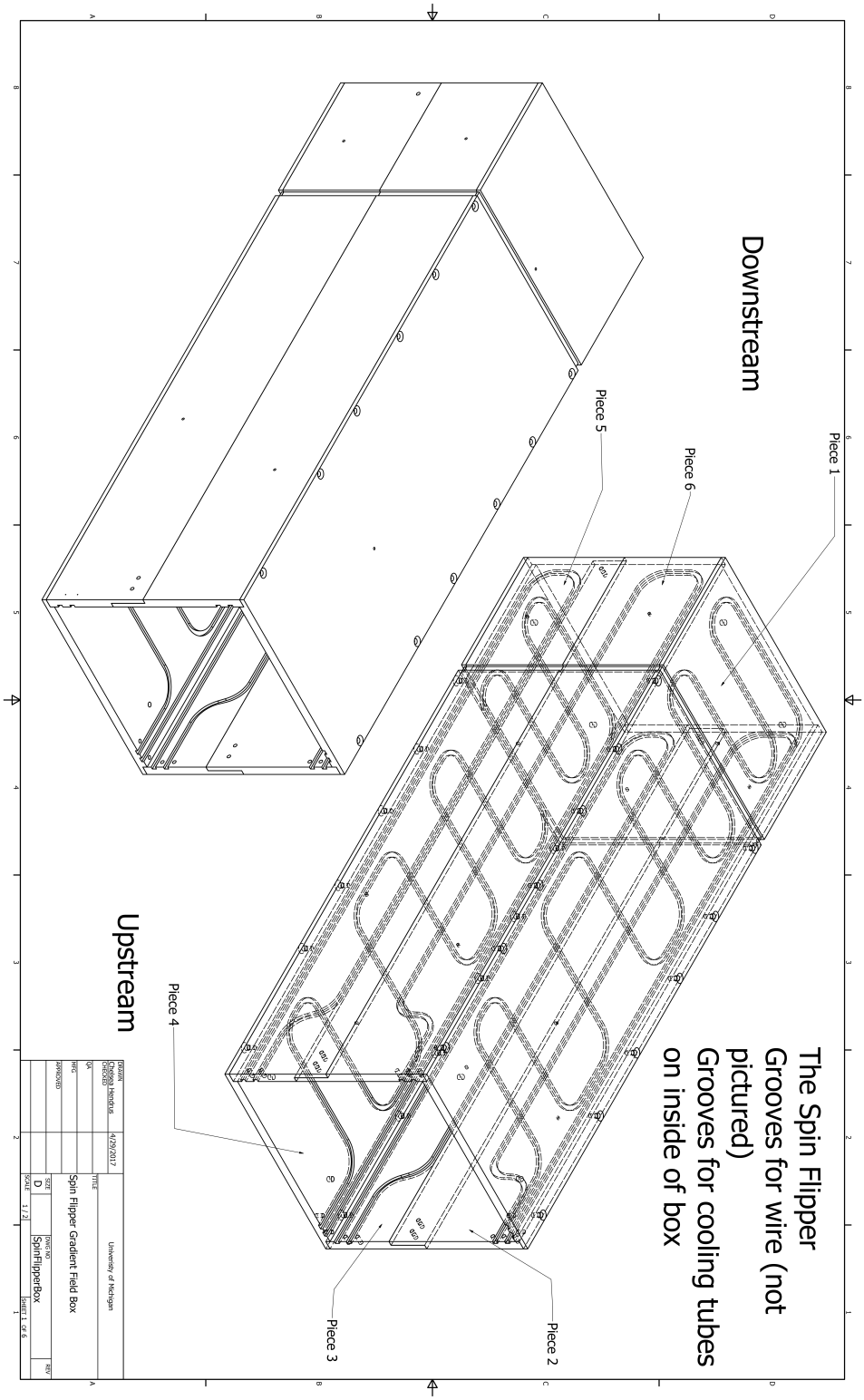

Figure B.1: Page 1 of the Spin Flipper Detailed Drawings

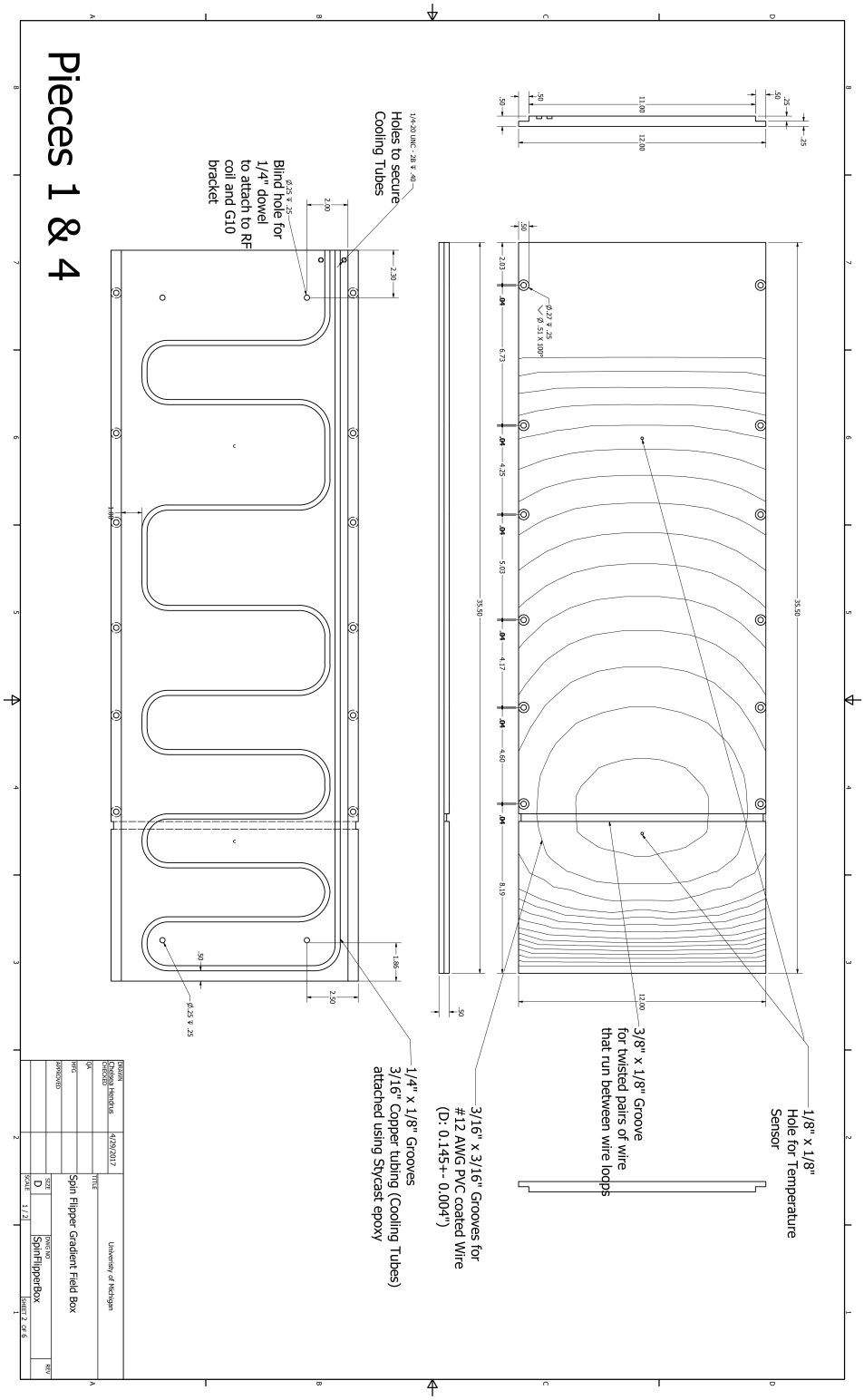

Figure B.2: Page 2 of the Spin Flipper Detailed Drawings

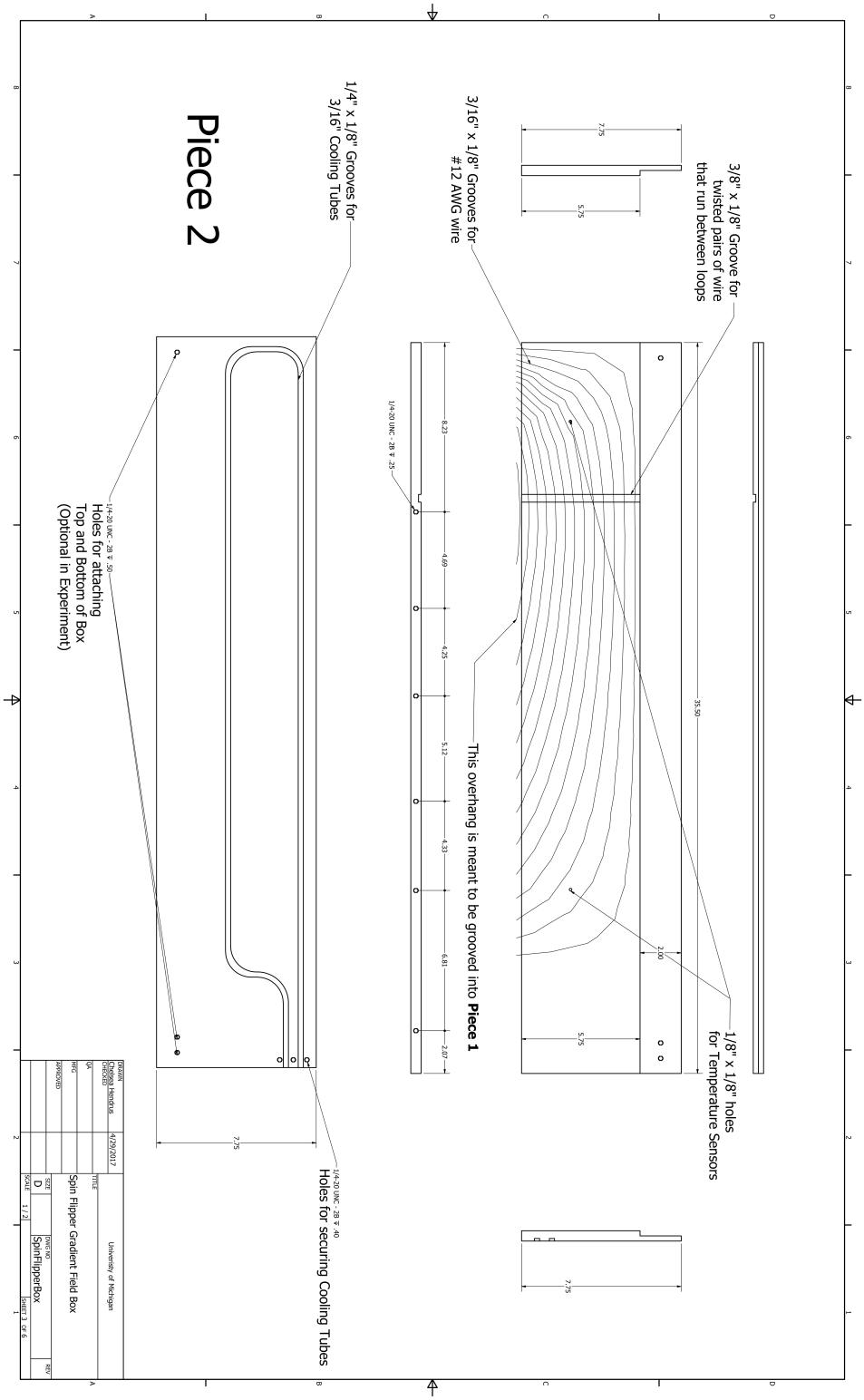

Figure B.3: Page 3 of the Spin Flipper Detailed Drawings

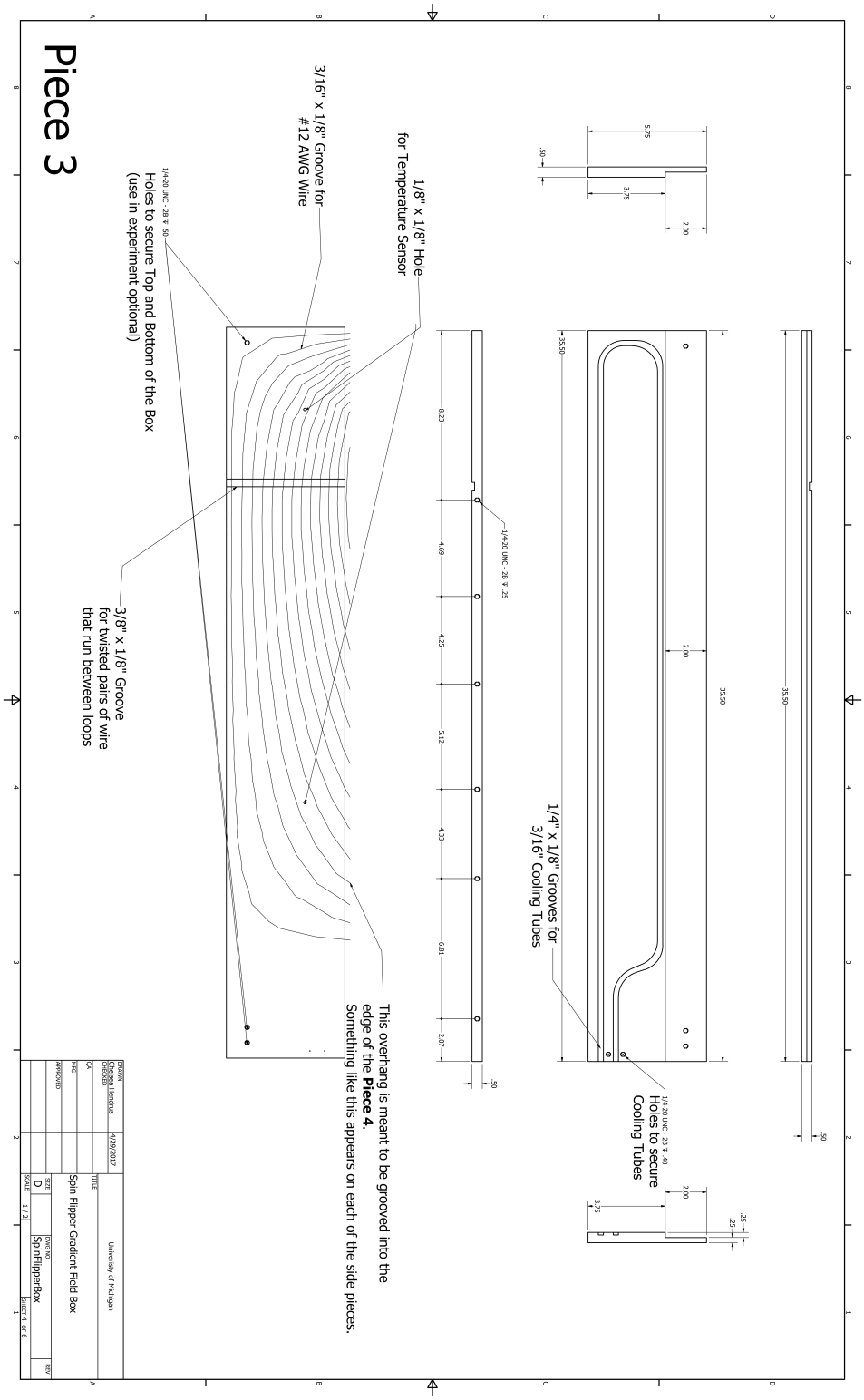

Figure B.4: Page 4 of the Spin Flipper Detailed Drawings

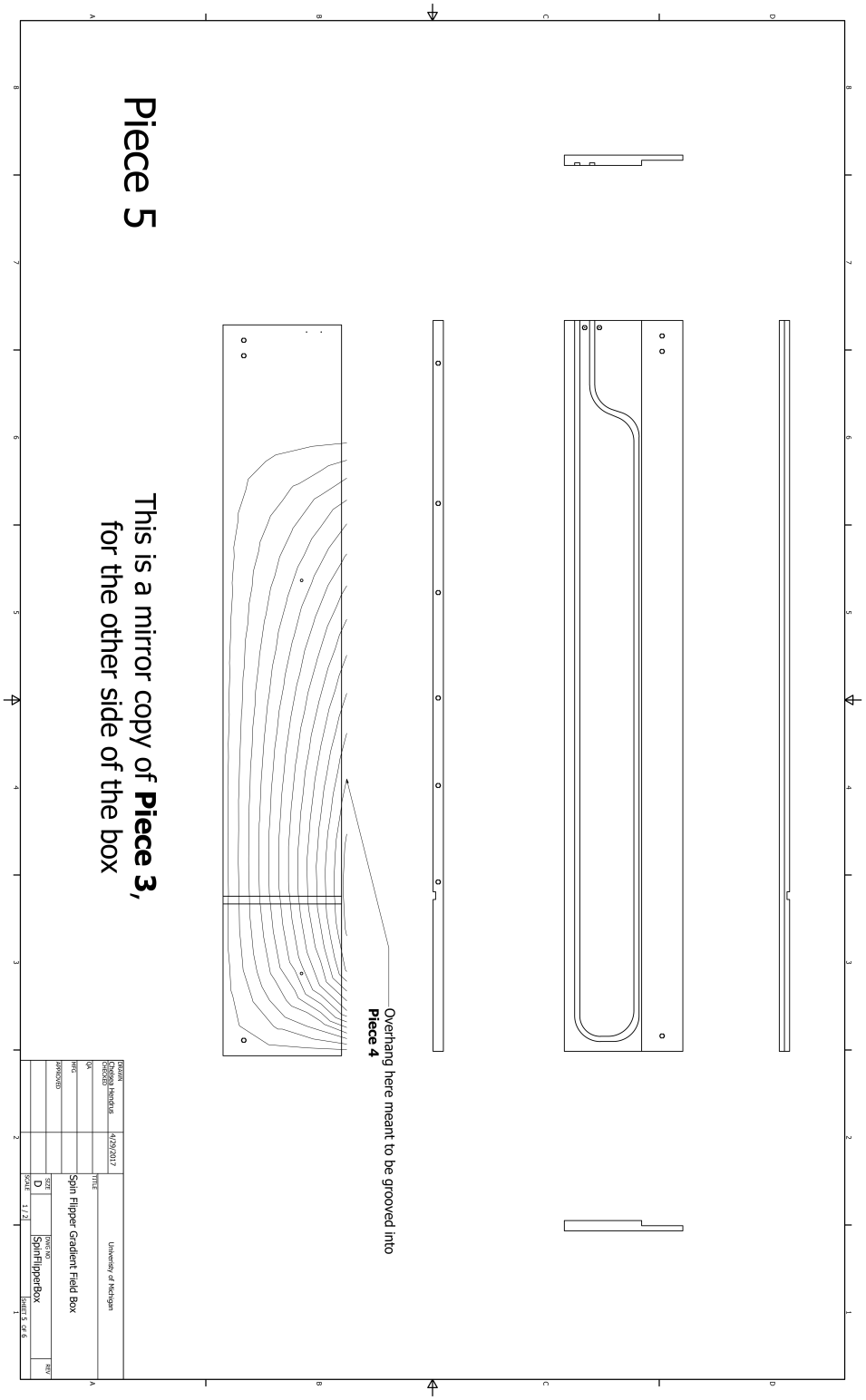

Figure B.5: Page 5 of the Spin Flipper Detailed Drawings

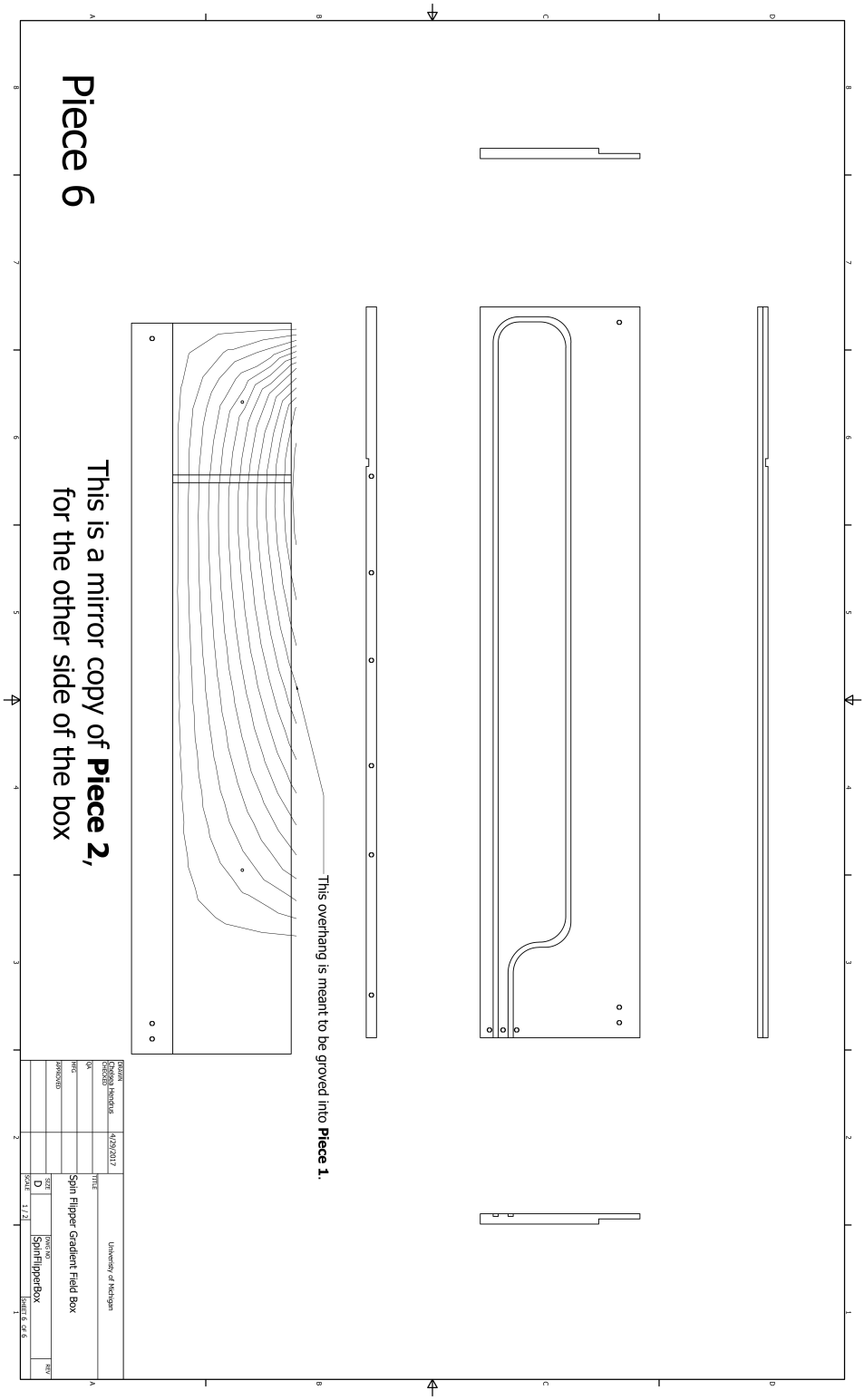

Figure B.6: Page 6 of the Spin Flipper Detailed Drawings

BIBLIOGRAPHY

[1] F. E. Wietfeldt and G. L. Greene. *Colloquium* : The neutron lifetime. 83(4):1173–1192.

[2] J. Chadwick. The neutron and its properties. 6(61):24–32.

[3] CERN. The standard model. https://home.web.cern.ch/science/physics/standard-model, 2023.

[4] A. D. Sakharov. Violation of cp invariance, c asymmetry, and baryon asymmetry of the universe. *Soviet Physics Uspekhi*, 34(5):392, may 1991.

[5] C. S. Wu, E. Ambler, R. W. Hayward, D. D. Hoppes, and R. P. Hudson. Experimental test of parity conservation in beta decay. *Phys. Rev.*, 105:1413–1415, Feb 1957.

[6] T. D. Lee and C. N. Yang. Question of parity conservation in weak interactions. *Phys. Rev.*, 104:254–258, Oct 1956.

[7] Class for Physics of the Royal Swedish Academy of Sciences. Scientific background on the nobel prize in physics 2008: Broken symmetries. October 2008.

[8] G. E. Konrad. *Measurement of the Proton Recoil Spectrum in Neutron Beta Decay with the Spectrometer aSPECT: Study of Systematic Effects*. PhD thesis, Mainz U., 2011.

[9] J. C. Hardy and I. S. Towner. Nuclear beta decays and ckm unitarity, 2018.

[10] M. Bargiotti, A. Bertin, M. Bruschi, M. Capponi, S. De Castro, R. Dona', P. Faccioli, D. Galli, B. Giacobbe, U. Marconi, I. Massa, M. Piccinini, M. Poli, N. Semprini-Cesari, R. Spighi, V. Vagnoni, S. Vecchi, M. Villa, A. Vitale, and A. Zoccoli. Present knowledge of the cabibbo-kobayashi-maskawa matrix. 2000.

[11] V. Cirigliano, A. Garcia, Doron Gazit, O. Naviliat-Cuncic, G. Savard, and A. Young. Precision Beta Decay as a Probe of New Physics. 7 2019.

[12] D F Geesaman and P E Reimer. The sea of quarks and antiquarks in the nucleon. *Reports on Progress in Physics*, 82(4):046301, mar 2019.

[13] R. Machleidt and D.R. Entem. Chiral effective field theory and nuclear forces. *Physics Reports*, 503(1):1–75, jun 2011.

[14] R. L. Cooper. *The Radiative Decay Mode of the Free Neutron*. PhD thesis, the University of Michigan, 2008.

[15] C. B. Hayes. Spin flipper, neutron polarimetry, and simulation, for the n3he experiment.

[16] J.D. Jackson, S.D. Treiman, and H.W. Wyld. Possible Test of Time Reversal Invariance in Beta Decay. *Physical Review*, 106(3):517–521, 1957.

[17] E. M. Scott. *Effects of the Nab Spectrometer on the Measurement of the Electron-Antineutrino Correlation Parameter a*. PhD thesis, The University of Tennessee, Knoxville, 2020.

[18] M. J. G. Borge, P. G. Hansen, B. Jonson, S. Mattsson, G. Nyman, A. Richter, and K. Riisager. The Axial Vector Strength in the Proton Rich Argon Isotopes. *Z. Phys. A*, 332:413–417, 1989.

[19] J. M. Berryman, S. Gardner, and M. Zakeri. Neutron stars with baryon number violation, probing dark sectors. *Symmetry*, 14(3), 2022.

[20] P.A. Zyla et al. Review of Particle Physics:neutron. *PTEP*, 2020(8):083C01, 2020. and 2021 update.

[21] A. Ceccucci, A. Ligeti, and Y. (KEK). Sakai. Reviews, Tables and Plots: Standard Model and Related Topics: 12. CKM Quark Mixing Matrix. *PTEP*, 2022:083C01, 2022.

[22] A. T. Yue, M. S. Dewey, D. M. Gilliam, G. L. Greene, A. B. Laptev, J. S. Nico, W. M. Snow, and F. E. Wietfeldt. Improved determination of the neutron lifetime. *Physical Review Letters*, 111(22), nov 2013.

[23] H. Saul, C. Roick, H. Abele, H. Mest, M. Klopf, A. Petukhov, T. Soldner, X. Wang, D. Werder, and B. Märkisch. Limit on the fierz interference term b from a measurement of the beta asymmetry in neutron decay. 125(11):112501.

[24] J. Fry, R. Alarcon, S. Baessler, S. Balascuta, L. Barron-Palos, T. Bailey, K. Bass, N. Birge, A. Blose, D. Borissenko, J. D. Bowman, L. J. Broussard, A. T. Bryant, J. Byrne, J. R. Calarco, J. Caylor, K. Chang, T. Chupp, T. V. Cianciolo, C. Crawford, X. Ding, M. Doyle, W. Fan, W. Farrar, N. Fomin, E. Frlez, M. T. Gericke, M. Gervais, F. Gluck, G. L. Greene, R. K. Grzywacz, V. Gudkov, J. Hamblen, C. Hayes, C. Hendrus, T. Ito, A. Jezghani, H. Li, M. Makela, N. Macsai, J. Mammei, R. Mammei, M. Martinez, D. G. Mathews, M. McCrea, P. McGaughey, C. D. McLaughlin, P. Mueller, D. van Petten, S. I. Penttila, D. E. Perryman, R. Picker, J. Pierce, D. Pocanic, Y. Qian, J. Ramsey, G. Randall, G. Riley, K. P. Rykaczewski, A. Salas-Bacci, S. Samiei, E. M. Scott, T. Shelton, S. K. Sjue, A. Smith, E. Smith, E. Stevens, J. Wexler, R. Whitehead, W. S. Wilburn, A. Young, and B. Zeck. The nab experiment: A precision measurement of unpolarized neutron beta decay. 219:04002.

[25] B. Märkisch, H. Mest, H. Saul, X. Wang, H. Abele, D. Dubbers, M. Klopf, A. Petoukhov, C. Roick, T. Soldner, and D. Werder. Measurement of the weak axial-vector coupling constant in the decay of free neutrons using a pulsed cold neutron beam. 122(24):242501.

[26] B. Plaster, E. Adamek, B. Allgeier, J. Anaya, H.O. Back, Y. Bagdasarova, D.B. Berguno, M. Blatnik, J.G. Boissevain, T.J. Bowles, L.J. Broussard, M.A.-P. Brown, R. Carr, D.J. Clark, S. Clayton, C. Cude-Woods, S. Currie, E.B. Dees, X. Ding, S. Du, B.W. Filippone, A. García, P. Geltenbort, S. Hasan, A. Hawari, K.P. Hickerson, R. Hill, M. Hino, J. Hoagland, S.A.

Hoedl, G.E. Hogan, B. Hona, R. Hong, A.T. Holley, T.M. Ito, T. Kawai, K. Kirch, S. Kitagaki, A. Knecht, S.K. Lamoreaux, C.-Y. Liu, J. Liu, M. Makela, R.R. Mammei, J.W. Martin, N. Meier, D. Melconian, M.P. Mendenhall, S.D. Moore, C.L. Morris, R. Mortensen, S. Nepal, N. Nouri, R.W. Pattie, A. Pérez Galván, D.G. Phillips II, A. Pichlmaier, R. Picker, M.L. Pitt, J.C. Ramsey, R. Rios, R. Russell, K. Sabourov, A.L. Sallaska, D.J. Salvat, A. Saunders, R. Schmid, S.J. Seestrom, C. Servicky, E.I. Sharapov, S.K.L. Sjue, S. Slutsky, D. Smith, W.E. Sondheim, X. Sun, C. Swank, G. Swift, E. Tatar, W. Teasdale, C. Terai, B. Tipton, M. Utsuro, R.B. Vogelaar, B. VornDick, Z. Wang, B. Wehring, J. Wexler, T. Womack, C. Wrede, Y.P. Xu, H. Yan, A.R. Young, J. Yuan, and B.A. Zeck. Final results for the neutron b/b-asymmetry parameter ia/isubb0/b/sub from the UCNA experiment. *EPJ Web of Conferences*, 219:04004, 2019.

[27] N. W. Birge. *Measurement of the Fierz Interference Term for Calcium-45*. PhD thesis, The University of Tennessee, Knoxville, 2019.

[28] M. T. Burkey, G. Savard, A. Gallant, N. D. Scielzo, J. A. Clark, T. Y. Hirsh, D. P. Burdette, E. Heckmaier, J. Klimes, K. Kolos, S. T. Marley, G. E. Morgan, R. Orford, S. Padgett, J. Pierce, R. Segel, K. S. Sharma, L. Varriano, and B. S. Wang. Precision β - ν correlation measurements with the Beta-decay Paul Trap. *Hyperfine Interactions*, 240(1):1–12, April 2019.

[29] V. Araujo-Escalona, D. Atanasov, X. Flé chard, P. Alfaurt, P. Ascher, B. Blank, L. Daudin, M. Gerbaux, J. Giovinazzo, S. Grévy, T. Kurtukian-Nieto, E. Liénard, G. Quéméner, N. Severijns, S. Vanlangendonck, M. Versteegen, and D. Zákoucký. Simultaneous measurements of the beta -neutrino angular correlation in pure fermi and pure gamow-teller transitions using beta-proton coincidences. *Physical Review C*, 101(5), may 2020.

[30] M. Beck, F. Ayala Guardia, M. Borg, J. Kahlenberg, R. Muñoz Horta, C. Schmidt, A. Wunderle, W. Heil, R. Maisonobe, M. Simson, T. Soldner, R. Virot, O. Zimmer, M. Klopf, G. Konrad, S. Baeßler, F. Glück, and U. Schmidt. Improved determination of the β–$\overline{\nu}_e$ angular correlation coefficient a in free neutron decay with the aSPECT spectrometer. *Phys. Rev. C*, 101:055506, May 2020.

[31] M. T. Hassan, W. A. Byron, G. Darius, C. DeAngelis, F. E. Wietfeldt, B. Collett, G. L. Jones, A. Komives, G. Noid, E. J. Stephenson, F. Bateman, M. S. Dewey, T. R. Gentile, M. P. Mendenhall, and J. S. Nico. Measurement of the neutron decay electron-antineutrino angular correlation by the aCORN experiment. 103(4):045502.

[32] S. Baeßler, J. D. Bowman, S. I. Penttilä, and D. Počanić. New precision measurements of free neutron beta decay with cold neutrons. *Journal of Physics. G, Nuclear and Particle Physics*, 41(11), 10 2014.

[33] D. Moser, H. Abele, J. Bosina, H. Fillunger, T. Soldner, X. Wang, J. Zmeskal, and G. Konrad. NoMoS: Anir/i b×/b ib/idrift momentum spectrometer for beta decay studies. *EPJ Web of Conferences*, 219:04003, 2019.

[34] X. Wang, C. Ziener, H. Abele, S. Bodmaier, D. Dubbers, J. Erhart, A. Hollering, E. Jericha, J. Klenke, H. Fillunger, W. Heil, C. Klauser, G. Konrad, M Lamparth, T. Lauer, M. Klopf,

R. Maix, B. Märkisch, W. Mach, H. Mest, D. Moser, A. Pethoukov, L. Raffelt, N. Rebrova, C. Roick, H. Saul, U. Schmidt, T. Soldner, R. Virot, and O. Zimmer and. Design of the magnet system of the neutron decay facility PERC. *EPJ Web of Conferences*, 219:04007, 2019.

[35] T. E. Mason, T. A. Gabriel, R. K. Crawford, K. W. Herwig, F. Klose, and J. F. Ankner. The spallation neutron source: A powerful tool for materials research.

[36] N. Fomin, G.L. Greene, R.R. Allen, V. Cianciolo, C. Crawford, T.M. Tito, P.R. Huffman, E.B. Iverson, R. Mahurin, and W.M. Snow. Fundamental neutron physics beamline at the spallation neutron source at ORNL. 773:45–51.

[37] R. Mitchell. *The Nab Cryogen Free Magnet System Job Number 3658*.

[38] L. J. Broussard, B. A. Zeck, E. R. Adamek, S. Baeßler, N. Birge, M. Blatnik, J. D. Bowman, A. E. Brandt, M. Brown, J. Burkhart, N. B. Callahan, S. M. Clayton, C. Crawford, C. Cude-Woods, S. Currie, E. B. Dees, X. Ding, N. Fomin, E. Frlez, J. Fry, F. E. Gray, S. Hasan, K. P. Hickerson, J. Hoagland, A. T. Holley, T. M. Ito, A. Klein, H. Li, C.-Y. Liu, M. F. Makela, P. L. McGaughey, J. Mirabal-Martinez, C. L. Morris, J. D. Ortiz, R. W. Pattie Jr., S. I. Penttilä, B. Plaster, D. Počanić, J. C. Ramsey, A. Salas-Bacci, D. J. Salvat, A. Saunders, S. J. Seestrom, S. K. L. Sjue, A. P. Sprow, Z. Tang, R. B. Vogelaar, B. Vorndick, Z. Wang, W. Wei, J. Wexler, W. S. Wilburn, T. L. Womack, and A. R. Young. Detection system for neutron β decay correlations in the UCNB and nab experiments. 849:83–93.

[39] H. Li. *The Main Electrode System of the Nab Experiment and the Analysis of the Performance in the Measurement of the Fierz Term b*. PhD thesis, The University of Virginia, 2021.

[40] H. P. Mumm, A. Garcia, L. Grout, M. Howe, L. P. Parazzoli, R. G. H. Robertson, K. M. Sundqvist, J. F. Wilkerson, S. J. Freedman, B. K. Fujikawa, L. J. Lising, M. S. Dewey, J. S. Nico, A. K. Thompson, T. E. Chupp, R. L. Cooper, K. P. Coulter, S. R. Hwang, R. C. Welsh, L. J. Broussard, C. A. Trull, F. E. Wietfeldt, and G. L. Jones. emiT: An apparatus to test time reversal invariance in polarized neutron decay. *Review of Scientific Instruments*, 75(12):5343–5355, dec 2004.

[41] T. E. Chupp, R. L. Cooper, K. P. Coulter, S. J. Freedman, B. K. Fujikawa, A. Garcí a, G. L. Jones, H. P. Mumm, J. S. Nico, A. K. Thompson, C. A. Trull, F. E. Wietfeldt, and J. F. Wilkerson. Search for a t-odd and p-even triple correlation in neutron decay. *Physical Review C*, 86(3), sep 2012.

[42] J.R. Taylor. *Classical Mechanics*. G - Reference,Information and Interdisciplinary Subjects Series. University Science Books, 2005.

[43] A. Abragam. *The Principles of Nuclear Magnetism*. The international series of monographs on physics. Clarendon Press, 1970.

[44] J.J. Sakurai. *Advanced Quantum Mechanics*. Always learning. Pearson Education, Incorporated, 2006.

[45] M.M. Musgrave, S. Baeßler, S. Balascuta, L. Barrón-Palos, D. Blyth, J.D. Bowman, T.E. Chupp, V. Cianciolo, C. Crawford, K. Craycraft, N. Fomin, J. Fry, M. Gericke, R.C. Gillis, K. Grammer, G.L. Greene, J. Hamblen, C. Hayes, P. Huffman, C. Jiang, S. Kucuker, M. McCrea, P.E. Mueller, S.I. Penttilä, W.M. Snow, E. Tang, Z. Tang, X. Tong, and W.S. Wilburn. Measurement of the absolute neutron beam polarization from a supermirror polarizer and the absolute efficiency of a neutron spin rotator for the NPDGamma experiment using a polarized 3he neutron spin-filter. 895:19–28.

[46] M Sharma. *Precision Neutron Polarimetry and a Measurement of Parity Violating Assymetry in N-P Capture*. PhD thesis, The University of Michigan, 2008.

[47] D.J. Griffiths. *Introduction to Quantum Mechanics*. Pearson international edition. Pearson Prentice Hall, 2005.

[48] V.I. Luschikov and Yu.V. Taran. On the calculation of the neutron adiabatic spin-flipper. 228(1):159–160.

[49] Krohn-Hite Corporation. *Model 7500 DC 10 1MHz Wideband Power Amplifier Operating Manual*.

[50] W. H. Press, S. A. Teukolsky, W. T. Vetterling, and B. P. Flannery. *Numerical Recipes in C*. Cambridge University Press, Cambridge, USA, second edition, 1992.

[51] L. Lyu. Numerical simulation of space plasmas (i) lecture notes [ap-4036].

[52] J. R. Cash and A. H. Karp. A variable order runge-kutta method for initial value problems with rapidly varying right-hand sides. 16(3):201–222.

[53] F. Mackay, R. J. Marchand, and K. Kabin. Divergence-free magnetic field interpolation and charged particle trajectory integration. *Journal of Geophysical Research*, 111, 2006.

[54] M. Yang, D. del Castillo-Negrete, G. Zhang, and M. Beidler. A divergence-free constrained magnetic field interpolation method for scattered data. 2022.

[55] M Batz, S Baeßler, W Heil, W Otten, D Rudersdorf, Y Sobolev, and M Wolf. 3he spin filter for neutrons. 110(3):6.

[56] C.Y. Jiang, X. Tong, D.R. Brown, W.T. Lee, H. Ambaye, J.W. Craig, L. Crow, H. Culbertson, R. Goyette, M.K. Graves-Brook, M.E. Hagen, B. Kadron, V. Lauter, L.W. McCollum, J.L. Robertson, B. Winn, and A.E. Vandegrift. Polarized 3he neutron spin filters at oak ridge national laboratory. *Physics Procedia*, 42:191–199, 2013. 9th International Conference on Polarised Neutrons in Condensed Matter Investigations.

[57] S Boag, C Y Jiang, X Tong, and S R Parnell. Lifetime behaviour and polarization stability in 3he neutron spin filter cells. *Journal of Physics: Conference Series*, 528(1):012019, jul 2014.

[58] M.M. Musgrave. *Neutron Polarimetry with Polarized 3He for the NPDGamma Experiment*. PhD thesis, The University of Tennessee, Knoxville, 2014.

[59] W C Chen, T R Gentile, C B Fu, S Watson, G L Jones, J W McIver, and D R Rich. Polarized ^{3} he cell development and application at NIST. 294:012003.

[60] Thad G. Walker and William Happer. Spin-exchange optical pumping of noble-gas nuclei. *Rev. Mod. Phys.*, 69:629–642, Apr 1997.

[61] T. E. Chupp, M. E. Wagshul, K. P. Coulter, A. B. McDonald, and W. Happer. Polarized, high-density, gaseous ^{3}He targets. *Phys. Rev. C*, 36:2244–2251, Dec 1987.

[62] M. V. Romalis and G. D. Cates. Accurate 3 he polarimetry using the rb zeeman frequency shift due to the rb 3 he spin-exchange collisions. 58(4):3004–3011.

[63] E. Babcock, Z. Salhi, L. Barnsley, J. Voigt, S. Mattauch, and A. Ioffe. μ-metal magnetic cavities for polarization and maintenance of polarization of 3he gas. *Journal of Physics: Conference Series*, 1316(1):012019, oct 2019.

[64] N. Nouri and B. Plaster. Comparison of magnetic field uniformities for discretized and finite-sized standard $\cos\theta$, solenoidal, and spherical coils. *Nucl. Instrum. Meth. A*, 723:30, 2013.

[65] R. Merritt, C. Purcell, and G. Stroink. Uniform magnetic field produced by three, four, and five square coils. 54(7):879–882.

[66] B. C. Schafer, W. A. Byron, W. C. Chen, B. Collett, M. S. Dewey, T. R. Gentile, Md T. Hassan, G. L. Jones, A. Komives, and F. E. Wietfeldt. Neutron polarimetry using a polarized 3he cell for the aCORN experiment. 988:164862.

[67] N. Fomin, J. Fry, R. W. Pattie, and G. L. Greene. Fundamental neutron physics at spallation sources. *Annual Review of Nuclear and Particle Science*, 72(1):151–176, 2022.

[68] Nab/pNab Collaborations. Letter of intent for an experiment at the fnpb/sns pnab: a program of study of polarized neutron beta decay. Draft, December, 2020.

[69] E. W. Weisstein. ”euler angles.” from mathworld–a wolfram web resource. https://mathworld.wolfram.com/eulerangles.html.